

Applications of high-gain parametric down-conversion to metrology

by

Samuel Lemieux

A thesis
submitted to the University of Ottawa
in partial fulfillment of the
thesis requirement for the degree of
Doctor of Philosophy
in
Physics

Ottawa, Ontario, Canada, 2023

© Samuel Lemieux, Ottawa, Canada, 2023

Abstract

Parametric down-conversion (PDC) is a nonlinear optical process widely used to generate pairs of photons. It occurs when an intense laser traverses an optical parametric amplifier (OPA). When the gain of the amplifier is increased, the number of downconverted photons increases exponentially: this is the high-gain regime of PDC. High-gain PDC is potentially a versatile tool for metrology. It is a source of highly-entangled states and bright squeezed states for applications in quantum information and interferometry. In addition, the high number of photons in high-gain PDC makes it possible to use diodes and cameras directly, instead of single-photon detectors and coincidence-counting apparatus. However, all the quantum-optical experimental methods need to be generalized or adapted for a high-photon flux. Most of the theoretical and experimental techniques used or developed in this thesis aim to address this transition from low to high-photon flux of PDC.

I theoretically and experimentally provide strategies to harness the mode structure of PDC, bringing us steps closer to a usable source of bright squeezed vacuum for interferometry and quantum imaging. I present experimental progress in reducing the number of frequency modes of high-gain PDC, which is naturally broadband, and consequently highly multimode. Our theory for high-gain PDC generated in a nonlinear crystal provides a set of modes containing physically meaningful information, i.e. the pairwise quantum correlations between independent modes. In addition, I provide a thorough discussion on the limit of $SU(1,1)$ interferometry in regards to internal loss and gain unbalancing. Finally, I tie the frequency spectrum of high-gain PDC to the properties of vacuum fluctuations, allowing to predict the number of photons from first principles, making it a powerful tool for spectroradiometry. Those developments are a springboard towards usable high-gain PDC for metrology.

Acknowledgements

This thesis was made possible thanks to many individuals and institutions. I acknowledge the financial support from the Fonds de recherche du Québec - Nature et technologies and the Canada Excellence Research Chairs program. I'm proud to say I am one of the first student to benefit from the Max Planck- University of Ottawa Center for Extreme and Quantum Photonics. This collaboration allowed me work at the Max-Planck institute for the Science of Light, in Erlangen, Germany, in the laboratory of Maria Chekhova, from whom I've learnt so much. From this collaboration, I want to give another special thanks to Gerd Leuchs and Timur Iskhakov.

I'm grateful to Robert W. Boyd, who has provided me with an outstanding learning environment, growing opportunities, and his invaluable experience throughout all my graduate studies. I acknowledge Robert Fickler and Enno Giese, who were instrumental in the work presented here, and in my progress as a scientist. Finally, I thank Jeremy Upham, whose support and friendship made this thesis possible.

Dedication

To my children.

Table of Contents

1	Introduction	1
1.1	Squeezed vacuum	5
1.1.1	Quantum-mechanical description of squeezed vacuum	6
1.1.2	Correlations in the second order	10
1.1.3	Parametric down-conversion	12
1.1.4	Multimode radiation and mode decomposition	14
1.2	Phase sensitivity	15
1.3	High-gain parametric down-conversion	17
1.3.1	Quantization of the electromagnetic field in a medium	18
1.3.2	Solving the equation of motion	21
2	Engineering the Frequency Spectrum of Bright Squeezed Vacuum via Group Velocity Dispersion in an SU(1,1) Interferometer	26
3	Bright squeezed vacuum in a nonlinear interferometer: Frequency and temporal Schmidt-mode description	36
4	Properties of bright squeezed vacuum at increasing brightness	46
5	Phase sensitivity of gain-unbalanced nonlinear interferometers	56
6	A primary radiation standard based on quantum nonlinear optics	67

7 Conclusion	79
References	81

Chapter 1

Introduction

Lasers are a tremendous technology that has changed communications, fabrication, medicine and many other fields besides. A key element of the laser is that as a photon travels through a medium primed for this purpose, it can stimulate the creation of another photon from the medium that is exactly in phase with the first photon. This amplification leads to intense coherent beams and in addition to the above technological advantages, has profoundly deepened our understanding of light-matter interactions, including the research domain of nonlinear optics [1].

Nonlinear optics has since shown that, under the right conditions, another kind of optical process can occur: a photon traveling through a nonlinear medium has a statistical possibility to spontaneously be annihilated and to have a pair of photons be created in its place. Because this process obeys conservation of energy and momentum, observing the properties of one of these photons gives us clear information about the other [2]. Consequently, particular properties about the behaviour of these photons arise. One such nonlinear optical process is photon-pair generation by spontaneous parametric down conversion (PDC) and is fundamentally different from just low-intensity light from any other source.

In the last decades, photon-pair generation via PDC has been ubiquitous in quantum optics laboratories and is at the heart of many groundbreaking experiments in quantum physics [3–5]. It is a cheap and reliable source of: entangled particles because the conservation laws dictating their creation cause correlations in the different degrees of freedom of the photons (e.g. polarization, position-momentum), allowing quantum entanglement;

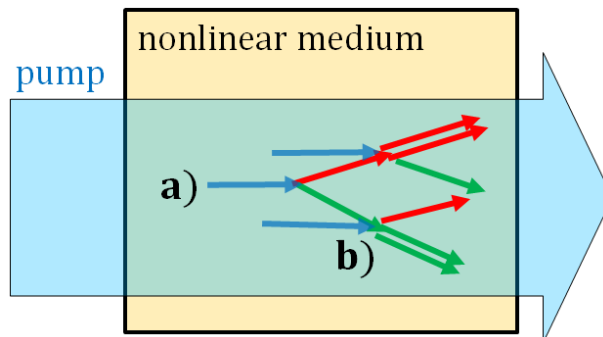


Figure 1.1: Cartoon representation of the PDC process occurring when an intense laser beam (pump) traverses a nonlinear medium. a) Spontaneous regime of PDC: when the right conditions are met, there is a low probability that one photon of the pump (blue in the figure) gets converted into photons of lower frequency (red and green in the figure). The color, spectral width, direction, and angular spread are determined by the properties of the medium and the pump laser. b) High-gain regime of PDC: when the nonlinear coupling is strong enough, spontaneous emission acts as a trigger for new down-conversion processes, leading to an exponential increase in the number of photons with respect to the gain.

squeezed states of light because their ensuing statistics can reduce the uncertainty or noise inherent in a particular observable parameter; or heralded single photons, because in being created together one photon reliably indicates the presence of the other.

This thesis builds upon the research of PDC by exploring the following question: what happens when the laser intensity is increased, such that the PDC process ceases to be spontaneous and the twin-photons turn into twin-beams, as depicted in Fig. (1.1)? It had been demonstrated that twin-beams, containing up to millions of photons per mode, retain many advantages of photon pairs, such as photon-number correlation, and even polarization entanglement [6, 7]. Those experiments were a strong indication that other properties of photon pairs could be generalized to large number of photons, and could lead to interesting applications in metrology.

One such application of PDC is squeezing, which is a feature of most photon-pair generation processes [8, 9]. Squeezing is characterized by reduced noise in one quadrature of the electromagnetic field at the expense of the other quadrature, like in Fig. (1.2), where different states of light are represented in the phase space with quadratures X and P . The squeezed quadrature is utilized in interferometry to mitigate the deleterious effects of vacuum noise [10, 11]. PDC theory predicts that a higher gain of parametric amplification

leads to a stronger level of squeezing [12]. In other words, twin beams with a large number of photons should exhibit tremendous squeezing.

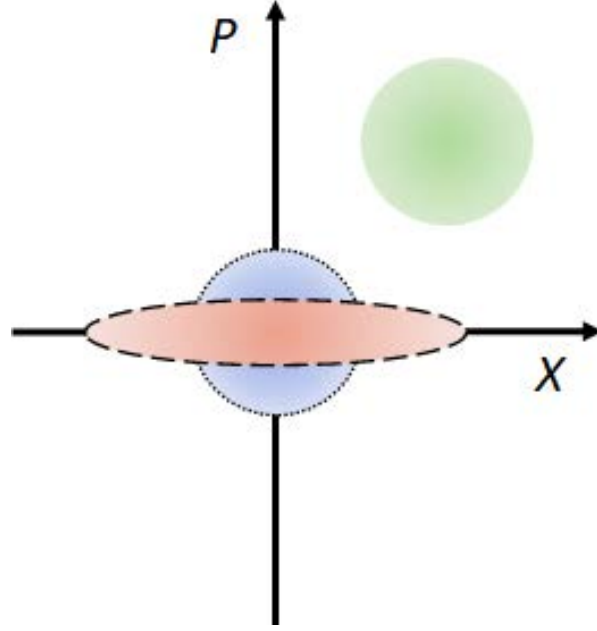


Figure 1.2: Cartoon representation of different states of light in the phase space, with the axes the quadratures X and P . The vacuum state (blue, dotted) resides at the origin, with a non-zero and equal uncertainty in both quadratures. The coherent state (green, no edge) has a non-zero amplitude (radius from the origin to the center of the circle). The squeezed vacuum (red, dashed) is centered at the origin, with unequal uncertainties in orthogonal quadratures. All states represented are minimum-uncertainty states.

Another quantum-metrological application of PDC is $SU(1,1)$ interferometry. $SU(1,1)$ interferometers are like conventional interferometers where the beam splitters have been replaced by optical parametric amplifiers (OPA), see Fig. (1.3). In an $SU(1,1)$ interferometer, the sensitivity scales favorably with intensity compared to a conventional interferometer with classical light [13, 14]. This favorable scaling is promising for applications where one wants to limit the intensity of the light traversing the sample, to avoid damage or unwanted nonlinear effects.

Spontaneous PDC is widely used in radiometry to calibrate the quantum efficiency of single photon detectors. The standard resides in the fact that photons are produced in

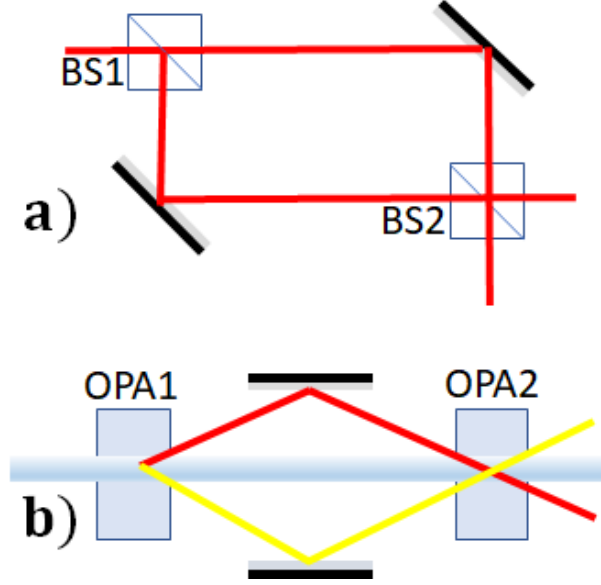


Figure 1.3: Schematic representation of: a) a Mach-Zehnder interferometer, composed of two beamsplitters BS1 and BS2; b) an $SU(1,1)$ interferometer.

pairs (but in different modes) [15–17]. The detection of a photon at an ancilla detector necessarily indicates the presence of a photon at the detector under test. The brightness of PDC itself can serve as a primary standard as well. In PDC, photon pairs are emitted as a result of the coupling between the pump laser and the down-converted modes. At the input of the nonlinear medium, the latter modes are in their vacuum states, whose properties are well known from the framework of quantum mechanics, and obtained from first principles [12]. Therefore, since it can be tied to the properties of the vacuum fluctuations, the brightness of PDC can serve as a primary standard for radiometry.

All the applications of PDC to metrology presented so far offer their range of challenges, both theoretical and experimental. The work presented in this thesis aims to solve those challenges. The higher the squeezing of a mode, the larger the metrological advantage. Hence, one prefers one strongly squeezed mode over many modes that are weakly squeezed. In chapter 2, we produce high-gain PDC in a single frequency-mode, constituting an important step towards applying it in interferometry. In chapter 3 and 4, we provide further theoretical and experimental insights into understanding the modal structure of PDC in the high-gain regime. The high-gain PDC setup in chapters 2 and 3 is based on an $SU(1,1)$ interferometer. In chapter 5, we theoretically explore a strategy to mitigate the

effects of losses in an $SU(1,1)$ interferometer and provide a discussion about the figures of merit used to quantify interferometers. Finally, from the insight that PDC spectral brightness can be tied to the properties of electromagnetic vacuum, we demonstrate in chapter 6 that high-gain PDC can be used as a primary standard for radiometry, whose brightness can be derived from first principles, akin to blackbody radiation.

This introduction aims to provide the necessary concepts to fully understand the work presented in this thesis. In section 1.1, we introduce a quantum-mechanical description of squeezing, which constitutes a toy-model for PDC generated in a single mode. In particular, we take a look at the photon-number statistics of squeezed states. We briefly cover parametric down-conversion from the angle of nonlinear optics, and show how the spectrum of PDC relates to the properties of the pump laser and the nonlinear medium. We also apply a Schmidt-mode decomposition to multimode PDC, and present its relevance to quantum-optical applications. In section 1.2, we discuss the phase sensitivity of conventional and $SU(1,1)$ interferometers. In section 1.3, we derive the number of photons for high-gain PDC produced from a planewave monochromatic pump.

1.1 Squeezed vacuum

Squeezed states of light are known to exhibit reduced noise in one of their field quadratures, in contrast to classical sources of light. This feature makes them attractive for metrological applications in optics, but also in other quantum systems [18, 19]. In this section, we examine some features of quantum states of light in order to determine the photon-number statistics of squeezed vacuum states. In the following chapters, we will use the formalism of squeezing to contextualize, analyze and discuss the results presented. The connection between squeezing, quadratures, entanglement and photon-number statistics is of particular relevance.

A simple squeezing Hamiltonian constitutes a toy-model for PDC in order to better understand its photon-number statistics. However, such a model usually does not describe PDC produced simultaneously in multiple modes. I also present the Schmidt-mode decomposition, a tool to meaningfully describe spontaneous PDC in the multimode configuration. This decomposition provides a set of modes that can be squeezed independently according to our toy model.

1.1.1 Quantum-mechanical description of squeezed vacuum

One function that maps a quantum state into phase space, comprising the two quadratures of the electromagnetic field, is the Wigner quasiprobability distribution [2]. When represented in phase space, the state appears *squeezed*—thus the name—adopting an elongated shape. The squeezed state is a minimum-uncertainty state, bounded by the Heisenberg uncertainty principle for the product of the noise for the two orthogonal quadratures. Importantly, squeezed states exhibit reduced noise in one of the quadratures at the expense of excess noise in the orthogonal quadrature [20]. This form of squeezing is called quadrature squeezing. Different types of squeezing are pictured Fig. (1.4). Number-phase squeezed states, for example, are squeezed along the polar coordinates of the phase space, which correspond to the amplitude of the field (the radius) and its phase (polar angle). Alternatively, squeezing can occur between two quadratures belonging to two different modes of the electromagnetic field. This is called two-mode squeezing. We customarily call those two modes the signal and the idler. We will derive the basic properties of squeezed states in relevance to the work presented in this thesis.

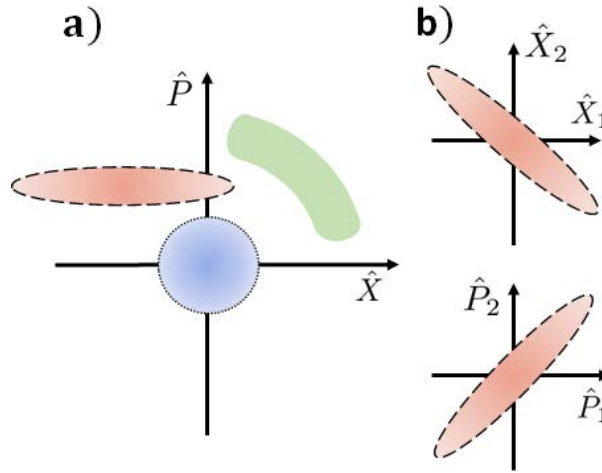


Figure 1.4: Cartoon representation of different types of squeezing in terms of the \hat{X} and \hat{P} quadratures. a) The quadrature squeezed state (red, dashed) and the number-phase squeezed state (green, no edge) are minimum uncertainty states like the vacuum state (blue, dotted). b) Two-mode squeezed states exhibit squeezing in the $\{\hat{X}_1, \hat{X}_2\}$ space, and as well in the $\{\hat{P}_1, \hat{P}_2\}$ space but at a $\pi/2$ dephasing.

We set up an idealized interaction Hamiltonian in the form of

$$\hat{H} = \frac{i\hbar\zeta}{2}\hat{a}^{\dagger 2} + \text{h.c.}, \quad (1.1)$$

where the creation and annihilation operators \hat{a}^\dagger and \hat{a} satisfy the commutation relation $[\hat{a}, \hat{a}^\dagger] = 1$. The coupling parameter $\zeta = re^{i\theta}$ is complex. In the context of PDC, the parameter r is connected to the gain of the OPA, which depends on the intensity of the pump, and θ includes the laser phase. The abbreviation “h.c.” denotes the Hermitian conjugate. This Hamiltonian generates single-mode squeezing due to the nonlinearity of the interaction, in contrast to the two-mode squeezing Hamiltonian, which is linear in each mode.

One can thus use the Heisenberg equation of motion and the commutation relation to find how \hat{a} and \hat{a}^\dagger evolve in time t under this Hamiltonian:

$$\frac{d\hat{a}}{dt} = \frac{i}{\hbar}[\hat{H}, \hat{a}] = \zeta\hat{a}^\dagger, \quad (1.2a)$$

$$\frac{d\hat{a}^\dagger}{dt} = \frac{i}{\hbar}[\hat{H}, \hat{a}^\dagger] = \zeta^*\hat{a}, \quad (1.2b)$$

and by taking the second derivative, we find a differential equation whose solution reads

$$\hat{a}(t) = \hat{a}(0) \cosh(rt) + e^{i\theta}\hat{a}^\dagger(0) \sinh(rt), \quad (1.3a)$$

$$\hat{a}^\dagger(t) = \hat{a}^\dagger(0) \cosh(rt) + e^{-i\theta}\hat{a}(0) \sinh(rt), \quad (1.3b)$$

a relation that is often called a Bogolyubov transformation [21]. It can be readily verified that the solutions of eq. (1.3) satisfy $[\hat{a}, \hat{a}^\dagger] = 1$ at all times, by making use of the hyperbolic relation $\cosh^2(x) - \sinh^2(x) = 1$.

A squeezed vacuum state is created when the squeezing Hamiltonian of eq. (1.1) is applied to the vacuum $|0\rangle$, represented here in the number basis. The average number of photons of squeezed vacuum is not zero, despite its name:

$$\langle n \rangle = \langle 0 | \hat{a}^\dagger(t) \hat{a}(t) | 0 \rangle = \sinh^2(rt), \quad (1.4)$$

where we used the usual rules of \hat{a} and \hat{a}^\dagger in the number basis. It is apparent that the number of photons grows exponentially with the amplitude of the coupling parameter r and the interaction time t , as plotted in Fig. (1.5).

Squeezing is best understood in the language of quadratures. The quadratures are described by quadrature operators that can adopt the form $\hat{X} = (\hat{a} + \hat{a}^\dagger)/\sqrt{2}$ and $\hat{P} =$

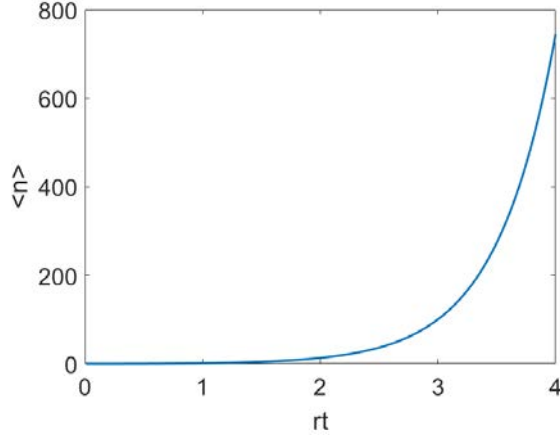


Figure 1.5: Average number of photons $\langle n \rangle$ with respect to the gain product rt

$i(\hat{a} - \hat{a}^\dagger)/\sqrt{2}$ [10]. The field quadratures behave like the real and imaginary parts of the electric field, which correspond to 0 and $\pi/2$ angle in the phase space, respectively. We will consider the vacuum state $|0\rangle$ as an example. The expectation value for the each quadrature reads $\langle X \rangle = \langle P \rangle = 0$. The variance, however, does not vanish, as $\langle (\Delta X)^2 \rangle = \langle (\Delta P)^2 \rangle = 1/2$. Therefore, the electromagnetic vacuum state exhibits a fluctuating electric field that averages to zero. In addition, those fluctuations do not depend on the phase. Using the actual definition for the electric field operators, it can be found the vacuum is a minimum uncertainty state, as prescribed by Heisenberg's uncertainty principle. Here, we find that the product of variances $\langle (\Delta X)^2 \rangle \langle (\Delta P)^2 \rangle = 1/4$, which is the Heisenberg limit.

Using our definitions for the quadratures, along with eq. (1.3), we obtain a time-evolved quadrature operator as

$$\hat{X}(t) = \hat{X}(0)e^{rt}, \quad (1.5a)$$

$$\hat{P}(t) = \hat{P}(0)e^{-rt}, \quad (1.5b)$$

where we used $\theta = 0$ for simplicity. In turn, for a vacuum input, the standard deviation (square root of the variance) evolves as

$$\sqrt{\langle (\Delta X)^2 \rangle}(t) = \sqrt{\langle (\Delta X)^2 \rangle}(0)e^{rt}, \quad (1.6a)$$

$$\sqrt{\langle (\Delta P)^2 \rangle}(t) = \sqrt{\langle (\Delta P)^2 \rangle}(0)e^{-rt}. \quad (1.6b)$$

The noise in the X quadrature is found to increase exponentially under the squeezing Hamiltonian, while the noise in the P quadrature decreases. Notably, the product of

the variance does not change over time. Therefore, the state produced by the squeezing operator is also a minimum-uncertainty state, where the increased noise in one quadrature serves to compensate the noise reduction in the other. This is the most widely recognized feature of squeezed states. Squeezed states can also be produced with a coherent state input, in which case the output state will be a squeezed coherent state, with a non-zero average electric field, as pictured in Fig. (1.4a).

The Hamiltonian of eq. (1.1) describes a process where two photons are being created in the same mode. A Hamiltonian where the two photons are produced in different modes, having the form

$$\hat{H} = i\hbar\zeta\hat{a}^\dagger\hat{b}^\dagger + \text{h.c.}, \quad (1.7)$$

and applied to the vacuum state, will produce a two-mode squeezed state. Using a treatment similar to the single-mode case, we find that the annihilation operators adopt the form

$$\hat{a}(t) = \hat{a}(0) \cosh(rt) + \hat{b}^\dagger(0) \sinh(rt), \quad (1.8a)$$

$$\hat{b}(t) = \hat{b}(0) \cosh(rt) + \hat{a}^\dagger(0) \sinh(rt), \quad (1.8b)$$

where we assumed that ζ is real, for simplicity. In that case, the squeezing is manifest in the correlation and anti-correlation between the quadratures. For example, if we consider a vacuum state, the X quadratures for the a and b modes exhibit no correlation. A two-mode squeezing operation in the form of eq. (1.8) will correlate the X quadratures at the expense of the P quadratures correlation, following the relation

$$\hat{X}_a(t) - \hat{X}_b(t) = (\hat{X}_a(0) - \hat{X}_b(0))e^{-rt} \quad (1.9a)$$

$$\hat{P}_a(t) - \hat{P}_b(t) = (\hat{P}_a(0) - \hat{P}_b(0))e^{rt}. \quad (1.9b)$$

The two-mode squeezed vacuum state for modes a and b is entangled in the X and P degrees of freedom. As the coupling parameter r gets larger, $\hat{X}_a(t) - \hat{X}_b(t)$ approaches a Dirac delta function centered at $t = 0$. In that case, the state is maximally entangled. This state is an example of an EPR state, as proposed by Einstein, Podolsky and Rosen in their landmark paper to address the oddities of quantum mechanics [22].

Photon pairs being created in a single mode a produce squeezing, whereas photon pairs being generated in two modes a and b produce entanglement. Let's consider a new set of modes $c = (a + b)/\sqrt{2}$ and $d = (a - b)/\sqrt{2}$. Such a mode transformation from $\{a, b\}$ to $\{c, d\}$ can be accomplished by a beam splitter. Using the operators a and b as defined in eq. (1.8), we see that c and d actually undergo a single-mode squeezing transformation

under the action of the two-mode squeezed state acting on a and b . In that case, entanglement and squeezing are the two sides of the same coin. Using a similar reasoning, in this thesis, I will use the language of “squeezing” and “entanglement” interchangeably to describe similar phenomena. For example, it is customary to call sub-shot-noise photon-number correlation “twin-beam squeezing”.

1.1.2 Correlations in the second order

There are various ways to quantify the level of correlation in the second-order of the electric field operators, depending on the situation. In the context of this work, we consider the degree of second-order coherence $g^{(2)}$ and the noise-reduction factor (NRF).

The degree of second-order coherence, or normalized intensity correlation between the fields i and j , is a measure of the pairwise photon correlation between two modes, or within a single mode. It is defined, following the work of pioneer Roy Glauber [23, 24] as:

$$g_{ij}^{(2)}(t_i, t_j) = \frac{\langle \hat{a}_i^\dagger(t_i) \hat{a}_j^\dagger(t_j) \hat{a}_j(t_j) \hat{a}_i(t_i) \rangle}{\langle \hat{a}_i^\dagger(t_i) \hat{a}_i(t_i) \rangle \langle \hat{a}_j^\dagger(t_j) \hat{a}_j(t_j) \rangle}. \quad (1.10)$$

It can be interpreted as a measure of the likelihood that two photons bring an absorber to an excited state, at two different times t_i and t_j . It is often derived starting from this principle. To keep things general, the location and time of measurement are left as variables of the field. The two photons can belong to the same field, in which case $g^{(2)}$ is a form of autocorrelation. The introduction of $g^{(2)}$ was significant in understanding the photon-bunching effect as observed by Hanbury-Brown and Twiss in their landmark intensity-correlation measurement [25]. In this experiment, it was discovered that a thermal source of light exhibits super-Poissonian fluctuations. With a proper mathematical treatment of the field, it was shown that for thermal fields, $g^{(2)}$ is straightforwardly connected to the degree of first-order coherence. This means that $g^{(2)}$ can be used to measure the coherence length of a field (or between two fields) by varying the time of detection between the two absorbers. It was also shown that all classical light must obey $g_{i,j}^{(2)} \geq 1$. Any deviation from this inequality is a sign of nonclassicality [26]. For example, a single photon, which can’t be described from classical optics, will exhibit $g^{(2)} = 0$. This is a consequence of the fact that a single photon will never trigger two detectors simultaneously.

The intensity autocorrelation is often expressed as $g^{(2)}(\tau = t_j - t_i)$, where the field overlaps itself with a temporal delay τ . $g^{(2)}(\tau)$ strongly depends on the state of light under scrutiny, and gives precious information about the field's photon number fluctuations [20]. For single-mode radiation, and when $\tau = 0$, the definition of $g^{(2)}(\tau)$ simplifies to:

$$g^{(2)}(\tau = 0) = \frac{\langle \hat{a}^\dagger \hat{a}^\dagger \hat{a} \hat{a} \rangle}{\langle \hat{a}^\dagger \hat{a} \rangle^2}, \quad (1.11)$$

where we dropped the time dependence of the creation and annihilation operators. For single-mode squeezed vacuum, using equation (1.3) we find

$$g^{(2)}(\tau = 0) = 3 + 1/\langle n \rangle. \quad (1.12)$$

In the case of two-mode squeezed vacuum, the same procedure can be applied to derive the photon-number statistics in each channel:

$$g_{aa}^{(2)}(\tau = 0) = g_{bb}^{(2)}(\tau = 0) = 2, \quad (1.13a)$$

$$g_{ab}^{(2)}(\tau = 0) = \frac{\langle \hat{a}^\dagger \hat{b}^\dagger \hat{b} \hat{a} \rangle}{\langle \hat{a}^\dagger \hat{a} \rangle \langle \hat{b}^\dagger \hat{b} \rangle} = 2 + 1/\langle n \rangle, \quad (1.13b)$$

for the autocorrelation and the crosscorrelation, respectively. The fluctuations in each channel of two-mode squeezed vacuum, taken individually, are thermal, with $g^{(2)} = 2$ [27], while the correlations between them are quantum in nature.

The Hanbury-Brown and Twiss apparatus, in its conventional form, necessitates two detectors, whose signals are multiplied. In the case of a single source, the field is sent to a beamsplitter, whose output ports point to the detectors. One detector's position is varied to measure $g^{(2)}$ as a function of the time difference. To measure the degree of second-order correlation of a single field at zero delay, it is sufficient to use a single bucket detector that measures a quantity proportional to $\langle n \rangle$, the average number of photons. We can straightforwardly move from the Hanbury-Brown and Twiss interferometer to the single bucket detector configuration since the beamsplitter has no impact on the statistics of $\langle n \rangle$ of the input source field [27].

The noise-reduction factor (NRF) is a measure of the photon-number correlation between two fields 1 and 2. It is defined as

$$\text{NRF} = \frac{\langle (\Delta(n_2 - n_1))^2 \rangle}{\langle n_2 + n_1 \rangle}. \quad (1.14)$$

The NRF is a measure of the fluctuations of the photon-number difference between the two fields, normalized to the fluctuations of a Poissonian field with the same average total photon number. For example, if a coherent state (which by definition exhibits Poissonian statistics in the photon number), was split with a 50:50 beamsplitter, the NRF measured by two detectors in the output ports would be equal to unity. For the same reason, the NRF measured for two coherent states with equal average photon number would also be unity. The NRF can be expressed in terms of cross-and-autocorrelations $g^{(2)}$, simply by using the commutation relations for creation and annihilation operators. Indeed, using a Cauchy-Schwarz type of inequality, and the inequality $2ab < (a+b)^2$ for real a and b , it can be shown that, for classical fields, $g_{11}^{(2)} + g_{22}^{(2)} \geq 2g_{12}^{(2)}$ [26]. We thus find that sub-shot-noise photon-number correlation (NRF < 1) is a proof of nonclassicality. Two-mode squeezed vacuum exhibits perfect photon-number correlation, such that NRF = 0.

1.1.3 Parametric down-conversion

Parametric down-conversion (PDC) is a three-wave nonlinear optical process where photons of frequency ω_p , labeled p for pump, get converted into a pair of daughter photons called the signal and the idler, of frequency ω_s and ω_i , respectively, following the rule for energy conservation $\omega_p = \omega_s + \omega_i$. This process occurs in a material with second-order susceptibility $\chi^{(2)}$ [1]. The type of PDC depends on the non-vanishing elements of the $\chi^{(2)}$ tensor relating the three fields, as well as on the birefringence of the material, described completely by the $\chi^{(1)}$ tensor. For uniaxial birefringent material, type-I PDC is the interaction where the pump, signal and idler fields have polarizations extraordinary, ordinary and ordinary, respectively. There exists other type of phase-matching for three-wave nonlinear processes, involving other combinations of polarizations for the three fields.

The angular and frequency spectrum of PDC is determined, in first approximation, by the properties of the pump laser, and by the phase-matching function of the crystal. The photography in Fig. (1.6) shows the angular and frequency coupling of type-I PDC. We say the phase-matching condition is fulfilled when $\kappa_p - \kappa_s - \kappa_i = 0$, where κ is the longitudinal part (along the z -axis) of the wavevector \mathbf{k} of magnitude $k = 2\pi n(\lambda)/\lambda$, where n is the refractive index and λ_x the wavelength in vacuum.

This condition leads to optimal conversion efficiency. Phase matching implies that the oscillatory contributions to the amplitudes from different parts of the medium add up constructively. When the phase-matching condition is not fulfilled, the fields interfere destructively; for a large phase mismatch, no light is produced at all. Phase matching is adjusted by tilting the angle of the birefringent medium, thereby varying the extraordinary

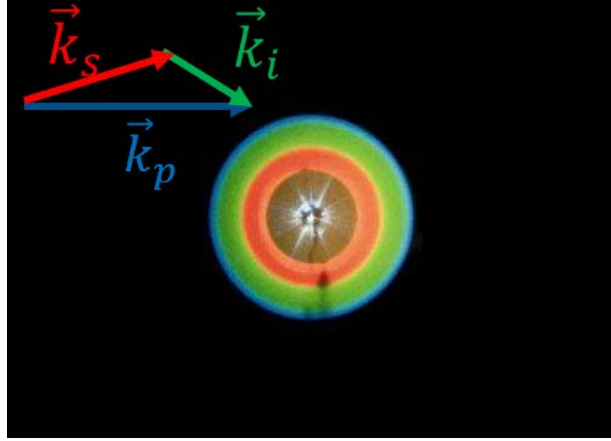


Figure 1.6: Photography of a Type-I PDC interaction. The phase-matched interaction, as exemplified by the vectors, typically leads to the highest PDC efficiency. and an illustration of a phase-matched interaction. In practice, a thin nonlinear-medium will relax the phase-matching condition, leading to a wide frequency-angular spectrum, like in the photography. (Illustration credit: Alan Migdall and NIST).

index of refraction (which is a factor of the wavevector k). For an infinite transverse nonlinear medium, the transverse momentum \mathbf{q} of the wavevector is conserved.

In the spontaneous regime of PDC, the photon pairs are generated according to a joint probability amplitude function for the signal and for the idler called the biphoton amplitude [28]. The biphoton amplitude is the product of the pump spectral function (rewritten in terms of signal and idler frequency and wavevectors by virtue of energy conservation) and the phase-matching function, which depends only on the properties of the $\chi^{(2)}$ material. In the work presented in this thesis, we are interested in the properties of PDC generated in the high-gain regime. In the spontaneous regime of PDC, each photon-pair generation is an independent event. The spontaneous regime of PDC is characterized by a linear dependence of the PDC photons output with respect to the pump laser intensity at the input. This is the first term in the series expansion of the photon number given by eq. (1.4) in terms of the gain rt . When the coupling between the pump, signal and idler is strong enough, for example by increasing the intensity of pump laser, the photon pairs generated in the nonlinear material can trigger the generation of other new photon pairs. In this high-gain regime, the number of PDC photons increases exponentially with the intensity of the pump, like in Fig. (1.5). The derivation of the number of photons for PDC at arbitrary gain and for a planewave monochromatic undepleted pump is found in section 1.3.

PDC is a photon-pair generator for which the squeezing Hamiltonian of eq. (1.1) can be used as a toy-model. In particular, many of the properties of single- and two-mode squeezed states, such as the number of photons of eq. (1.4) and the photon-number statistics, apply straightforwardly to PDC produced in a single mode. However, the spectral and statistical properties of high-gain PDC produced in the laboratory are not entirely understood.

In the experiments presented throughout this thesis, we mostly use β -baryum borate (BBO) as a $\chi^{(2)}$ nonlinear material to produce PDC. The BBO crystal allows to reach the high-gain regime of PDC using a high-energy pulsed laser, due to its high damage threshold.

1.1.4 Multimode radiation and mode decomposition

In this thesis, we call radiation “multimode” when it is produced in multiple modes for the signal and for the idler. Free-space OPAs naturally produce multimode radiation. “Multimode” may refer to various degrees of freedom, typically the spatial and temporal ones. Some applications, especially in phase estimation, require—or are facilitated by—PDC being produced mainly in a single mode. We address this challenge in Chapter 2. At the same time, multimode light is attractive for several applications, mostly in the field of imaging [29–31]. For example, the photon-number correlation between the signal and idler allows for sub-shot-noise imaging of a faintly absorbing object, by making use of the NRF defined earlier in this chapter. In addition, theory predicts that the multimode spontaneous PDC can be decomposed into an ensemble of independent two-mode squeezed states, which could in turn be used as a resource in quantum information applications [32].

An average over many modes does not exhibit the same photon-number statistics as each mode taken separately. This is because the number of photons is an independent random variable for each mode, leading to a Poisson distribution for the number of photons when many modes are present. Therefore, for highly multimode squeezed states, the degree of second-order coherence $g^{(2)}$ will tend to unity. This feature can be used to measure the number of modes in multimode squeezed states [33, 34]. We use this method in chapter 2.

A measurement of NRF below unity is an indication, but not a proof, of two-mode quadrature squeezing. For light generated in an OPA into free space, the photon-number correlation between the signal and idler fields is in principle perfect. In practice, ideally, the measured NRF should only be limited by the noise of the detectors. However, while the $\text{NRF} < 1$ indicates non-classicality, it is not straightforward to isolate the pairs of modes that exhibit two-mode squeezing. In other words, it is challenging to measure squeezing directly from the collection of signal and idler modes. Filters, such as pinholes in the

spatial domain, or narrowband filter in the frequency domain, can be used as a brute-force method to recover a pair of squeezed modes. However, there is no guarantee that the filter will only suppress photons from undesired modes. In addition, the filter may suppress photons from the targeted modes, in a way that will deteriorate the degree of squeezing.

Any bipartite pure state can be decomposed into Schmidt modes [35, 36]. The Schmidt modes (or Schmidt functions) $\{\psi_n(x_1)\}$ for a particle with variable x_1 , and $\{\chi_n(x_2)\}$ for a particle with variable x_2 , uniquely describe any two-variable function such that

$$\Psi(x_1, x_2) = \sum_n \lambda_n^{1/2} \psi_n(x_1) \chi_n(x_2), \quad (1.15)$$

where the Schmidt functions form a complete orthonormal set, and $\sum_n \lambda_n = 1$ if $\int \int x_1 x_2 |\Psi(x_1, x_2)|^2 = 1$. Those properties can be straightforwardly translated to the discrete variables.

The Schmidt-mode decomposition of a bipartite wavefunction provides valuable information about the state. In particular, there is a close connection between the Schmidt number (defined as the spread of λ_n) and the degree of entanglement in the state [37, 38]. In addition, the Schmidt modes obtained by applying eq. (1.15) on the Hamiltonian for spontaneous multimode PDC are squeezed pair-wise, and therefore offer a potentially large set of two-mode squeezed states. In that regard, the Schmidt-mode decomposition of spontaneous PDC is the diagonalization of the Hamiltonian corresponding to the down-conversion process. In practice, for discrete variables, or numerical simulations, the Schmidt modes are obtained by simply applying a singular value decomposition on the Hamiltonian.

Parts of this thesis deal with understanding the behaviour of high-gain PDC using the Schmidt-mode formalism. In particular, in chapters 2 and 3, we derive spectral and statistical properties of high-gain PDC by neglecting time-ordering effects in the PDC Hamiltonian. This approximation allows us to calculate the Schmidt modes efficiently and compare experimental results with simulated ones. In chapter 4, we provide a more complete model for high-gain PDC that comprises time-ordering, and accurately predicts typical PDC behaviour, such as the broadening of the angular (momentum) and frequency spectrum of PDC as the gain increases.

1.2 Phase sensitivity

The phase-sensitivity of an interferometer is the smallest phase-change that will lead to a signal change above the noise level [39]. SU(1,1) interferometers, which typically comprise

two OPAs, exhibit a phase sensitivity that scales favorably with the number of photons inside the interferometer, when compared to conventional interferometers [13]. In this section, we will define the phase-sensitivity of interferometers and briefly introduce SU(1,1) interferometers. Those concepts will be used in chapter 5.

Let us consider a lossless Mach-Zehnder interferometer with a single laser input. The intensity at the output ports as a function of the interferometer phase ϕ reads

$$I_1 = I_{\text{in}}(T_1 T_2 + R_1 R_2 - 2\sqrt{T_1 T_2 R_1 R_2} \cos \phi), \quad (1.16a)$$

$$I_2 = I_{\text{in}}(T_1 R_2 + R_1 T_2 + 2\sqrt{T_1 T_2 R_1 R_2} \cos \phi), \quad (1.16b)$$

where I_{in} is the input intensity, and T_j and R_j are the transmittance and reflectance of the j -th beamsplitter of the interferometer. The smallest measurable phase $\Delta\phi$ by virtue of variations of intensity at the output of the interferometer $\frac{\partial I_O}{\partial \phi}$ is given by

$$\Delta\phi = \frac{\Delta I_O}{\left| \frac{\partial I_O}{\partial \phi} \right|}, \quad (1.17)$$

where ΔI_O is the noise of the measured intensity signal and I_O denotes the measured output intensity, for either output port, or the difference of their intensities, for example. This equation is obtained from Gaussian error propagation. More sophisticated methods like the Fisher information can give a better estimate of the phase sensitivity. Using the fact that an ideal laser exhibits Poissonian statistics in the number of photon, and that the intensity of light is proportional to the number of photons, we can infer that $\Delta I_O \propto \sqrt{n}$, with n the average number of photon in the detection port. Likewise, the scaling of $\left| \frac{\partial I_O}{\partial \phi} \right|$, at the optimal interferometer phase of $\phi = \pi/2$, follows a scaling with n . We therefore find that the $\Delta\phi$ follows, at best, a $1/\sqrt{n}$ scaling. The sensitivity can be improved by using various strategies, but the shot-noise-limited $1/\sqrt{n}$ scaling cannot be exceeded without resorting to strategies based on nonclassical light or measurements [40]. Parts of the work presented in this thesis is motivated by potential enhancement in phase-sensitivity provided by quantum light.

It was discovered, from the framework of quantum Fisher information, that the NOON state of light is a prime example for below-shot-noise interferometry, with a phase-sensitivity following a $1/n$ scaling [40–42]. This $1/n$ scaling is conventionally called the Heisenberg limit. Other states of light and measurement strategies can reach the Heisenberg limit.

The $SU(1,1)$ interferometer is an interferometer where the beamsplitting operation is performed by OPAs, see Fig. 1.3. The name stems from the group-theoretical relation between the input and output for the field operators, which differs from the more conventional $SU(2)$ interferometers, that are solely based on beamsplitters and mirrors, like the Mach-Zehnder interferometer. OPAs are devices that amplify a signal, by taking optical energy from a pump channel, typically a well-characterized and stable laser beam. The pump and signal beams are coupled to an idler mode, following energy and momentum conservation, as discussed in the previous section. This coupling is responsible for added noise in the amplifier. OPAs operated without any light at the signal or idler inputs spontaneously produce photon pairs in the output modes. However, a coherently fed OPA can lead to perfect destructive interference, with vacuum states in the output ports. For optimal results, the $SU(1,1)$ is operated for destructive interference. The second OPA of the interferometer annihilates the photons created by the first OPA. We have seen in eq. (1.4) that the number of photons generated in a parametric down-conversion process grows exponentially with the parametric gain of the OPA. This means that any dephasing between the signal and the idler arm within the interferometer will lead to a large number of photons at the output of the interferometer. This is a result of the phase and amplitude correlation between the signal and idler modes in the two-mode squeezing operation occurring within the OPAs. Without that quantum correlation, the phase sensitivity could not reach the Heisenberg level.

In this thesis, we examine theoretically and experimentally explore $SU(1,1)$ interferometers. Namely, we devise a strategy to reduce the number of modes in an $SU(1,1)$ interferometer operated in the high-gain regime, thereby facilitating its usage. We also theoretically explore the effects of gain unbalancing between the two OPAs can improve the performance of the spectrometer, as well as raise issues about the conventional figures of merit in interferometry.

1.3 High-gain parametric down-conversion

In this section, we derive the number of photons for high-gain PDC with a planewave pump. The objective is two-fold. Firstly, the metrological applications of PDC require that we rigorously keep track of approximations and the limits of the theoretical model. In particular, in chapter 6, we directly use the results obtained from this derivation, and discuss the approximations in the supplementary material. Secondly, the derivation method presented in this section is the starting point for the derivation in chapter 4, where we

explore high-gain PDC with a non-planewave pump laser.

As a first step, we quantize the electromagnetic field in dispersive media. With this definition of the quantum operators, we solve the Heisenberg's equation of motion in the nonlinear crystal for PDC at arbitrary gain. The main assumption here is that it is sufficient to consider a planewave monochromatic pump if the pump's angular and frequency spectra are much narrower than that of the downconverted light's [43]. Such an assumption would not be valid for, say, a pump pulse below the picosecond range, or a pump strongly focused into the nonlinear material. Quantifying the effect of going from planewave monochromatic pump to a non-planewave non-monochromatic pump on the spectrum and photon-number distribution of PDC is a work in progress, partially addressed in chapters 3 and 4.

1.3.1 Quantization of the electromagnetic field in a medium

This derivation is inspired from Landau and Lifshitz's book on Electrodynamics of continuous media [44], as well as on Klyshko's book on Photons and nonlinear optics [12].

The quantization of the electromagnetic field can be accomplished if we know the total energy in the system, and associate canonical variables for it. For a dispersive medium, deriving the energy carried in the field is not straightforward. The Poynting theorem for an ideal dielectric reads

$$-\frac{\partial u}{\partial t} = \nabla \cdot \mathbf{S}, \quad (1.18)$$

and states that the rate of change of the energy density u is equal to the divergence of the Poynting vector, defined as usual by $\mathbf{S} = \mathbf{E} \times \mathbf{H}$, with \mathbf{E} and \mathbf{H} the time-varying electric and magnetic field, respectively. From Maxwell's equations,

$$-\nabla \cdot \mathbf{S} = \mathbf{H} \cdot \frac{\partial \mathbf{B}}{\partial t} + \mathbf{E} \cdot \frac{\partial \mathbf{D}}{\partial t}. \quad (1.19)$$

In the specific case of a non-dispersive material, we find

$$-\nabla \cdot \mathbf{S} = \frac{\partial}{\partial t} \left[\frac{1}{2} (\epsilon \mathbf{E}^2 + \mu \mathbf{H}^2) \right], \quad (1.20)$$

where we can recognize, from eq. (1.18), that the energy density is $u = (\epsilon \mathbf{E}^2 + \mu \mathbf{H}^2)/2$, where ϵ is the permittivity and μ is the permeability. However, for a dispersive dielectric, we must use the right-hand side of eq. (1.19) to compute the rate of change of the energy density. In

what follows, we will find an approximate expression for the total electromagnetic energy in a dispersive material in terms of the dispersion relation. So far, all the fields that we have considered were the real fields. Let us express the real fields (from now on denoted like $\tilde{\mathbf{E}}$) in terms of complex exponentials with positive and negative frequency ω_0 , for example

$$\tilde{\mathbf{E}} = \frac{1}{2}(\mathbf{E} + \mathbf{E}^*) = \frac{1}{2}(\mathbf{E}_0(t)e^{-i\omega_0 t} + \mathbf{E}_0^*(t)e^{+i\omega_0 t}), \quad (1.21)$$

where $\mathbf{E}_0(t)$ is an envelope that varies slowly with respect to $e^{-i\omega_0 t}$. The second term in the right-hand side of eq. (1.19) now reads

$$\begin{aligned} \tilde{\mathbf{E}} \cdot \frac{\partial \tilde{\mathbf{D}}}{\partial t} &= \frac{1}{2}(\mathbf{E} + \mathbf{E}^*) \cdot \frac{1}{2}(\dot{\mathbf{D}} + \dot{\mathbf{D}}^*) \\ &= \frac{1}{4}(\mathbf{E}\dot{\mathbf{D}}^* + \mathbf{E}^*\dot{\mathbf{D}}), \end{aligned} \quad (1.22)$$

where in the last equality we have used the rotating-wave approximation, thereby removing the terms that oscillate at twice the optical frequency. The following step, which amounts to an expansion of ϵ into orders of the electric field, can be accomplished concisely if we introduce an operator \hat{f} according to

$$\frac{\partial \mathbf{D}}{\partial t} = \hat{f}\mathbf{E} = \widehat{\frac{\partial}{\partial t}\epsilon}\mathbf{E}, \quad (1.23)$$

and if $\mathbf{E}_0(t)$ is a constant of time (meaning that \mathbf{E} is monochromatic), then the operator yields the eigenvalue $\hat{f}\mathbf{E} = f(\omega_0)\mathbf{E}$, with $f(\omega_0) = -i\omega_0\epsilon(\omega_0)$. Note that we are interested in the unperturbed Hamiltonian, so we are not considering the nonlinear susceptibility yet. Using the operator \hat{f} and keeping only the first two terms in the Taylor expansion:

$$\begin{aligned} \frac{\partial \mathbf{D}}{\partial t} &= \hat{f}\mathbf{E} \\ &= f(\omega_0)\mathbf{E}_0(t)e^{-i\omega_0 t} + i\left.\frac{df}{d\omega}\right|_{\omega_0} \frac{d\mathbf{E}_0(t)}{dt}e^{-i\omega_0 t}. \end{aligned} \quad (1.24)$$

Replacing ω_0 with ω , and $f(\omega)$ with $-i\omega\epsilon(\omega)$, we find

$$\frac{\partial \mathbf{D}}{\partial t} = -i\omega\epsilon(\omega)\mathbf{E} + \frac{d(\omega\epsilon)}{d\omega} \frac{d\mathbf{E}_0(t)}{dt}e^{-i\omega t}. \quad (1.25)$$

Repeating this procedure for \mathbf{D}^* , we can now reexpress eq. (1.22) as

$$\mathbf{E} \cdot \frac{\partial \mathbf{D}}{\partial t} = \frac{1}{4} \frac{d(\omega\epsilon)}{d\omega} \frac{d}{dt}(\mathbf{E}^* \cdot \mathbf{E}), \quad (1.26)$$

where we assumed that ϵ is real. This form, with the time derivative, will allow us to extract the electromagnetic energy, just like from the Poynting's theorem. Repeating this procedure again for the magnetic field, we obtain that the total time-averaged electromagnetic energy $U_{\mathbf{k}}$, corresponding to the wave \mathbf{k} of frequency ω_k belonging in a slowly-varying wavepacket, in a dispersive medium of real ϵ and of volume V , reads

$$U_{\mathbf{k}} = V \left[\frac{d(\omega\epsilon)}{d\omega} \bigg|_{\omega_k} |\mathbf{E}_{\mathbf{k}}^{(+)}|^2 + \frac{d(\omega\mu)}{d\omega} \bigg|_{\omega_k} |\mathbf{H}_{\mathbf{k}}^{(+)}|^2 \right], \quad (1.27)$$

where we gained a factor 4 by going from the complex electric fields to the analytic signals $\mathbf{E}^{(+,-)}$, as per the relation $\tilde{\mathbf{E}} = \mathbf{E}^{(+)} + \mathbf{E}^{(-)}$. For a non-magnetic material, we can use $H^2\mu_0 = E^2\epsilon = E^2\epsilon_0\epsilon_r$, to find

$$U_{\mathbf{k}} = V\epsilon_0 |\mathbf{E}_{\mathbf{k}}^{(+)}|^2 \frac{d(\omega^2\epsilon_r)}{\omega d\omega} \bigg|_{\omega_k}, \quad (1.28)$$

whereas for free-space the energy would read $U_{\mathbf{k}} = 2V\epsilon_0 |\mathbf{E}_{\mathbf{k}}^{(+)}|^2$. μ_0 is the permeability of the vacuum, ϵ_0 is the permittivity of the vacuum and ϵ_r the relative permittivity. In quantizing the field, we just consider this energy to be our Hamiltonian, with the electric field becoming quantum-mechanical operators according to

$$\begin{aligned} \mathbf{E}_{\mathbf{k}}^{(+)} &= i c_{\mathbf{k}} a_{\mathbf{k}} \\ \mathbf{E}_{\mathbf{k}}^{(-)} &= -i c_{\mathbf{k}} a_{\mathbf{k}}^\dagger \\ [\mathbf{E}_{\mathbf{k}}^{(+)}, \mathbf{E}_{\mathbf{k}}^{(-)}] &= c_{\mathbf{k}}^2. \end{aligned} \quad (1.29)$$

Finally, $c_{\mathbf{k}}$ is obtained from the normalization condition $U_{\mathbf{k}} = \hbar\omega_k a_{\mathbf{k}}^\dagger a_{\mathbf{k}}$, yielding

$$\begin{aligned} c_{\mathbf{k}}^2 &= \frac{\hbar\omega_k}{V\epsilon_0 \frac{d(\omega^2\epsilon_r)}{\omega d\omega} \bigg|_{\omega_k}} \\ &= \frac{\hbar\omega_k}{2\epsilon_0 V} \frac{u_{\mathbf{k}}}{c n_{\mathbf{k}}}, \end{aligned} \quad (1.30)$$

where we used the bosonic commutation relation. $u_{\mathbf{k}}$ is the group velocity, $n_{\mathbf{k}}$ is the refractive index and c is the speed of light in vacuum. In the last step we ignored the anisotropy in the (linear) crystal. The electric-field operator for a dispersive medium acquires an additional $\sqrt{u/cn}$ factor with respect to the free-field operator.

1.3.2 Solving the equation of motion

We start by rewriting the Hamiltonian that describes a three-wave interaction where the central frequencies that are involved, denoted with the ‘bar’, follow $\bar{\omega}_3 > \bar{\omega}_2 > \bar{\omega}_3/2 > \bar{\omega}_1$. This Hamiltonian writes

$$\hat{H} = \epsilon_0 \int d^3r \chi^{(2)} \hat{E}_1^{(-)}(\mathbf{r}, t) \hat{E}_2^{(-)}(\mathbf{r}, t) \hat{E}_3^{(+)}(\mathbf{r}, t) + \text{h.c.}, \quad (1.31)$$

where $\chi^{(2)}$ is the second order susceptibility of the nonlinear medium. We already used a form of the rotating-wave approximation in choosing the positive and negative frequency parts of the analytic signals. We also set the polarization of the fields corresponding to the non-vanishing elements of the $\chi^{(2)}$ tensor. The pump field is classical (we thus drop the hat), undepleted, monochromatic, and a planewave, described by a transverse amplitude A_p , such that

$$E_3^{(+)}(\mathbf{r}, t) = A_p \exp[i(k_p z - \omega_p t)], \quad (1.32)$$

where $k_p = \omega_p n_p / c$, with n_p the refractive index of a pump field propagating in the longitudinal (z) direction. The other fields are a collection of \mathbf{k} -modes, following

$$\begin{aligned} \hat{E}_j^{(+)} &= \sum_{\mathbf{k}_j} \hat{E}^{(+)}(\mathbf{k}_j, t) \exp[i(\mathbf{k}_j \cdot \mathbf{r})], \\ \hat{E}^{(+)}(\mathbf{k}_j, t) &= ic(\mathbf{k}_j) \hat{a}(\mathbf{k}_j, t) \exp[-i\omega(\mathbf{k}_j)t], \\ j &= \{1, 2\}, \end{aligned} \quad (1.33)$$

where $\hat{a}(\mathbf{k}_j, t)$ is the envelope of the annihilation operator in the mode \mathbf{k}_j . We turn to an integral by accounting for the quantization volume,

$$\begin{aligned} \sum_{\mathbf{k}} &\longrightarrow \frac{1}{v_k} \int d^3k, \\ v_k &= \frac{(2\pi)^3}{V}, \end{aligned} \quad (1.34)$$

where v_k is understood as the volume that each mode occupies in the k -space. We split up the longitudinal and transverse components of the wave vector \mathbf{k} as κ and \mathbf{q} , respectively. We can rewrite the Hamiltonian as

$$\begin{aligned} \hat{H} &= \frac{-\epsilon_0 A_p}{v_k^2} \int d^3r \chi^{(2)}(\mathbf{r}) \int d^3k'_1 d^3k'_2 c(\mathbf{k}'_1) c(\mathbf{k}'_2) \exp[i(k_p - \kappa'_1 - \kappa'_2)z] \\ &\times \exp[-i(\mathbf{q}'_1 + \mathbf{q}'_2) \cdot \boldsymbol{\rho}] \exp[-i(\omega_p - \omega(\mathbf{k}'_1) - \omega(\mathbf{k}'_2))t] \hat{a}^\dagger(\mathbf{k}'_1, t) \hat{a}^\dagger(\mathbf{k}'_2, t) + \text{h.c.}, \end{aligned} \quad (1.35)$$

that we can then integrate over the transverse spatial coordinates $\boldsymbol{\rho}$, using

$$\int d^2\rho e^{-i(\mathbf{q}_1+\mathbf{q}_2)\cdot\boldsymbol{\rho}} = 4\pi^2\delta(\mathbf{q}_1+\mathbf{q}_2), \quad (1.36)$$

and we integrate over \mathbf{q}'_2 to obtain

$$\begin{aligned} \hat{H} = & \frac{-\epsilon_0 A_p 4\pi^2}{v_k^{4/3}} \int_0^L dz \chi^{(2)}(z) \int d^3k'_1 d\kappa'_2 c(\mathbf{k}'_1) c(\mathbf{k}'_2) \exp[i(k_p - \kappa'_1 - \kappa'_2)z] \\ & \times \exp[-i(\omega_p - \omega(\mathbf{k}'_1) - \omega(\mathbf{k}'_2))t] \hat{a}^\dagger(\mathbf{k}'_1, t) \hat{a}^\dagger(\mathbf{k}'_2, t) + \text{h.c.}, \end{aligned} \quad (1.37)$$

where the $\mathbf{k}'_2 = \{-\mathbf{q}'_1, \kappa'_2\}$. We impose a nonlinear medium of length L . The polarization for the different fields is already set, assuming PDC with type-I phase matching. We added a factor of $v_k^{2/3}$, following the prescription of eq. (1.34).

The Heisenberg's equation of motion is

$$\begin{aligned} \frac{d}{dt} \hat{a}(\mathbf{k}_1, t) = & \frac{i}{\hbar} [\hat{H}, \hat{a}(\mathbf{k}_1, t)] \\ = & \frac{i\epsilon_0 A_p 4\pi^2 c(\mathbf{k}_1) \bar{c}(\mathbf{k}_2) \chi^{(2)}}{v_k^{1/3} \hbar} \int_0^L dz \int d\kappa'_2 \exp[i(k_p - \kappa_1 - \kappa'_2)z] \\ & \times \exp[-i(\omega_p - \omega(\mathbf{k}_1) - \omega(\mathbf{k}'_2))t] \hat{a}^\dagger(\mathbf{k}'_2, t) \end{aligned} \quad (1.38)$$

where $\bar{c}(\mathbf{k}_2)$ is $c(\mathbf{k}_2)$ evaluated at the central wavevector of the whole \mathbf{k}_2 range, determined mostly by the phase-matching function. We also assumed that $\chi^{(2)}$ is constant from $z = 0$ to L . Bringing $\bar{c}(\mathbf{k}_2)$ out of the integral is a form of the slowly-varying amplitude approximation, where the bandwidth of the \mathbf{k}_2 field has to be much smaller than the central value of \mathbf{k}_2 . We also used the commutation relation $[\hat{a}(\mathbf{k}_1, t), \hat{a}^\dagger(\mathbf{k}'_1, t)] = \delta(\mathbf{k}_1 - \mathbf{k}'_1)$. Upon integrating over \mathbf{k}'_1 , we got an additional factor v_k as a consequence of eq (1.34).

We integrate each side over a long interaction time, giving

$$\begin{aligned} \hat{a}(\mathbf{k}_1, t) - \hat{a}(\mathbf{k}_1, t_0) = & \frac{i\epsilon_0 A_p 4\pi^2 c(\mathbf{k}_1) \bar{c}(\mathbf{k}_2) \chi^{(2)}}{v_k^{1/3} \hbar} \int dt \int_0^L dz \int d\kappa'_2 \\ & \times \exp[i(k_p - \kappa_1 - \kappa'_2)z] \exp[-i(\omega_p - \omega(\mathbf{k}_1) - \omega(\mathbf{k}'_2))t] \hat{a}^\dagger(\mathbf{k}'_2, t), \end{aligned} \quad (1.39)$$

where t_0 denotes time at which the interaction starts. We now turn to the $(\mathbf{q}z\omega)$ reference, by using the Fourier transformed operators in the fixed reference frame, adopting the form

$$\hat{a}^\dagger(\mathbf{k}, t) = \hat{a}^\dagger(\mathbf{q}, \kappa, t) = \frac{1}{2\pi} \int d\omega dz \exp[-i(\omega(\mathbf{q}, \kappa) - \omega)t] \exp[i(\kappa - \kappa(\mathbf{q}, \omega))z] \hat{a}^\dagger(\mathbf{q}, z, \omega), \quad (1.40)$$

where κ is the quantity found in $\hat{a}^\dagger(\mathbf{q}, \kappa, t)$ and $\kappa(\mathbf{q}, \omega)$ depends on the dispersion, with ω as a variable. We plug the operator in the form of eq. (1.40) back into eq. (1.39), yielding

$$\begin{aligned} \hat{a}(\mathbf{k}_1, t) - \hat{a}(\mathbf{k}_1, t_0) = & \frac{i\epsilon_0 A_p 2\pi c(\mathbf{k}_1) \bar{c}(\mathbf{k}_2) \chi^{(2)}}{v_k^{1/3} \hbar} \int dt \int_0^L dz \int d\kappa'_2 \int d\omega \int dz' \\ & \times \exp[i(\kappa_p - \kappa_1 - \kappa'_2)z] \exp[-i(\omega_p - \omega_1 - \omega(\mathbf{q}'_2, \kappa'_2))t] \\ & \times \exp[-i(\omega(\mathbf{q}'_2, \kappa'_2) - \omega)t] \exp[i(\kappa'_2 - \kappa(\mathbf{q}'_2, \omega))z'] \hat{a}^\dagger(\mathbf{q}'_2, z', \omega), \end{aligned} \quad (1.41)$$

where $\omega_1 = \omega(\mathbf{k}_1)$. We may now proceed with the following integrations

$$\begin{aligned} \int dt \exp[-i(\omega_p - \omega_1 - \omega)t] &= 2\pi \delta(\omega_p - \omega_1 - \omega) \\ \int d\kappa'_2 \exp[-i(z - z')\kappa'_2] &= 2\pi v_k^{1/3} \delta(z - z'), \end{aligned} \quad (1.42)$$

where we added $v_k^{1/3}$ to account for the mode density. Replacing \mathbf{q}'_2 with $-\mathbf{q}_1$, as found after eq. (1.37), and integrating over the delta functions, we obtain

$$\begin{aligned} \hat{a}(\mathbf{k}_1, t) - \hat{a}(\mathbf{k}_1, t_0) &= \frac{(2\pi)^3 i\epsilon_0 A_p c(\mathbf{k}_1) \bar{c}(\mathbf{k}_2) \chi^{(2)}}{\hbar} \\ &\times \int_0^L dz \exp[i(\kappa_p - \kappa_1 - \kappa(-\mathbf{q}_1, \omega_p - \omega_1))z] \hat{a}^\dagger(-\mathbf{q}_1, \omega_p - \omega_1, z). \end{aligned} \quad (1.43)$$

Now we will examine the operators on the left-hand side of eq. (1.39). Outside the crystals, those operators do not depend on z , so may write them in terms of their Fourier counterparts, reading

$$\begin{aligned} \hat{a}^\dagger(\mathbf{q}, \kappa, t) &= \frac{1}{2\pi} \int d\omega \hat{a}^\dagger(\mathbf{q}, \omega, z) \int dz \exp[-i(\omega(\mathbf{q}, \kappa) - \omega)t] \exp[i(\kappa - \kappa(\mathbf{q}, \omega))z] \\ &= \int d\omega \hat{a}^\dagger(\mathbf{q}, \omega, z) \exp[-i(\omega(\mathbf{q}, \kappa) - \omega)t] \delta(\kappa - \kappa(\mathbf{q}, \omega)) \\ &= \int d\kappa u_\kappa \hat{a}^\dagger(\mathbf{q}, \omega, z) \exp[-i(\omega(\mathbf{q}, \kappa) - \omega)t] \delta(\kappa - \kappa(\mathbf{q}, \omega)) \\ &= u_\kappa \hat{a}^\dagger(\mathbf{q}, \omega, z), \end{aligned} \quad (1.44)$$

where we used $d\omega = u_\kappa d\kappa$, with u_κ the projection of the group velocity on the z -axis. This last relation can be used to relate the operator at t_0 to $z = 0$, and the operator at t to

$z = L$. We can finally write an equation of motion in the form

$$\begin{aligned} \hat{a}(\mathbf{q}_1, \omega_1, z = L) - \hat{a}(\mathbf{q}_1, \omega_1, z = 0) &= \frac{(2\pi)^3 i \epsilon_0 A_p c(\mathbf{k}_1) \bar{c}(\mathbf{k}_2) \chi^{(2)}}{\hbar u_\kappa} \\ &\times \int_0^L dz \exp[i(\kappa_p - \kappa_1 - \kappa(-\mathbf{q}_1, \omega_p - \omega_1))z] \hat{a}^\dagger(-\mathbf{q}_1, \omega_p - \omega_1, z), \end{aligned} \quad (1.45)$$

or, in the differential form,

$$\begin{aligned} \frac{d}{dz} \hat{a}(\mathbf{q}_1, \omega_1, z) &= \frac{(2\pi)^3 i \epsilon_0 A_p c(\mathbf{k}_1) \bar{c}(\mathbf{k}_2) \chi^{(2)}}{\hbar u_\kappa} \\ &\times \exp[i(\kappa_p - \kappa_1 - \kappa(-\mathbf{q}_1, \omega_p - \omega_1))z] \hat{a}^\dagger(-\mathbf{q}_1, \omega_p - \omega_1, z). \end{aligned} \quad (1.46)$$

Note that for each value of ω there are two possible values of κ . We thus implicitly assumed that waves propagate in the forward direction. We can rewrite the equation of motion in terms of z

$$\frac{da(\mathbf{q}, z, \omega)}{dz} \sim a^\dagger(\tilde{\mathbf{q}}, z, \tilde{\omega}) \exp[i(\kappa_p - \kappa(\mathbf{q}, \omega) - \kappa(\tilde{\mathbf{q}}, \tilde{\omega}))z] \frac{c\tilde{c}}{u_z \tilde{u}_z} \quad (1.47)$$

where we removed the s labels. We also introduced $\tilde{\mathbf{q}} = -\mathbf{q}$, $\tilde{\omega} = \omega_p - \omega$, $\tilde{c} = c(\tilde{\mathbf{q}}, \tilde{\omega})$ and $\tilde{u}_z = u_z(\tilde{\mathbf{q}}, \tilde{\omega})$. Introducing the short-hand notation $a_\omega(z) = a(\mathbf{q}, z, \omega)$, $a_{\tilde{\omega}}(z) = a(\tilde{\mathbf{q}}, z, \tilde{\omega})$ and $\Delta\kappa = \kappa_p - \kappa(\mathbf{q}, \omega) - \kappa(\tilde{\mathbf{q}}, \tilde{\omega})$, we get the two coupled differential equation

$$\begin{aligned} \frac{da_\omega}{dz} &\sim a_{\tilde{\omega}}^\dagger \exp[i\Delta\kappa z] \frac{c\tilde{c}}{u_z}, \\ \frac{da_{\tilde{\omega}}^\dagger}{dz} &\sim a_\omega \exp[-i\Delta\kappa z] \frac{c\tilde{c}}{\tilde{u}_z}, \end{aligned} \quad (1.48)$$

from which it is evident that the modes are coupled pairwise, even in the high-gain regime.

To solve this differential equation, we first move to the rotating frame, resulting in a coupling matrix that is independent of z . We find the following solution:

$$\begin{aligned} a_\omega(L) &= U a_\omega(0) + V a_{\tilde{\omega}}^\dagger(0) \\ U &= \left(\cosh[L\beta] - \frac{i\Delta\kappa}{2\beta} \sinh[L\beta] \right) \exp[i\Delta\kappa L/2] \\ V &= \frac{\Gamma \sqrt{\tilde{u}_z/u_z}}{\beta} \sinh[L\beta] \exp[i\Delta\kappa L/2] \\ \Gamma^2 &\propto \frac{(c\tilde{c})^2}{u_z \tilde{u}_z} \\ \beta^2 &= \Gamma^2 - \frac{\Delta\kappa^2}{4}. \end{aligned} \quad (1.49)$$

This equation is a generalization of the Bogolyubov transformation for phase-matched squeezed state, see eq. (1.8). The photon operator in the planewave representation after the interaction $a_{\mathbf{k}} = a(\mathbf{q}_s, \kappa_s, t \rightarrow \infty)$, obtained from the input operators, like $a_{\mathbf{k},0} = a(\mathbf{q}_s, \kappa_s, t \rightarrow -\infty)$, takes the form

$$\begin{aligned} a_{\mathbf{k}} &= u_z a_\omega(L) = u_z U a_\omega(0) + u_z V a_{\tilde{\omega}}^\dagger(0) \\ &= U a_{\mathbf{k},0} + \frac{u_z}{\tilde{u}_z} V a_{\tilde{\mathbf{k}},0}^\dagger, \end{aligned} \quad (1.50)$$

from which we can compute the number of photons in the k -representation, from modes \mathbf{k} and \mathbf{k}' , with the vacuum at the input, reading

$$N_{\mathbf{k}\mathbf{k}'} = \langle a_{\mathbf{k}}^\dagger a_{\mathbf{k}'} \rangle = |V|^2 \left(\frac{u_z}{\tilde{u}_z} \right)^2 \delta(\tilde{\mathbf{k}} - \tilde{\mathbf{k}}') = \frac{\Gamma^2}{\beta^2} \sinh^2[L\beta], \quad (1.51)$$

where we used

$$\delta(\tilde{\mathbf{k}} - \tilde{\mathbf{k}}') = \frac{\delta(\mathbf{k} - \mathbf{k}')}{|d\tilde{\mathbf{k}}/d\mathbf{k}|} = \delta(\mathbf{k} - \mathbf{k}') \frac{d\mathbf{k}/d\omega}{d\tilde{\mathbf{k}}/d\omega} = \delta(\mathbf{k} - \mathbf{k}') \frac{\tilde{u}_z}{u_z}. \quad (1.52)$$

Importantly, when the phase-matching condition is fulfilled, the number of photons in mode \mathbf{k} is given by

$$N_{\mathbf{k}} = \sinh^2[L\Gamma], \quad (1.53)$$

where the phase-matched gain reads

$$\Gamma \sim \frac{c\tilde{c}}{\sqrt{\tilde{u}_z u_z}} \approx \frac{\omega\tilde{\omega}}{n\tilde{n}}, \quad (1.54)$$

where the approximation is that we cancelled the group velocities with each other. This is the result that we used to perform the calibration experiment, see chapter 6.

Chapter 2

Engineering the Frequency Spectrum of Bright Squeezed Vacuum via Group Velocity Dispersion in an SU(1,1) Interferometer

This work is an extension of a similar experiment performed in the spatial domain [38]. A first step had been achieved when we observed the effect of dispersion on the interference pattern in a nonlinear interferometer in the Mach-Zehnder configuration, in an experiment performed and analyzed by Dr. Timur Iskhakov and me [45]. I then moved to a Michelson-type interferometer—which allowed us to use only one nonlinear crystal—and increased the amount of dispersion in order to reduce the number of frequency modes as close as possible to unity.

The theory used to perform the simulations shown in Fig. (4) and Fig. (5) is better developed in chapter 3. The main source of error in this experiment was the phase instability of the interferometer. During the course of one acquisition, the shape of the spectrum could change drastically, going from constructive to destructive interference. This is manifest in Fig. (4), where in the 8th data point, the larger error in the FWHM leads to a reduction in the value of $g^{(2)}$. In other words, for this data point, many spectra were acquired while the interferometer was not stabilized on constructive interference. When the interference is not perfectly constructive, more modes are being excited, leading to a deterioration of the $g^{(2)}$ value.

This experiment was proposed by Prof. Maria Chekhova and fleshed out with the help

of Profs. Robert Boyd and Gerd Leuchs. During my visit in Erlangen, I built the setup and acquired most of the data. Dr. Mathieu Manceau wrote the LabVIEW code for data acquisition and acquired the last few data points. I analyzed the data and wrote the code to compute the joint spectral amplitude and the Schmidt-mode decomposition, based on the theory provided by Polina Sharapova and Olga Tikhonova. I wrote most of the letter. I wrote the supplementary materials, using the data provided by Dr. Mathieu Manceau. All coauthors offered invaluable help throughout writing the article.

Engineering the Frequency Spectrum of Bright Squeezed Vacuum via Group Velocity Dispersion in an SU(1,1) Interferometer

Samuel Lemieux,^{1,*} Mathieu Manceau,² Polina R. Sharapova,^{3,4} Olga V. Tikhonova,^{4,5}

Robert W. Boyd,^{1,6} Gerd Leuchs,^{2,7} and Maria V. Chekhova^{2,4,7}

¹*Department of Physics and Max Planck Centre for Extreme and Quantum Photonics, University of Ottawa, 25 Templeton Street, Ottawa, Ontario K1N 6N5, Canada*

²*Max Planck Institute for the Science of Light, G.-Scharowsky Strasse 1/Bau 24, 91058 Erlangen, Germany*

³*Department of Physics, University of Paderborn, Warburger Strasse 100, D-33098 Paderborn, Germany*

⁴*Physics Department, Lomonosov Moscow State University, Moscow 119991, Russia*

⁵*Skobeltsyn Institute of Nuclear Physics, Lomonosov Moscow State University, Moscow 119234, Russia*

⁶*Institute of Optics, University of Rochester, Rochester, New York 14627, USA*

⁷*University of Erlangen-Nuremberg, Staudtstrasse 7/B2, 91058 Erlangen, Germany*

(Received 5 July 2016; published 27 October 2016)

Bright squeezed vacuum, a promising tool for quantum information, can be generated by high-gain parametric down-conversion. However, its frequency and angular spectra are typically quite broad, which is undesirable for applications requiring single-mode radiation. We tailor the frequency spectrum of high-gain parametric down-conversion using an SU(1,1) interferometer consisting of two nonlinear crystals with a dispersive medium separating them. The dispersive medium allows us to select a narrow band of the frequency spectrum to be exponentially amplified by high-gain parametric amplification. The frequency spectrum is thereby narrowed from (56.5 ± 0.1) to (1.22 ± 0.02) THz and, in doing so, the number of frequency modes is reduced from approximately 50 to 1.82 ± 0.02 . Moreover, this method provides control and flexibility over the spectrum of the generated light through the timing of the pump.

DOI: 10.1103/PhysRevLett.117.183601

Photon pairs have become a ubiquitous tool for many quantum optics applications. They have been used extensively to herald single photons, to increase the phase sensitivity of interferometers, and to test the foundations of quantum mechanics through Bell's inequalities [1,2]. A versatile source of biphotons is parametric down-conversion (PDC), a process in which a pump photon is split in a nonlinear crystal into a pair of entangled photons labeled the signal and the idler. Recent work has featured PDC in the high-gain regime, leading to the generation of bright squeezed vacuum (BSV), that is, squeezed vacuum with a large mean photon number per mode [3]. This type of radiation manifests macroscopic quantum features, such as polarization entanglement within a macroscopic pulse [4], Hong-Ou-Mandel bunching [5], as well as subshot-noise photon-number correlations [6–12]. With the detection losses sufficiently small, this state of light will even violate Bell's inequalities [13].

The angular and frequency spectra of PDC are, in the general case, multimode, with the width inversely proportional to the length of the crystal due to phase matching. At the same time, there are various potential applications that require single-mode BSV, such as phase supersensitivity in SU(1,1) interferometers [2,14–16] or heralded preparation of nonclassical states [17]. In this Letter, we propose and demonstrate a method to dramatically narrow the frequency spectrum and reduce the number of temporal modes of

BSV states. It constitutes a possible extension of the quasingle transverse mode source of BSV [18], paving the way for truly single-mode BSV. Unlike most PDC frequency engineering methods proposed to date [17,19], our source makes use of the high gain (because the desired modes are amplified exponentially), does not require phase-matching engineering, and could be extended to all the transparency range of the nonlinear crystal [20]. Importantly, the method does not involve losses and thus does not destroy photon-number correlations [18].

The source is based on the interference between the PDC generated by two separated crystals. This scheme, aimed at increasing the parametric gain while at the same time reducing the transverse walk-off [3,21], relies on the properties of the SU(1,1) interferometer [2]. The latter, in contrast to a usual SU(2) interferometer, has beam splitters replaced by nonlinear media where parametric amplification takes place. In our setup, this leads to the strong selective amplification of some modes and to the deamplification of others.

By introducing a medium with group velocity dispersion (GVD) between the two crystals forming the SU(1,1) interferometer, we are able to tailor the frequency spectral width of PDC generated in the high-gain regime (Fig. 1). A pump pulse sent into the first crystal with quadratic nonlinearity ($\chi^{(2)}$) generates a broadband PDC pulse. The latter is injected into the GVD medium and undergoes

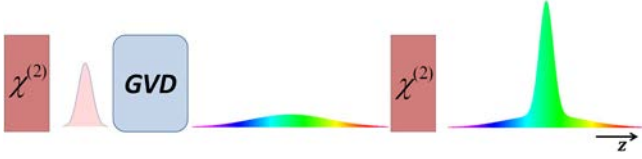


FIG. 1. Principle of the method. A broadband PDC pulse is generated in a strongly pumped nonlinear crystal; the PDC pulse spreads and chirps after propagation in a medium with group velocity dispersion (GVD); the spread and chirped PDC pulse is amplified in another crystal, using the same pump pulse. The frequency spectrum after the second crystal is narrower than that after the first one.

temporal spreading and chirping, meaning that time and frequency contents become correlated. In the second crystal, only the part of the stretched PDC pulse that overlaps in time with the unaltered pump pulse is amplified. This procedure is equivalent to selecting a narrow frequency width without introducing noticeable losses.

The parametric gain G is a key quantity in describing this approach. The average number of output photons per mode $\langle N \rangle$ is given by $\sinh^2(G)$, and $G \propto \chi^{(2)} E_p L$, where E_p is the pump's electric field amplitude and L is the length of the interaction with the pump pulse, which is given by the crystal length if walk-off effects are negligible. In the high-gain regime—large $\chi^{(2)} E_p L$ product—doubling the interaction length between the pump pulse and the PDC pulse increases the number of PDC photons by several orders of magnitude. In our case, the interaction length is doubled only for the part of the stretched PDC pulse that overlaps with the unaltered pump pulse in the second crystal, leading to a narrow band output pulse.

Since the PDC pulse is chirped and stretched in time, varying the time of arrival of the pump pulse tunes the central frequency of the amplified PDC. This tuning is performed simply by changing the length of the pump path. In addition, one would expect a twin beam to be created at a frequency determined by the conservation of the pump photon energy. In the spectrum, two peaks would thus appear on either side of the degenerate frequency, and at equal distance therefrom.

To theoretically describe the interferometer, we assume an undepleted classical pump pulse of fixed duration consisting of plane waves with a Gaussian frequency spectrum of width $\Delta\omega_p$ and central frequency $\bar{\omega}_p$. Moving to the frequency domain and assuming that each photon from the pump pulse spectrum (p) gives rise to one signal (s) and one idler (i) photon, fulfilling $\omega_p = \omega_s + \omega_i$, we obtain a time-independent Hamiltonian. The calculations based on neglecting frequency mismatches are in good agreement with the measurements obtained for the two-crystal interferometer with dispersion [22], whereas for a single crystal the frequency mismatches have to be taken into account [23,24].

Under these assumptions the Hamiltonian becomes

$$H = i\hbar\Gamma \int d\omega_s d\omega_i F(\omega_s, \omega_i) a_{\omega_s}^\dagger a_{\omega_i}^\dagger + \text{H.c.}, \quad (1)$$

where Γ is a measure of the strength of the parametric interaction and $F(\omega_s, \omega_i)$ is called the joint spectral amplitude (JSA). Following Ref. [25], we find the JSA as

$$F(\omega_s, \omega_i) = \frac{\sin(\delta/2)}{\delta/2} \exp\left[\frac{-(\omega_s + \omega_i - \bar{\omega}_p)^2}{4\Delta\omega_p^2}\right] \times \exp[-i(\delta + \delta'/2)] \cos[(\delta + \delta')/2], \quad (2)$$

for the case of two crystals separated by a linear optical material, where $\delta = [k_p - k_s(\omega_s) - k_i(\omega_i)]L$ is the phase mismatch accumulated in one of the crystals of length L and, likewise, δ' is the phase mismatch accumulated in the linear gap between the two crystals. The first two factors correspond to the JSA of a single crystal pumped with a pulse of finite duration, assuming conservation of the pump photon's energy. The last two factors convey the total phase acquired by the pump and the PDC in the interferometer, and are responsible for the interference effects appearing in the frequency spectrum. δ' embodies all the effects of the linear gap between the two crystals, including propagation in different paths, pulse spreading, and chirping.

To solve the Heisenberg equation of motion for $a_{\omega_s}^\dagger$ and $a_{\omega_i}^\dagger$, we numerically diagonalize the Hamiltonian by performing a Schmidt decomposition of the JSA [Eq. (2)] so that it adopts the form

$$F(\omega_s, \omega_i) = \sum_k \sqrt{\tilde{\lambda}_k} u_k(\omega_s) v_k(\omega_i), \quad (3)$$

in analogy to Refs. [26–28]. In the high-gain solution, the weights λ_k of the Schmidt (broadband) modes $u_k(\omega_s)$ and $v_k(\omega_i)$ become [26]

$$\tilde{\lambda}_k = \frac{\sinh^2(G\sqrt{\lambda_k})}{\sum_{k=1}^{\infty} \sinh^2(G\sqrt{\lambda_k})}, \quad (4)$$

where the parametric gain G is proportional to the coupling strength Γ . The frequency spectrum of the signal (idler) beam is then found by summing the Schmidt-mode intensity distributions $|u_k(\omega_s)|^2$ ($|v_k(\omega_i)|^2$) with their weights $\tilde{\lambda}_k$. This method provides a complete description of the high-gain PDC spectrum, including the effective number of modes, estimated from the new weights given by Eq. (4).

In the experiment, the effective number of Schmidt modes K is assessed from the degree of second-order coherence with zero delay τ ,

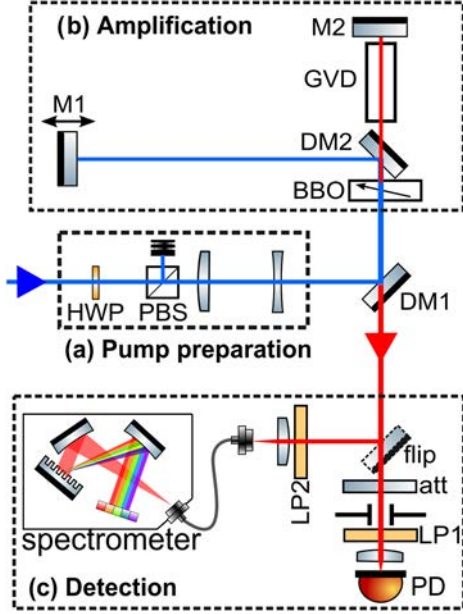


FIG. 2. Experimental setup. (a) An attenuator [half-wave plate (HWP) and Glan polarizer (PBS)] and a telescope are used to prepare the pump in power, polarization, and beam diameter. (b) PDC generated in the first pass of the pump in the BBO crystal is stretched temporally in a dispersive medium (GVD) and sent back into the crystal to be amplified. The time of arrival of the pump is carefully tuned with the position of mirror M1, set on a translation stage. (c) The PDC is sent either into a spectrometer or into a photodiode (PD).

$$g^{(2)}(\tau = 0) = 1 + \frac{g_1^{(2)} - 1}{K}, \quad (5)$$

where $g_1^{(2)}$ is the degree of second-order coherence of single-mode PDC [29]. For degenerate collinear PDC, $g_1^{(2)} = 3$ [30]. $g^{(2)}$ is obtained experimentally from the definition $g^{(2)}(\tau = 0) = \langle N^2 \rangle / \langle N \rangle^2$, where N is the number of photons in the PDC field [31].

The experimental setup (Fig. 2) consists of an SU(1,1) interferometer of Michelson type [32]. The pump ($\lambda_p = 400$ nm) is the second harmonic of a Spectra Physics Spitfire Ace system with a 5 kHz repetition rate and 0.9 ps pulses, its power is measured right after an attenuator [half-wave plate (HWP) and a Glan polarizer (PBS)], and its diameter is set to 0.6 mm FWHM with a telescope ($f = 300$ mm and $f = -75$ mm). A dichroic mirror (DM1, Newlight Photonics HS10-R400/T800) sends the pump towards a nonlinear crystal (BBO, type-I degenerate collinear phase matching, 3 mm long). Another dichroic mirror (DM2, same as DM1) reflects the pump and transmits the PDC. The pump is reflected by a mirror (M1) set on a translation stage to tune its time of arrival, while the PDC is sent into a dispersive medium (GVD) and reflected back again by a mirror (M2). The PDC and the pump are recombined at DM2. The PDC is

amplified in the crystal in accordance with the time of arrival of the pump. After its transmission by DM1, the PDC can either be sent into a low-noise charge integrating detector based on a *p-i-n* diode (PD) or reflected into the spectrometer by means of a flip mirror (flip). In the detector arm, there is a variable attenuator (att) to prevent saturation, a 500 μ m pinhole to select a single angular mode, a long-pass filter (LP1) for suppressing the residual pump radiation, and a focusing lens ($f = 40$ mm). The *p-i-n* diode is used to measure the PDC intensity and $g^{(2)}$. The spectrometer arm consists of a long-pass filter (LP2) and a focusing lens ($f = 100$ mm) to couple light into the spectrometer (Ocean Optics HR4000).

The dispersive material contains various combinations of SF6, SF57, LLF1, and BK7 glass rods [33]. The amount of pulse spreading is given by the GVD parameter $k''d$ (dimensionality ps^2), where d is the thickness of the material, and $k'' = d^2k/d\omega^2|_{\omega_0}$ is the GVD evaluated at the central frequency ω_0 . For each new rod or combination of rods, one has to set the new position of mirror M1 to provide the proper path length for the pump pulse. The phase shift in the interferometer is not locked and, therefore, drifts randomly, with a typical time of 1 min. For each set of rods, the pump power is adjusted so that the amplified PDC has the same intensity. This ensures that the parametric gain is kept roughly equal for each measurement. The spectra are recorded only when the interferometer is producing stable output fringes, and the FWHM of the spectra is measured for each value of $k''d$. The theoretical and experimental spectral widths reported herein correspond to the FWHM of spectra in the photon numbers [34]. The number of acquired pulses in $g^{(2)}$ measurements is limited by the drifting time of the interferometer.

The introduction of a dispersive material between two nonlinear crystals has the effect of dramatically narrowing the frequency spectrum of PDC, as compared with the

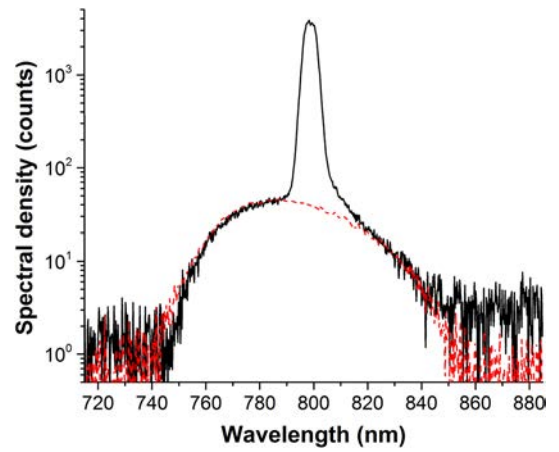


FIG. 3. Comparison of the spectral densities obtained experimentally for a single pass through the nonlinear crystal (dashed red line), and for the interferometer with a 18.3 cm rod of SF6 (solid black line).

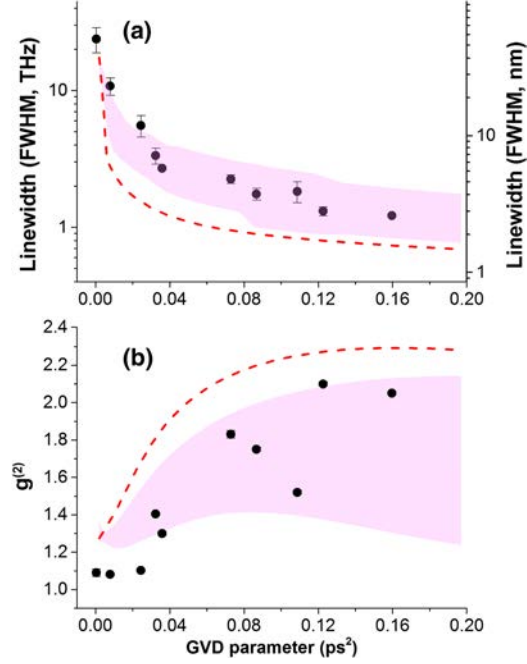


FIG. 4. Linewidth of the spectrum (a) and $g^{(2)}$ (b) as functions of the GVD parameter. Experimental points (black) are compared to theoretically calculated values (pink zones and red dashed curves). The red dashed curves correspond to constructive interference between the pump and the PDC at degeneracy. The pink zones denote the region within 1 standard deviation from the mean, which is determined by averaging over 8 different phases for the central frequency from 0 to 2π by varying the air gaps, considering amplification and deamplification cases. The influence of GVD manifests itself through the narrowing of the spectrum and the increase in $g^{(2)}$.

spectrum produced by a single crystal (Fig. 3). Moreover, the frequency spectrum of amplified PDC gets narrower as the value of $k''d$ between the two crystals is increased (Fig. 4). The observed asymptotic trend culminates with an experimental spectral width of (1.22 ± 0.02) THz, corresponding to the sample with the greatest GVD parameter. The experimental results fit well between the boundaries obtained from theory for different phase scenarios. The effective number of modes K , assessed through $g^{(2)}$, is reduced as well when $k''d$ is increased, shrinking down to a minimum of 1.82 ± 0.02 . One would have expected that the points in the right-hand part of Fig. 4, near the asymptote, exhibit single-mode statistics, but the contribution of the phase fluctuations in the interferometer is significant and results in an increase of the number of modes. In fact, phase drifts can transform the single peak of Fig. 3 into two or three peaks, effectively changing the frequencies where amplification or deamplification occurs. For smaller GVD values, the spectrum exhibits a rich interference pattern [34,35]. The theoretical prediction for a best-case scenario—phase locked on constructive interference, the dashed curve in Fig. 4—yields a maximum $g^{(2)}$ of

2.29 ($K = 1.55$ modes) with a parametric gain of 7. Under this theory, increasing the gain has the effect of improving the efficiency of the mode selection: the minimum number of modes shrinks to 1.06 when the parametric gain is 10.

Background multimode PDC, which is not amplified in the second crystal, also has a considerable effect on $g^{(2)}$. As a simple test, we put an interference filter ($\Delta\lambda = 10$ nm) in front of the detector to cut out part of the background PDC, and $g^{(2)}$ went from 2.05 ± 0.01 to 2.29 ± 0.02 , corresponding to $K = 1.5$.

Displacing mirror M1, thereby varying the time of arrival of the pump pulse with respect to the PDC pulse, has the effect of generating two peaks on either side of the degenerate frequency (Fig. 5). A greater mismatch in arrival time induces stronger detuning from degeneracy and weaker PDC intensity, until the two peaks completely fade out. The theory curve of Fig. 5 was convolved with a Gaussian whose width corresponds to the nominal resolution of the spectrometer. Without the convolution, one of the two peaks exhibits densely packed fringes (see the inset in Fig. 5): this interference effect can be understood as induced coherence arising from the indistinguishability of the photon sources [22,36].

In conclusion, by inserting a dispersive medium between two strongly pumped PDC emitters, we have demonstrated BSV with narrowed spectral width, from (56.5 ± 0.1) THz down to (1.22 ± 0.02) THz. Meanwhile, the number of modes decreased from approximately 50 down to 1.82 ± 0.02 , and even 1.5 when the background radiation from a single PDC emitter was eliminated. The method can be used to generate and tune bright narrow band two-color PDC by changing the time of arrival of the pump pulse with respect to the PDC pulse.

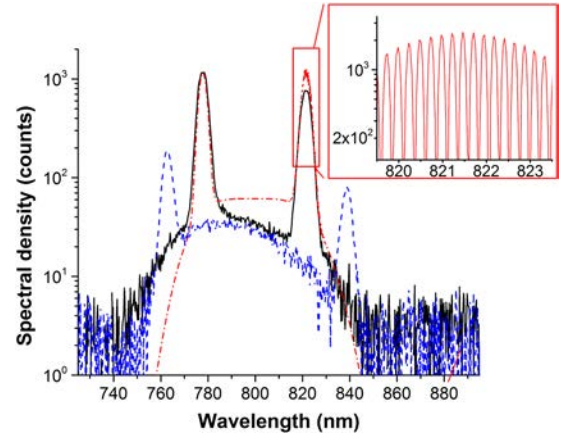


FIG. 5. Experimental spectra when the pump path length is increased by (1.40 ± 0.01) mm (black solid line) and by (2.40 ± 0.01) mm (blue dashed line) with respect to the configuration for degeneracy. The red dash-dotted line shows the spectrum calculated for the first case, with a parametric gain of 7. The inset shows the second peak of the calculated spectrum without the convolution to show the interference fringes.

It was earlier demonstrated that by using two spatially separated crystals, one can filter out a single angular mode of PDC [18]. A combination of this method with our approach can be used to generate single-mode BSV in both the frequencies and the angles [37], but has yet to be demonstrated experimentally. In our case, the pump beam waist was too small to provide the selection of a single spatial mode.

Our method of selective amplification in an SU(1,1) interferometer can be further developed by replacing the GVD material by a pulse shaper imprinting different phases on the modes to be amplified or deamplified. In this manner, one can arbitrarily change the shape of the frequency spectrum amplified in the second crystal. Our source is a significant improvement in the generation of single-mode bright squeezed vacuum states of light.

The research leading to these results has received funding from the EU FP7 under Grant Agreement No. 308803 (Project BRISQ2). We also acknowledge partial financial support of the Russian Foundation for Basic Research, Grant No. 14-02-00389-a and the joint DFG-RFBR project CH 1591/2-1-16-52-12031 NNIO_a. This work was also supported by the Canada Excellence Research Chairs program and the National Science and Engineering Research Council of Canada. G.L. acknowledges financial support from the European Research Council via the Advanced Grant “PACART”. We thank Xin Jiang and Patricia Schrehardt for providing the glass samples of SF6, SF57, and LLF1.

-
- [1] C. M. Caves, *Phys. Rev. D* **23**, 1693 (1981).
- [2] B. Yurke, S. L. McCall, and J. R. Klauder, *Phys. Rev. A* **33**, 4033 (1986).
- [3] M. V. Chekhova, G. Leuchs, and M. Żukowski, *Opt. Commun.* **337**, 27 (2015).
- [4] T. Sh. Iskhakov, I. N. Agafonov, M. V. Chekhova, and G. Leuchs, *Phys. Rev. Lett.* **109**, 150502 (2012).
- [5] T. Sh. Iskhakov, K. Yu. Spasibko, M. V. Chekhova, and G. Leuchs, *New J. Phys.* **15**, 093036 (2013).
- [6] O. Jedrkiewicz, Y.-K. Jiang, E. Brambilla, A. Gatti, M. Bache, L. A. Lugiato, and P. Di Trapani, *Phys. Rev. Lett.* **93**, 243601 (2004).
- [7] M. Bondani, A. Allevi, G. Zambra, M. G. A. Paris, and A. Andreoni, *Phys. Rev. A* **76**, 013833 (2007).
- [8] G. Brida, L. Caspani, A. Gatti, M. Genovese, A. Meda, and I. R. Berchera, *Phys. Rev. Lett.* **102**, 213602 (2009).
- [9] I. N. Agafonov, M. V. Chekhova, and G. Leuchs, *Phys. Rev. A* **82**, 011801 (2010).
- [10] V. Boyer, A. M. Marino, R. C. Pooser, and P. D. Lett, *Science* **321**, 544 (2008).
- [11] A. M. Marino, V. Boyer, R. C. Pooser, P. D. Lett, K. Lemons, and K. M. Jones, *Phys. Rev. Lett.* **101**, 093602 (2008).
- [12] V. Boyer, A. M. Marino, and P. D. Lett, *Phys. Rev. Lett.* **100**, 143601 (2008).
- [13] K. Rosolek, M. Stobińska, M. Wieśniak, and M. Żukowski, *Phys. Rev. Lett.* **114**, 100402 (2015).
- [14] F. Hudelist, J. Kong, C. Liu, J. Jing, Z. Y. Ou, and W. Zhang, *Nat. Commun.* **5**, 3049 (2014).
- [15] Z. Y. Ou, *Phys. Rev. A* **85**, 023815 (2012).
- [16] W. N. Plick, J. P. Dowling, and G. S. Agarwal, *New J. Phys.* **12**, 083014 (2010).
- [17] G. Harder, T. J. Bartley, A. E. Lita, S. W. Nam, T. Gerrits, and C. Silberhorn, *Phys. Rev. Lett.* **116**, 143601 (2016).
- [18] A. M. Pérez, T. Sh. Iskhakov, P. Sharapova, S. Lemieux, O. V. Tikhonova, M. V. Chekhova, and G. Leuchs, *Opt. Lett.* **39**, 2403 (2014).
- [19] P. J. Mosley, J. S. Lundeen, B. J. Smith, P. Wasylczyk, A. B. U'Ren, C. Silberhorn, and I. A. Walmsley, *Phys. Rev. Lett.* **100**, 133601 (2008).
- [20] F. O. Koller, K. Haider, M. Huber, T. E. Schrader, N. Regner, W. J. Schreier, and W. Zinth, *Opt. Lett.* **32**, 3339 (2007).
- [21] D. J. Armstrong, W. J. Alford, T. D. Raymond, A. V. Smith, and M. S. Bowers, *J. Opt. Soc. Am. B* **14**, 460 (1997).
- [22] A detailed theoretical comparison of the single- and two-crystal configurations in the high-gain regime will be presented in P. Sharapova, O. V. Tikhonova, S. Lemieux, R. W. Boyd, G. Leuchs, and M. V. Chekhova (to be published).
- [23] N. Quesada and J. E. Sipe, *Phys. Rev. A* **90**, 063840 (2014).
- [24] A. Christ, B. Brecht, W. Mauerer, and C. Silberhorn, *New J. Phys.* **15**, 053038 (2013).
- [25] D. N. Klyshko, *Zh. Eksp. Teor. Fiz.* **104**, 2676 (1993) [*Sov. Phys. JETP* **77**, 222 (1993)].
- [26] P. Sharapova, A. M. Pérez, O. V. Tikhonova, and M. V. Chekhova, *Phys. Rev. A* **91**, 043816 (2015).
- [27] W. Wasilewski, A. I. Lvovsky, K. Banaszek, and C. Radzewicz, *Phys. Rev. A* **73**, 063819 (2006).
- [28] A. Christ, K. Laiho, A. Eckstein, K. N. Cassemiro, and C. Silberhorn, *New J. Phys.* **13**, 033027 (2011).
- [29] M. A. Finger, T. Sh. Iskhakov, N. Y. Joly, M. V. Chekhova, and P. St. J. Russell, *Phys. Rev. Lett.* **115**, 143602 (2015).
- [30] R. Loudon and P. L. Knight, *J. Mod. Opt.* **34**, 709 (1987).
- [31] By definition, the photon creation and annihilation operators in $g^{(2)}$ should follow normal ordering. When the number of photons is high, it is possible to drop normal ordering.
- [32] I. Abram, R. K. Raj, J. L. Oudar, and G. Dolique, *Phys. Rev. Lett.* **57**, 2516 (1986).
- [33] SCHOTT optical glass data sheets, 2012, http://refractiveindex.info/download/data/2012/schott_optical_glass_collection_datasheets_dec_2012_us.pdf.
- [34] See Supplemental Material at <http://link.aps.org/supplemental/10.1103/PhysRevLett.117.183601> for details on the calibration of the spectrometer and on the effect of phase fluctuations on the shape of the frequency spectrum.
- [35] T. Sh. Iskhakov, S. Lemieux, A. M. Pérez, R. W. Boyd, M. V. Chekhova, and G. Leuchs, *J. Mod. Opt.* **63**, 64 (2016).
- [36] X. Y. Zou, L. J. Wang, and L. Mandel, *Phys. Rev. Lett.* **67**, 318 (1991).
- [37] Note that by selecting a single spatial mode, one does not yet select a single frequency mode, and vice versa.

Engineering the frequency spectrum of bright squeezed vacuum via group velocity dispersion in an SU(1,1) interferometer - Supplementary Material

Samuel Lemieux,^{1,*} Mathieu Manceau,² Polina R. Sharapova,^{3,4} Olga V. Tikhonova,^{4,5}
Robert W. Boyd,^{1,6} Gerd Leuchs,^{2,7} and Maria V. Chekhova^{2,4,7}

¹*Department of Physics and Max Planck Centre for Extreme and Quantum Photonics,
University of Ottawa, 25 Templeton Street, Ottawa, Ontario K1N 6N5, Canada*

²*Max Planck Institute for the Science of Light, G.-Scharowsky Str.1/Bau 24, 91058 Erlangen, Germany*

³*Department of Physics, University of Paderborn,
Warburger Strasse 100, D-33098, Paderborn, Germany*

⁴*Physics Department, Lomonosov Moscow State University, Moscow 119991, Russia*

⁵*Skobeltsyn Institute of Nuclear Physics, Lomonosov Moscow State University, Moscow 119234, Russia*

⁶*Institute of Optics, University of Rochester, Rochester, New York 14627, USA*

⁷*University of Erlangen-Nuremberg, Staudtstrasse 7/B2, 91058 Erlangen, Germany*

(Dated: September 15, 2016)

In section 1, the sensitivity of a small solid-angle spectrometer is calibrated using the properties of twin-beams generated via parametric down-conversion. In section 2, we examine the interference fringes in the frequency spectrum obtained at the output of an SU(1,1) interferometer.

I. CALIBRATION OF A SPECTROMETER WITH TWIN BEAM

Parametric down-conversion (PDC) can be used to calibrate the sensitivity of a spectrometer. The maxima of the twin-peaks in two-color PDC are almost constant over a broad frequency range around degeneracy. This knowledge about the photon-number frequency spectrum allows one to estimate the response function of the spectrometer. In the following, we mathematically describe the photon-number frequency spectrum of PDC, and report an experimental demonstration of the calibration method based on its properties.

In the low-gain regime, the number of photons of frequency ω_s in the planewave mode k_s is given by

$$N(\omega_s, \omega_i) = \left(\frac{2\pi\chi^{(2)}|E_p|L}{c} \alpha(k_s, k_i) \right)^2 \omega_s \omega_i, \quad (\text{S1a})$$

$$\alpha(k_s, k_i) = \frac{\sin([k_p - k_s - k_i]L/2)}{[k_p - k_s - k_i]L/2} \quad (\text{S1b})$$

where p , s and i are the pump, the signal and the idler, $\chi^{(2)}$ is the effective quadratic susceptibility of a nonlinear crystal of length L , $|E_p|$ is the pump electric field amplitude, c is the speed of light in the vacuum, and $\alpha(k_s, k_i)$ is the phase-matching function [1]. Here, the pump is assumed to be a monochromatic plane wave. Assuming collinear propagation, we can rewrite the wavevectors in terms of frequencies, using $k = \omega/c$. Also, restricting the analysis to three photon events yields a photon energy relation of the form $\omega_p = \omega_s + \omega_i$. The number of photons now reads

$$N(\omega_s) = \left(\frac{2\pi\chi^{(2)}|E_p|}{c} \alpha(\omega_s, \omega_p - \omega_s) \right)^2 \omega_s (\omega_p - \omega_s). \quad (\text{S2})$$

The case when $\alpha(\omega_s, \omega_p - \omega_s) = 1$ is achieved provided that the phase-matching condition is fulfilled, $k_p - k_s - k_i = 0$. In this case, the dependence of the number of photons per mode on the frequency becomes

$$N(\Omega) \propto \left(\frac{\omega_p}{2} \right)^2 - \Omega^2, \quad \Omega = \omega_s - \omega_p/2, \quad (\text{S3})$$

where we defined Ω as the frequency detuning of ω_s with respect to the frequency of degeneracy $\omega_p/2$. Around degeneracy, the number of photons almost does not depend on Ω . This property can be used to calibrate the sensitivity

* XXXXXXXXXX

of a small solid-angle spectrometer in the photon number spectral density, and is valid as long as $\Omega \ll \omega_p/2$. As an example, for $\lambda_p = 400$ nm and $\lambda_s = 700$ nm, we have $\Omega^2/[\omega_p/2]^2 \approx 0.02$. The phase-matching condition is fulfilled by tuning the angle of the optic axis of the nonlinear crystal with respect to the pump's direction of propagation.

A series of PDC spectra for different optic axis angles was acquired with a spectrometer whose sensitivity is not calibrated (Fig. S1). A polynomial curve fit connecting the peaks of the different twin-beams was generated. We then divided an uncalibrated spectrum corresponding to degenerate phase-matching for a single crystal by this fit-function (Fig. S2). The result is a calibrated spectrum that appears symmetric around the degenerate frequency, and that exhibits a flat top. The flat top is a typical spectral shape due to the phase-matching function $\alpha(\omega_s, \omega_i)$. As a reference, a curve fit with a sinc^2 shape, as in eqs. (S1), was added to Fig. S2.

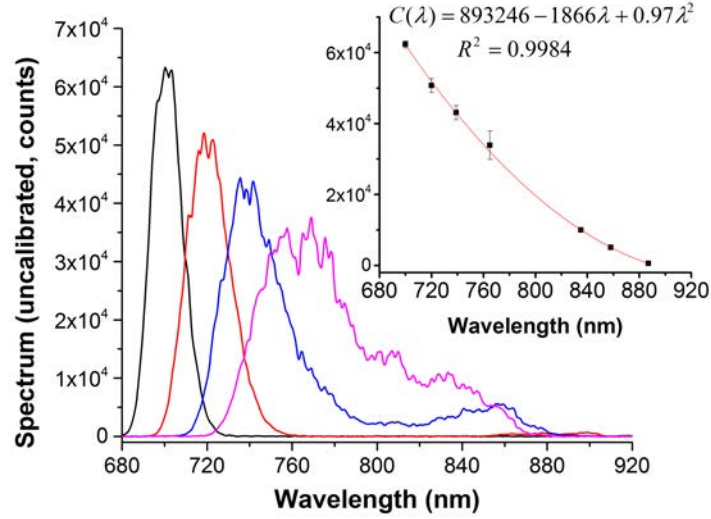


FIG. S1: A set of uncalibrated two-color spectra of PDC. The inset shows the height of each peak, with polynomial fit.

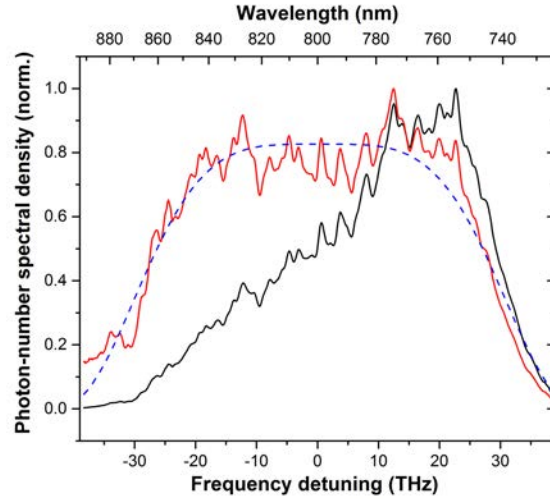


FIG. S2: Photon-number spectral density of degenerate collinear PDC calibrated using the properties of two-color PDC (solid red curve), its sinc^2 curve fit with eqs. (S1) (blue dashed curve), and the uncalibrated spectrum (solid black curve). The frequency detuning is defined as $\Omega/2\pi$.

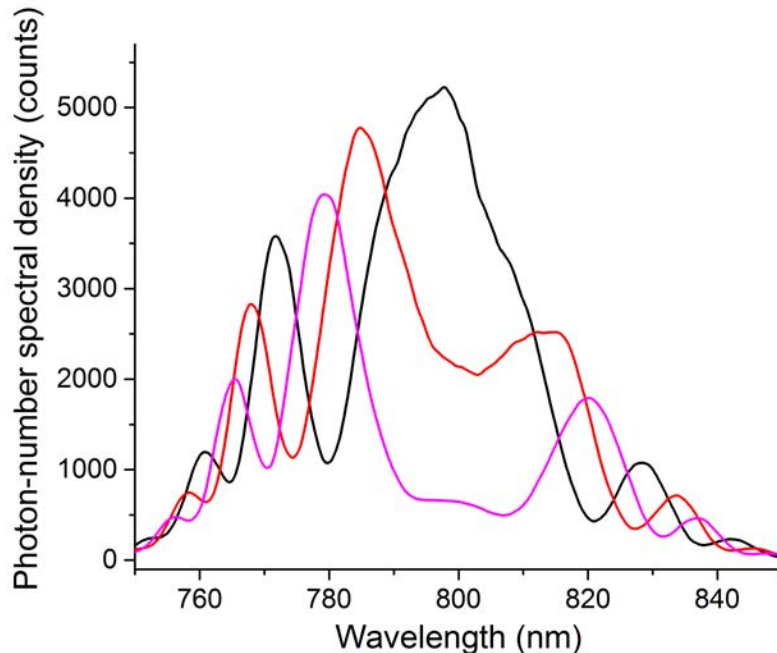


FIG. S3: Measured spectra for different relative phases between the pump and PDC, where the dispersive medium is an 3 mm thick slab of BK7.

II. INTERFERENCE FRINGES IN THE FREQUENCY SPECTRUM

The phases that the pump, signal and idler acquire between the first and the second pass through the crystal determine the shape of the frequency spectrum. Depending on this phase, the spectrum at a certain frequency can exhibit constructive interference (amplification) or destructive interference (deamplification). For instance, in the Fig. 3 of the main text, at the wavelength 800 nm, there is constructive interference, whereas destructive interference at that wavelength would translate to two peaks with a dip at 800 nm.

The influence of this phase arises from the cosine factor in the equation (2) of the main text, and its effect on the frequency spectrum depends on whether we consider the degenerate or the two-color case. When the phase mismatch δ' is Taylor expanded around $\omega_p/2$, and assuming monochromatic pump, it can be found that δ' is quadratic with ω in the degenerate case. This translates to one larger fringe around $\omega_p/2$ and progressively thinner fringes for larger detuning. In the two-color case, δ' is linear with ω , with fringes being more densely packed than in the degenerate case.

Increasing the amount of GVD inside the interferometer has two effects. First, it narrows the frequency width to be amplified in the second crystal, as illustrated in the Fig. 1 of the main text. Second, it makes the interference fringes inside the frequency spectrum more narrow. With enough GVD, and assuming no phase mismatch at $\omega_p/2$, the frequency width to be amplified is roughly as wide as the fringe around $\omega_p/2$, resulting in a strong single peak and no apparent destructive interference in the spectrum.

Phase drifts in the interferometer can have a dramatic effect on the shape of the frequency spectrum, even more so in our setup where the pump and the PDC propagate in two different arms. The experimental spectra for a very low amount of GVD (0.14 ps^2 , caused by a 3 mm thick slab of BK7) show an evolution of the interference fringes in the frequency spectrum (Fig. S3) and, in doing so, a transition between a strong central peak to weaker side peaks. For obtaining these spectra, we made use of the natural phase drift in the interferometer due to the temperature instability and air flow.

[1] D. N. Klyshko, *Photons and Nonlinear Optics* (CRC Press, 1988).

Chapter 3

Bright squeezed vacuum in a nonlinear interferometer: Frequency and temporal Schmidt-mode description

This paper provides a theoretical description of multi-mode parametric down-conversion based on the Schmidt-mode decomposition of the joint-spectral amplitude.

The Hamiltonian of eq. (4) was obtained by making an assumption about energy conservation between the photon pairs and the pump. This approximation is very useful in order to find squeezing eigenmodes, as in [32]. In fact, the Hamiltonian of eq. (4) corresponds to a time-averaged Hamiltonian, or the first term in a Magnus expansion [46]. A proper treatment of the wave-function would require to take into account time ordering between the Hamiltonians at different times. Another solution is to work in the Heisenberg picture and compute the creation and annihilation operators at different times, which is what we do in chapter 4.

This project is the culmination of long-lasting efforts and many exchange between the experimentalists and theorists. In the early experiments for this project, Timur Iskhakov and I fleshed out the crucial effect of the air gap between the crystals, leading to constructive or destructive interference. I provided insights to the article, from the perspective of an experimentalist. I helped polish the theory, namely the limitations of the model regarding the assumption that the signal and idler photons should conserve energy. I helped write the part about the similarity between the $SU(1,1)$ interferometer and induced coherence.

A big chunk of efforts were made towards computing the higher-order terms of the Magnus expansion for high-gain PDC following the prescription of [46]. The goal was to better understand the effect of time-ordering, and the transition between low-gain to high-gain PDC. I worked on this project with Louis Vallée, Enno Giese and Robert Boyd.

Bright squeezed vacuum in a nonlinear interferometer: Frequency and temporal Schmidt-mode description

P. R. Sharapova,¹ O. V. Tikhonova,^{2,3} S. Lemieux,⁴ R. W. Boyd,^{4,5} and M. V. Chekhova^{2,6,7}

¹*Department of Physics and CeOPP, University of Paderborn, Warburger Strasse 100, D-33098 Paderborn, Germany*

²*Physics Department, Moscow State University, Leninskiye Gory 1-2, Moscow 119991, Russia*

³*Skobeltsyn Institute of Nuclear Physics, Lomonosov Moscow State University, Moscow 119234, Russia*

⁴*Department of Physics, University of Ottawa, 25 Templeton Street, Ottawa, Ontario K1N 6N5, Canada*

⁵*Institute of Optics, University of Rochester, Rochester, New York 14627, USA*

⁶*Max-Planck Institute for the Science of Light, Staudtstrasse 2, Erlangen D-91058, Germany*

⁷*University of Erlangen-Nürnberg, Staudtstrasse 7-B2, Erlangen D-91058, Germany*



(Received 8 February 2018; published 21 May 2018)

Control over the spectral properties of the bright squeezed vacuum (BSV), a highly multimode nonclassical macroscopic state of light that can be generated through high-gain parametric down conversion, is crucial for many applications. In particular, in several recent experiments BSV is generated in a strongly pumped SU(1,1) interferometer to achieve phase supersensitivity, perform broadband homodyne detection, or tailor the frequency spectrum of squeezed light. In this work, we present an analytical approach to the theoretical description of BSV in the frequency domain based on the Bloch-Messiah reduction and the Schmidt-mode formalism. As a special case we consider a strongly pumped SU(1,1) interferometer. We show that different moments of the radiation at its output depend on the phase, dispersion, and the parametric gain in a nontrivial way, thereby providing additional insights on the capabilities of nonlinear interferometers. In particular, a dramatic change in the spectrum occurs as the parametric gain increases.

DOI: [10.1103/PhysRevA.97.053827](https://doi.org/10.1103/PhysRevA.97.053827)

I. INTRODUCTION

Bright squeezed vacuum (BSV) is a macroscopic nonclassical state of light that exhibits strong correlations between the signal and idler beams (twin-beam squeezing) [1–4], quadrature squeezing [5,6], polarization entanglement [7], and so on, making it attractive for applications in quantum imaging [8–10] and quantum metrology [11,12]. The BSV produced in a traveling-wave parametric amplifier is characterized by a highly multimode structure [9,13,14]. Depending on the choice of modes, one can observe quadrature squeezing or twin-beam squeezing; two different nonclassical effects [15]. Due to the strong multiphoton correlations and complicated mode structure, the theoretical description of BSV is difficult.

Earlier works on the theoretical description of BSV [16–20] used a numerical approach based on solving a set of coupled integrodifferential equations. In Refs. [16–18], the Heisenberg picture was used in the Fourier space, and the analytical solution was only found for a very narrow band pump. In Refs. [19,20], broadband (Schmidt) modes were introduced and the effect of time ordering was considered, followed by a numerical treatment. However, recent experiments where the spectral properties of BSV are modified, in particular, by using it in a nonlinear interferometer [21–24], are still lacking a detailed theoretical description.

Here we present a consistent analytical approach to the description of BSV in the frequency domain. Our approach is based on the collective Schmidt operators and allows us to take into account multiphoton correlations and nonclassical features of BSV radiation and to analyze different characteristics

of BSV for various experimental configurations. In particular, we analyze a nonlinear SU(1,1) interferometer [21,22,25–28] containing a dispersive medium [23,24], which allows one to engineer the spectral properties of BSV. High-gain effects, such as the dramatic narrowing of the BSV spectrum and the generation of tunable two-color BSV, as well as the transition from low to high parametric gain, are described in terms of the Schmidt modes. The basic idea of the developed theoretical approach appears to be rather general and can be used to describe the spatial properties of BSV as well [29].

II. FORMALISM OF THE FREQUENCY SCHMIDT MODES

Parametric down-conversion (PDC) in a crystal with a quadratic susceptibility $\chi^{(2)}(\mathbf{r})$ is described by the following Hamiltonian [28] in terms of electromagnetic field operators:

$$H \sim \int d^3\mathbf{r} \chi^{(2)}(\mathbf{r}) E_p^{(+)}(\mathbf{r}, t) E_s^{(-)}(\mathbf{r}, t) E_i^{(-)}(\mathbf{r}, t) + \text{H.c.}, \quad (1)$$

where s, i, p indices correspond to the signal, idler, and pump radiation, respectively. In this work, in contrast to Ref. [29], we consider a pulsed pump, for which the envelope of $E_p^{(+)}(\mathbf{r}, t)$ depends on time.

We assume a classical pump with a Gaussian envelope, $E_p^{(+)}(\mathbf{r}, t) = E_0 e^{-\frac{t^2}{2\tau^2}} e^{i(\mathbf{k}_p \mathbf{r} - \omega_p t)}$, with the full width at half maximum (FWHM) of the intensity pulse being $2\sqrt{\ln 2} \tau$. First, we will consider the case of a single crystal where PDC is produced. Further, this model will be generalized to other experimental configurations. By using the expansion

of the quantum fields over plane-wave modes, $E_{s,i}^{(-)}(\mathbf{r}, t) = \int d\mathbf{k}_{s,i} C_{\mathbf{k}_{s,i}} e^{-i(\mathbf{k}_{s,i}\mathbf{r} - \omega_{s,i}t)} a_{\mathbf{k}_{s,i}}^\dagger$, with the summation replaced for convenience by integration, the Hamiltonian becomes

$$H \sim i \iint d\mathbf{k}_s d\mathbf{k}_i d^3\mathbf{r} \chi^{(2)}(\mathbf{r}) E_0 C_{\mathbf{k}_s} C_{\mathbf{k}_i} e^{-\frac{t^2}{2\tau^2}} \times e^{i(\mathbf{k}_p - \mathbf{k}_s - \mathbf{k}_i)\mathbf{r}} e^{i(\omega_s + \omega_i - \omega_p)t} a_{\mathbf{k}_s}^\dagger a_{\mathbf{k}_i}^\dagger + \text{H.c.} \quad (2)$$

In the Hamiltonian (2) the integration runs over all wave vectors of the signal and idler photons and over the three spatial variables. However, in what follows, we will restrict our consideration to the collinear propagation of the photons only, and neglect the transverse wave-vector components. Then, the integration over the three-dimensional wave-vector domain is equivalent to the integration over frequencies. From the experimental viewpoint it means, in particular, that we consider a sufficiently broad spatial pump beam. In this case, the Hamiltonian can be written as

$$H \sim i \iint d\omega_s d\omega_i \int_{-L}^0 dz e^{-\frac{t^2}{2\tau^2}} e^{i(k_p - k_s - k_i)z} \times e^{i(\omega_s + \omega_i - \omega_p)t} a_{\omega_s}^\dagger a_{\omega_i}^\dagger + \text{H.c.}, \quad (3)$$

where we assume that coefficients $C_{\mathbf{k}_{s,i}}$ are frequency independent, and that $\chi^{(2)}$ is constant over the length of the crystal L ($\chi_0^{(2)}$) and zero elsewhere.

Let us represent the Gaussian temporal envelope of the pump as a Fourier transform: $\exp\{-\frac{t^2}{2\tau^2}\} \exp\{-i\omega_p t\} = \int d\omega \exp\{-\frac{(\omega - \omega_p)^2}{2\Omega^2}\} \exp\{-i\omega t\}$, where $\Omega = 1/\tau$. Then, we assume that each photon of the pump spectrum gives rise to the signal and idler photons with the energy mismatch being exactly zero, $\omega = \omega_s + \omega_i$. This approximation is well satisfied for an SU(1,1) interferometer because of the effective narrowing of the spectrum due to the nonlinear interference [28]. This leads to a δ -function $\delta(\omega - \omega_s - \omega_i)$ removing the integration over ω , and the Hamiltonian takes the form

$$H = i\hbar\Gamma \iint d\omega_s d\omega_i \exp\left\{-\frac{(\omega_s + \omega_i - \omega_p)^2}{2\Omega^2}\right\} \times \int_{-L}^0 dz e^{i(k_p - k_s - k_i)z} a_{\omega_s}^\dagger a_{\omega_i}^\dagger, \quad (4)$$

where $a_{\omega_{s,i}}^\dagger$ are the photon creation operators for the monochromatic signal (idler) frequency modes, and $\Gamma \sim \chi_0^{(2)} E_0$ is the effective coupling strength.

The approximation of zero energy mismatch restricts the generality of our model, which, for instance, fails to describe the broadening of the spectrum with increasing parametric gain [30]. On the other hand, we take into account the whole spectral width of the pump, signal or idler pulses, and the wave-vector mismatch, which allows us to obtain the analytical solution to the problem and to describe many features of BSV. After integrating in z , the PDC Hamiltonian can be represented in the simple form

$$H = i\hbar\Gamma \int d\omega_s d\omega_i F(\omega_s, \omega_i) a_{\omega_s}^\dagger a_{\omega_i}^\dagger + \text{H.c.}, \quad (5)$$

with the two-photon amplitude (TPA) $F(\omega_s, \omega_i)$ depending only on the signal and idler frequencies

$$F(\omega_s, \omega_i) = C \exp\left\{-\frac{(\omega_s + \omega_i - \omega_p)^2}{2\Omega^2}\right\} \text{sinc}\left(\frac{\Delta k L}{2}\right) \times \exp\left\{-i\frac{\Delta k L}{2}\right\}, \quad (6)$$

where C is the normalization constant and $\Delta k = k_p(\omega_s + \omega_i) - k_s(\omega_s) - k_i(\omega_i)$ is the wave-vector mismatch inside the crystal. The signal and idler wave vectors $k_{s,i} = n_{s,i}(\omega_{s,i})\omega_{s,i}/c$ depend on the refractive indices $n_{s,i}(\omega_{s,i})$ which can be calculated by using dispersion (Sellmeier) formulas [31]. The interaction Hamiltonian (5) indicates correlations between the signal and idler monochromatic-wave photons. It is more convenient to introduce new spectral modes that will be independent of each other. Such a procedure is similar to using normal coordinates for the description of interacting harmonic oscillators. In our case we can use the Schmidt decomposition [32] and present a bipartite TPA as

$$F(\omega_s, \omega_i) = \sum_n \sqrt{\lambda_n} u_n(\omega_s) v_n(\omega_i), \quad (7)$$

where λ_n are the eigenvalues and $u_n(\omega_s), v_n(\omega_i)$ are the Schmidt modes [33,34].

After the Schmidt decomposition, new photon operators can be introduced that are responsible for the creation or annihilation of a photon not with a certain frequency but with the spectral distribution determined by a certain Schmidt mode function

$$A_n^\dagger = \int d\omega_s u_n(\omega_s) a_{\omega_s}^\dagger, \\ B_n^\dagger = \int d\omega_i v_n(\omega_i) a_{\omega_i}^\dagger. \quad (8)$$

The Schmidt-mode operators (8) are similar to the broadband operators used in Ref. [19]. In terms of these operators, the PDC Hamiltonian is diagonalized [15]

$$H = i\hbar\Gamma \sum_n \sqrt{\lambda_n} (A_n^\dagger B_n^\dagger - A_n B_n). \quad (9)$$

The new modes are independent and the operators (8) satisfy the usual commutation relations

$$[A_n, A_m^\dagger] = \delta_{mn}, \quad [A_n, B_m^\dagger] = 0. \quad (10)$$

Using the commutation relations one can obtain the Heisenberg equations for the Schmidt modes

$$\frac{dA_n}{dt} = \Gamma \sqrt{\lambda_n} B_n^\dagger, \\ \frac{dB_n^\dagger}{dt} = \Gamma \sqrt{\lambda_n} A_n. \quad (11)$$

The solutions to these equations are given by the Bogolyubov transformations and provide the output operators, after an interaction time T with the crystal, in terms of the initial (vacuum) operators

$$A_n^{\text{out}} = A_n^{\text{in}} \cosh[G\sqrt{\lambda_n}] + [B_n^{\text{in}}]^\dagger \sinh[G\sqrt{\lambda_n}], \\ B_n^{\text{out}} = B_n^{\text{in}} \cosh[G\sqrt{\lambda_n}] + [A_n^{\text{in}}]^\dagger \sinh[G\sqrt{\lambda_n}],$$

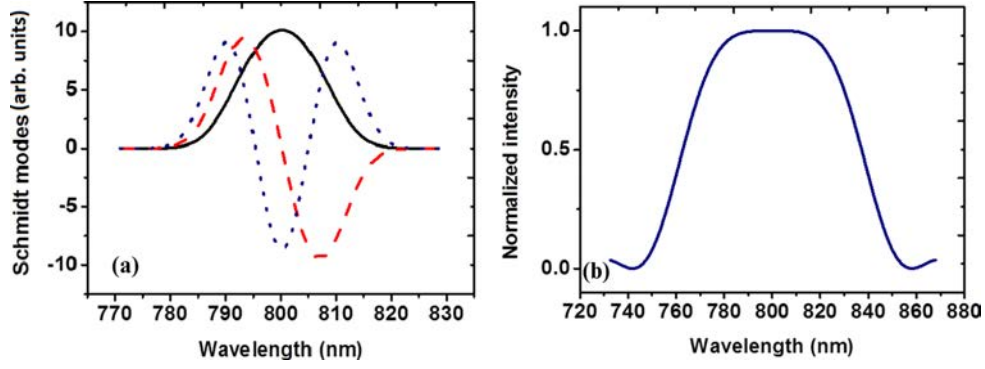


FIG. 1. For BSV generated under degenerate collinear phase matching in a single 3-mm BBO crystal pumped by 1-ps pulses at the wavelength $\lambda_p = 400$ nm: (a) the Schmidt modes u_0 (black), u_1 (red), and u_2 (blue); (b) the normalized intensity distribution for parametric gain $G=1$.

where $A_n^{\text{in}}, B_n^{\text{in}}$ are the initial (vacuum) photon annihilation operators in the corresponding Schmidt mode (8) and $G = \Gamma \times T$ corresponds to the parametric gain. Also, using the commutation relations one can obtain the Heisenberg equations for the monochromatic-wave operators

$$\frac{da_{\omega_s}}{dt} = \Gamma \sum_n \sqrt{\lambda_n} u_n(\omega_s) [B_n^{\text{out}}]^\dagger. \quad (12)$$

The solutions to these equations yield the output monochromatic-wave operators in terms of the initial vacuum operators for each frequency from the spectrum. For example, for the signal radiation

$$a_{\omega_s}^{\text{out}} = a_{\omega_s}^{\text{in}} + \sum_n u_n(\omega_s) \{ [B_n^{\text{in}}]^\dagger \sinh(\sqrt{\lambda_n} G) + A_n^{\text{in}} [\cosh(\sqrt{\lambda_n} G) - 1] \}. \quad (13)$$

In the degenerate case, the signal and idler photons have the same Schmidt modes, $A_n = B_n$.

This simple analytical expression allows one to calculate various characteristics of BSV, such as the mean photon number, the variance of the photon number difference in the signal and idler beams, the correlation functions and so on, for different experimental configurations.

According to our approach the spectral distribution of the signal beam is given by the incoherent sum of independent

Schmidt modes with the weights Λ_n ,

$$\langle N_s(\omega_s) \rangle = \sum_n |u_n(\omega_s)|^2 \Lambda_n. \quad (14)$$

In the simplest case of a single crystal the Schmidt modes are very close to the Hermite functions [33]. Typical spectral distributions for three lowest-order Schmidt modes are presented in Fig. 1(a). The modes contribute independently to the total signal and in the case of a large number of modes give rise to a rather broad spectral distribution [Fig. 1(b)].

The weight of each Schmidt mode depends on the parametric gain so that the new Schmidt coefficients Λ_n determining the contributions of different modes into the spectral distribution are redistributed. In the high-gain regime they sufficiently differ from the initial ones λ_n :

$$\Lambda_n = \frac{(\sinh[G\sqrt{\lambda_n}])^2}{\sum_n (\sinh[G\sqrt{\lambda_n}])^2}. \quad (15)$$

It means that with increasing the parametric gain the distribution of the Schmidt coefficients becomes sharper [Fig. 2(a)]; in other words, the effective number of modes contributing to the total signal decreases [Fig. 2(b)] [35].

The effective number of modes is defined by the Schmidt number $K = \frac{1}{\sum_n \Lambda_n^2}$ [35–37] and is reduced with the increase of the parametric gain [Fig. 2(b)]. It means that in the high-gain limit only the first Schmidt mode will contribute to the total

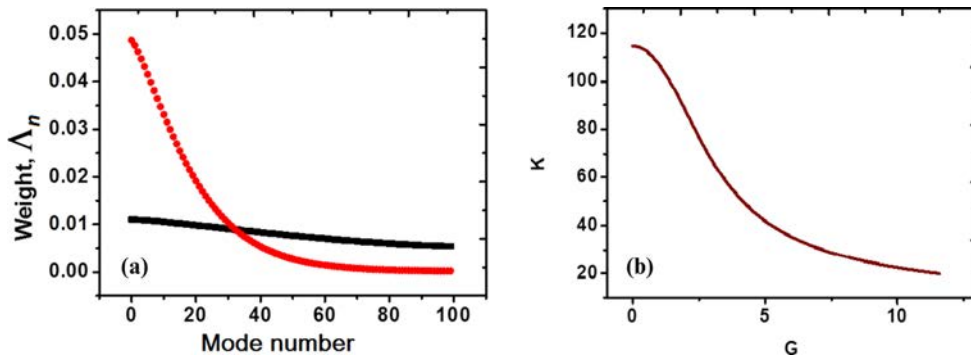


FIG. 2. Weights of the Schmidt modes for BSV generated under degenerate collinear phase matching in a single BBO crystal of length 3-mm pumped by 1-ps pulses at 400 nm: (a) the Schmidt eigenvalues for different values of the parametric gain $G = 1$ (black) and $G = 9$ (red); (b) the Schmidt number vs parametric gain.

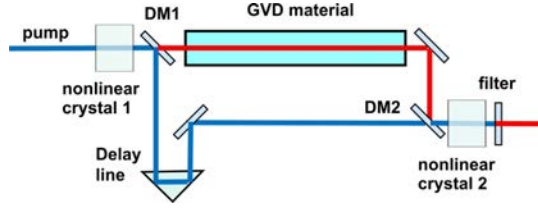


FIG. 3. An SU(1,1) interferometer with GVD. BSV is generated in the first nonlinear crystal. The dichroic mirror DM1 separates the pump from the BSV. The BSV propagates through the GVD material while the pump propagates through the air and its time delay can be adjusted. After the dichroic mirror DM2 the pump and the BSV radiation overlap in the second nonlinear crystal. Finally, the BSV is filtered from the pump.

signal and all features of the PDC radiation will be defined by the properties of this Schmidt mode.

Because the profiles of the Schmidt modes are assumed to not depend on the parametric gain, the model predicts the narrowing of the total spectral width of BSV with the gain increase. While this is not the case for a single crystal, where small spectral broadening can be observed with the gain increase [30], the narrowing of the spectrum is indeed observed for a nonlinear interferometer [24], considered in the next section.

III. NONLINEAR INTERFEROMETER WITH GROUP-VELOCITY DISPERSION

The above-described theoretical approach can be applied to different experimental configurations as long as we can obtain the TPA. An interesting experimental configuration that allows one to engineer the BSV spectrum and mode content includes two nonlinear crystals separated by a medium with large group velocity dispersion (GVD), a nonlinear SU (1,1) interferometer [21–24,38] (Fig. 3). In such a configuration, the radiation is down-converted in one nonlinear crystal and can be amplified or deamplified in the other one, depending on the coherent phase conditions. In the presence of the dispersive medium, BSV generated in the first crystal is spread in time and in addition, acquires a chirp. Its different spectral components propagate inside the GVD medium with their own group velocities. If, in addition, the pump pulse is delayed, only a certain spectral band of the down-converted radiation spectrum will overlap with it in time in the second crystal (Fig. 3) and get amplified there. This way, by changing the time delay of the pump with respect to the PDC radiation one can vary the mode structure of the BSV.

For the two-crystal configuration with the GVD medium (Fig. 3), the TPA (6) is modified; in addition to the envelope, the modulation term appears [14,39]:

$$F(\omega_s, \omega_i) = C \exp \left\{ -\frac{(\omega_s + \omega_i - \omega_p)^2}{2\Omega^2} \right\} \text{sinc} \left(\frac{\Delta k L}{2} \right) \exp \left\{ -i \frac{\Delta k L}{2} \right\} \\ \times \cos \left\{ \frac{\Delta k L + \Delta k_a d_a + (k_p^a d_0 - k_s^g d - k_i^g d)}{2} \right\} \exp \left\{ -i \frac{\Delta k L + \Delta k_a d_a + (k_p^a d_0 - k_s^g d - k_i^g d)}{2} \right\}, \quad (16)$$

where k_s^g, k_i^g are the wave vectors of signal and idler photons in the GVD medium, d is the length of the GVD medium, d_0 is the additional pump path length, which can be varied in the experiment, $\Delta k_a = k_p^a - k_s^a - k_i^a$ is the wave-vector mismatch in the air, with $k_{p,s,i}^a$ being the corresponding wave vectors for the pump, signal, and idler radiation, and d_a is the length of the air gap where all three beams propagate together. All wave-vector mismatches can be calculated directly from the dispersive (Sellmeier) formulas. Let us denote the part of the argument of the cosine function that is due to the dispersive medium and the air gap as $\phi(\omega_s, \omega_i) = [\Delta k_a d_a + (k_p^a d_0 - k_s^g d - k_i^g d)]/2$.

Depending on this phase and its derivative, the BSV structure can be substantially changed. The derivative of the phase depends on the relation between the group velocities of the pump and the BSV radiation. Due to varying the additional pump path d_0 one can change the phase derivative and satisfy the extremum condition

$$\frac{d\phi}{d\omega_i} = 0, \quad \frac{d\phi}{d\omega_s} = 0 \quad (17)$$

for different frequencies. Such a condition can be considered as a requirement of the group velocity matching between the pump and the chosen BSV frequency. In other words, this condition will be fulfilled for the frequency band in the signal

radiation that overlaps in time with the pump pulse in the second crystal.

Figure 4(a) shows the phase shape ϕ versus the signal and idler frequencies in the case where condition (17) is fulfilled for the degenerate frequency $\omega_s = \omega_i = \omega_p/2$. It means that the pump and the PDC radiation at the degenerate frequency (shown by the orange arrow) perfectly overlap in time in the second nonlinear crystal.

If the pump pulse overlaps in time in the second crystal with the PDC radiation for a certain nondegenerate frequency, the

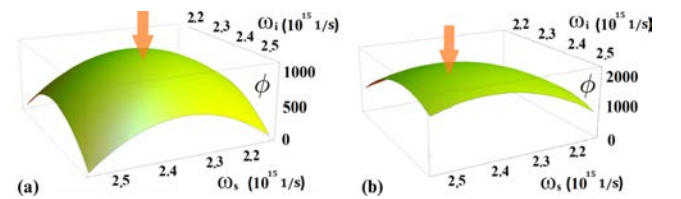


FIG. 4. The profile of the phase ϕ in the cases where the pump pulse overlaps in the second crystal with the PDC radiation at (a) the degenerate frequency and (b) a nondegenerate frequency. The orange arrow shows the overlapping frequency. The calculation was done for the case of SF6 Schott glass of length $d = 36$ cm used as the GVD medium. The other parameters are as mentioned above.

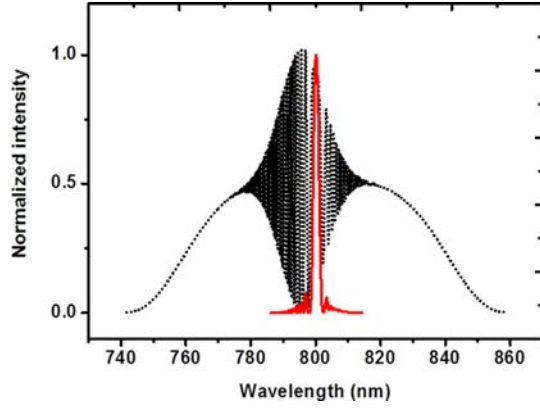


FIG. 5. Normalized intensity distribution for an SU(1,1) interferometer with 36 cm of SF6 glass. The pump pulse overlaps in the second crystal with the frequency-degenerate part of the PDC radiation. Black dotted line: parametric gain $G = 1$, red solid line: parametric gain $G = 13$.

extremum condition (17) will be fulfilled for this frequency. Figure 4(b) shows the phase profile in such a case, the orange arrow shows the chosen frequency.

Another factor affecting the BSV features is the total value of the phase ϕ . Depending on ϕ , the radiation from the first crystal is amplified or deamplified in the second one. For a fixed frequency, this can be changed by slightly varying the pump path between the GVD medium and the second crystal. Indeed, this almost does not affect the group delay but changes sufficiently the total phase. Thereby by changing the experimental parameters we can obtain different shapes of the TPA. And as long as we know the TPA for the chosen experimental configuration, we can provide its Schmidt decomposition and apply the theoretical approach described above.

To investigate the effect of the GVD medium on the BSV structure we consider $d = 36$ cm of highly dispersive glass (SF6, $k'' = 199.01$ fs²/mm). First, we chose the additional pump path and the air gap between the GVD medium and the second crystal so that both conditions, for overlapping between the pump and signal pulse in the second crystal (17) and for the amplification ($\phi = 0$), are satisfied for the degenerate

frequency. The intensity distribution calculated for the case of low parametric gain is shown in Fig. 5 by a black curve. It has a rather broad envelope with fast interference oscillations at the center. The interference fringes as well as the broad spectrum profile indicate the multimode structure of the down-converted radiation. As the parametric gain increases, the number of modes is reduced, and the spectrum gets narrower. At high gain (Fig. 5, red curve), the intensity distribution shrinks drastically compared to the low-gain regime and, as we will show further, the radiation becomes nearly single-mode in this case. One can see a similarity between the spectra shown in Fig. 5 for lower and higher gain values and the results of Refs. [23,24], respectively.

The effective number K of the Schmidt modes is given by the second-order normalized intensity correlation function for the integral spectrum, $g^{(2)} = 1 + 2/K$ for the degenerate case. The calculated dependence of $g^{(2)}$ on the length of the SF6 glass is shown in Fig. 6(a). One can observe a fast modulation, on the micrometer scale, caused by the variation of ϕ and the resulting oscillations from amplification to deamplification. Even a very small change in the GVD medium length makes the total phase significantly different, which results in the strong nonmonotonic dependence of $g^{(2)}$ on the medium length. The oscillation period at the degenerate wavelength can be calculated from the equation $(k_s^s|_{\omega_p} + k_i^s|_{\omega_p})d = \pi$ and is $0.224 \mu\text{m}$. The sharp peaks in the correlation function are much narrower than oscillations in a conventional interferometer and indicate its phase supersensitive features [12]. The same behavior had been observed in the case of an interferometer with the air gap [14].

These fast oscillations can be eliminated by providing constructive interference for a given wavelength through phase locking the interferometer. Under such a condition, the correlation function grows monotonically with the increase in the GVD medium length [Fig. 6(b)], achieves its maximal value and then decreases due to the contribution of higher-order Schmidt modes.

From Fig. 6(b), it is also clear that with increasing the parametric gain, the maximal value of $g^{(2)}$ goes up. For the gain $G = 13$, it achieves $g^{(2)} = 3$, which corresponds to the case of a single temporal mode. Thus, by choosing appropriate experimental parameters, namely, a sufficiently long GVD medium and a sufficiently high pump power at the

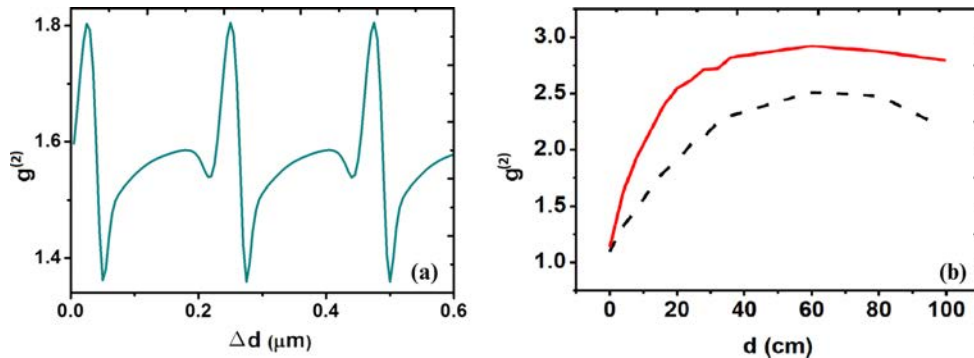


FIG. 6. Normalized second-order intensity correlation function at the output of the SU(1,1) interferometer calculated versus the length of the SF6 glass for the same configuration as in Fig. 5: (a) for the length of the GVD medium $d = \bar{d} + \Delta d$, $\bar{d} = 5$ cm, Δd is varied, the parametric gain $G = 13$ and (b) under conditions (17) and $\phi = 0$ for different parametric gain values: $G = 8.5$ (black dashed line), $G = 13$ (red solid line).

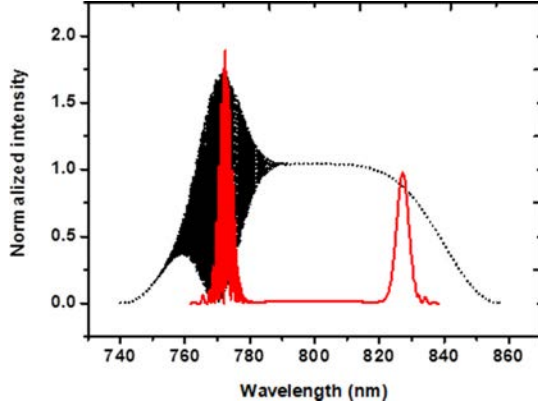


FIG. 7. Normalized intensity distribution for an SU (1,1) interferometer with 36 cm of SF6 glass. The pump pulse overlaps in the second crystal with the PDC radiation at nondegenerate wavelength 827 nm. Black dotted line: parametric gain $G = 1$, red solid line: parametric gain $G = 13$.

same time, one can achieve BSV with a single frequency mode populated with a huge number of photons.

It is worth noting that in the case of a single crystal, the number of modes is also reduced with increasing the parametric gain but due to the initial huge number of modes, the single-mode regime is not achievable for reasonable pump intensities. Using the GVD medium is a much more efficient instrument for reducing the number of modes.

If, by changing the pump path, one makes the pump pulse overlap in the second crystal with the PDC radiation at a certain nondegenerate frequency, the extremum condition will be fulfilled for the conjugated frequency [Fig. 4(b)]. In this case, the spectral intensity distribution at low gain is also broad, but the interference fringes will be only observed in the conjugated frequency range (Fig. 7). This is a manifestation of the induced

coherence effect [40]: to observe interference fringes in the signal radiation from the first and the second crystals, the idler radiation from both crystals should be indistinguishable (in our case, overlap in time).

However, as the parametric gain increases, the situation changes dramatically: instead of a single broad peak, two separated peaks appear, as for nondegenerate (“two-color”) BSV generation [4]. One of these peaks is observed at the frequency satisfying condition (17), the other one at the conjugated frequency. The second peak has interference structure while the first one is smooth. Thus with increasing the parametric gain the frequency spectrum gets narrower. If in this case the pump delay is changed this process becomes tunable.

The oscillations in the spectrum of the left-hand peak in Fig. 7 are typical for two-pulse interference, observed, for instance, in pump-probe experiments [41,42]. Indeed, they originate from the two possibilities: PDC is generated in the first crystal or in the second one. However, there are important features distinguishing the “induced coherence” effect from other types of interference. First, in our case the interference structure appears in the left-hand peak only provided that the pulse at the conjugated (right-hand) frequencies overlaps with the pump in the second crystal. Second, in the high-gain regime the contributions from the first crystal and the second crystal will be unequal, in contrast to more common types of interference.

IV. SCHMIDT MODES OF TWO-COLOR BSV

The first and second Schmidt modes in the case of two-color PDC (Fig. 7) are shown in Figs. 8(a) and 8(b). One can see that they have a double-peak structure. These modes u_0, u_1 have the same eigenvalues in the Schmidt decomposition and the same intensity profiles, but different symmetry: for the first Schmidt mode, the envelope is symmetric with respect to the degenerate frequency, for the second one it is antisymmetric. It means that

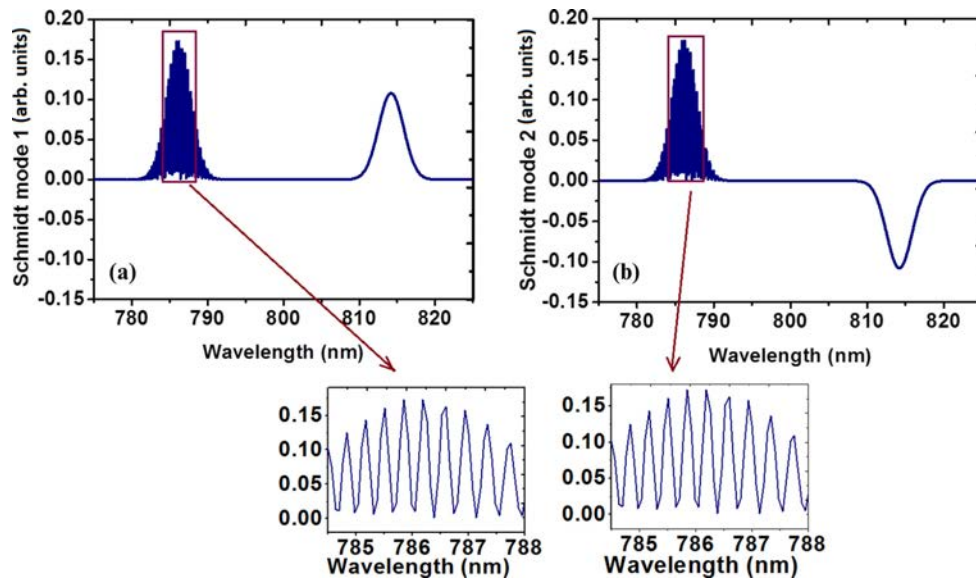


FIG. 8. The Schmidt modes u_0, u_1 for the case shown in Fig. 7, where, due to the high gain and a delay introduced in the interferometer, BSV has only two modes and its spectrum has a double-peak structure: (a) mode u_0 has a symmetric envelope, (b) mode u_1 has an antisymmetric envelope. The insets show the left peak of each mode with a better resolution.

even at a sufficiently high gain, BSV will be characterized by two-mode structure, each mode having a double peak profile.

Because the exact phase matching is achieved for the degenerate wavelength, the idler Schmidt modes have the same shape as the signal ones, i.e., $A_n = B_n$ and the diagonalized Hamiltonian (9) can be rewritten in the form

$$H = i\hbar\Gamma \sum_n \sqrt{\lambda_n} (A_n^{\dagger 2} - A_n^2). \quad (18)$$

For each mode u_n , as the ones shown in Fig. 8, one could observe quadrature squeezing; however, such an experiment is rather difficult because the local oscillator should be prepared with the same complicated profile as shown in Figs. 8(a) or 8(b).

On the other hand, instead of these “odd” and “even” Schmidt modes u_n, u_{n+1} , with the photon creation operators $A_n^\dagger, A_{n+1}^\dagger$, one can pass to their superpositions, corresponding to the operators $C_{n,n+1}^\dagger = \frac{1}{2}(A_n^\dagger + A_{n+1}^\dagger)$ and $D_{n,n+1}^\dagger = \frac{1}{2}(A_n^\dagger - A_{n+1}^\dagger)$. While the first one will have the shape of a single modulated peak [the left-hand peak in Fig. 8(a)], the second mode will have the shape of a smooth peak [the right-hand peak in Fig. 8(a)]. For these modes it is possible to observe the twin-beam squeezing which can be measured using a spectral filter for selecting $C_{n,n+1}$ and $D_{n,n+1}$ modes. The quantitative characteristic of the twin-beam squeezing is the noise reduction factor (NRF),

$$\text{NRF} = \frac{\langle (N_s - N_i)^2 \rangle - \langle N_s - N_i \rangle^2}{\langle N_s \rangle + \langle N_i \rangle}, \quad (19)$$

where $\langle N_s \rangle$ and $\langle N_i \rangle$ are the integrated numbers of photons in the signal and idler beams.

The condition $\text{NRF} < 1$ is a signature of twin-beam squeezing. For the double-peak structure of Fig. 7, the left peak corresponding to the signal beam and the right peak to the

idler one, calculation yields $\text{NRF} = 10^{-8}$ due to accuracy. This demonstrates an almost perfect twin-beam squeezing, the difference from zero caused by the oscillating structure of the left peak.

V. CONCLUSION

We present a fully analytical approach to the description of the frequency properties of BSV, based on the model of independent Schmidt modes. Within this approach, we describe the operation of an SU(1,1) interferometer with a dispersive material and its effect on the Schmidt-mode structure of the generated BSV. We show that with the transition from low to high parametric gain, the interference structure in the spectrum is replaced by a single- or a double-peak structure, depending on the path length difference in the interferometer. In the second case, the Schmidt modes also have a double-peak structure. By appropriately shaping the local oscillator, one can observe quadrature squeezing for each of the “double-peak” mode. This, however, is difficult due to the modulation of one of the peaks caused by the “induced coherence” effect. Alternatively, and in a simpler way, one can observe twin-beam squeezing by selecting the two peaks in the spectrum separately and registering their variance of the intensity difference.

ACKNOWLEDGMENTS

We acknowledge the financial support of the joint DFG-RFBR Projects No. CH 1591/2-1 and No. 16-52-12031 NNIOa and the Deutsche Forschungsgemeinschaft (DFG) via TRR 142/1, Project No. C02. We acknowledge partial financial support of the Russian Foundation for Basic Research, Grant No. 18-02-00645a. S.L. and R.W.B. acknowledge support from the Canada Excellence Research Chairs program and from the Max Planck Centre for Extreme and Quantum Photonics. P. R. Sh. thanks the state of North Rhine-Westphalia for support by the *Landesprogramm für geschlechtergerechte Hochschulen*.

-
- [1] O. Jedrkiewicz, Y.-K. Jiang, E. Brambilla, A. Gatti, M. Bache, L. A. Lugiato, and P. Di Trapani, *Phys. Rev. Lett.* **93**, 243601 (2004).
 - [2] M. Bondani, A. Allevi, G. Zambra, M. G. A. Paris, and A. Andreoni, *Phys. Rev. A* **76**, 013833 (2007).
 - [3] G. Brida, L. Caspani, A. Gatti, M. Genovese, A. Meda, and I. R. Berchera, *Phys. Rev. Lett.* **102**, 213602 (2009).
 - [4] I. N. Agafonov, M. V. Chekhova, and G. Leuchs, *Phys. Rev. A* **82**, 011801 (2010).
 - [5] N. Corzo *et al.*, *Opt. Express* **19**, 21358 (2011).
 - [6] Y. Shaked, Y. Michael, R. Z. Vered, L. Bello, M. Rosenbluh, and A. Pe’er, *Nat. Commun.* **9**, 609 (2018).
 - [7] T. Sh. Iskhakov, I. N. Agafonov, M. V. Chekhova, and G. Leuchs, *Phys. Rev. Lett.* **109**, 150502 (2012).
 - [8] G. Brida, M. Genovese, and I. R. Berchera, *Nat. Photon.* **4**, 227 (2010).
 - [9] V. Boyer, A. M. Marino, R. C. Pooser, and P. D. Lett, *Science* **321**, 544 (2008).
 - [10] A. Allevi and M. Bondani, *J. Opt.* **19**, 064001 (2017).
 - [11] G. Brida, I. P. Degiovanni, M. Genovese, M. L. Rastello, and I. R. Berchera, *Opt. Express* **18**, 20572 (2010).
 - [12] M. Manceau, G. Leuchs, F. Ya. Khalili, and M. V. Chekhova, *Phys. Rev. Lett.* **119**, 223604 (2017).
 - [13] V. Boyer, A. M. Marino, and P. D. Lett, *Phys. Rev. Lett.* **100**, 143601 (2008).
 - [14] A. M. Pérez, T. Sh. Iskhakov, P. Sharapova, S. Lemieux, O. V. Tikhonova, M. V. Chekhova, and G. Leuchs, *Opt. Lett.* **39**, 2403 (2014).
 - [15] S. L. Braunstein, *Phys. Rev. A* **71**, 055801 (2005).
 - [16] R. S. Bennink and R. W. Boyd, *Phys. Rev. A* **66**, 053815 (2002).
 - [17] W. Wasilewski, A. I. Lvovsky, K. Banaszek, and C. Radzewicz, *Phys. Rev. A* **73**, 063819 (2006).
 - [18] B. Dayan, *Phys. Rev. A* **76**, 043813 (2007).
 - [19] A. Christ, B. Brecht, W. Mauerer, and C. Silberhorn, *New J. Phys.* **15**, 053038 (2013).
 - [20] A. Eckstein, B. Brecht, and C. Silberhorn, *Opt. Express* **19**, 13770 (2011).

- [21] R. Z. Vered, Y. Shaked, Y. Ben-Or, M. Rosenbluh, and A. Pe'er, *Phys. Rev. Lett.* **114**, 063902 (2015).
- [22] Y. Shaked, R. Pomerantz, R. Z. Vered, and A. Pe'er, *New J. Phys.* **16**, 053012 (2014).
- [23] T. Sh. Iskhakov, S. Lemieux, A. M. Perez, R. W. Boyd, M. V. Chekhova, and G. Leuchs, *J. Mod. Opt.* **63**, 64 (2016).
- [24] S. Lemieux, M. Manceau, P. R. Sharapova, O. V. Tikhonova, R. W. Boyd, G. Leuchs, and M. V. Chekhova, *Phys. Rev. Lett.* **117**, 183601 (2016).
- [25] B. Yurke, S. L. McCall, and J. R. Klauder, *Phys. Rev. A* **33**, 4033 (1986).
- [26] J. Jing, C. Liu, Z. Zhou, Z. Y. Ou, and W. Zhang, *Appl. Phys. Lett.* **99**, 011110 (2011).
- [27] F. Hudelist, J. Kong, C. Liu, J. Jing, Z. Y. Ou, and W. Zhang, *Nat. Commun.* **5**, 3049 (2014).
- [28] D. N. Klyshko, *Zh. Eksp. Teor. Fiz.* **104**, 2676 (1993).
- [29] P. Sharapova, A. M. Perez, O. V. Tikhonova, and M. V. Chekhova, *Phys. Rev. A* **91**, 043816 (2015).
- [30] K. Yu. Spasibko, T. Sh. Iskhakov, and M. V. Chekhova, *Opt. Express* **20**, 7507 (2012).
- [31] V. G. Dmitriev, G. G. Gurzadyan, and D. N. Nikogosyan, *Handbook of Nonlinear Optical Crystals* (Springer, New York, 1999).
- [32] C. K. Law, I. A. Walmsley, and J. H. Eberly, *Phys. Rev. Lett.* **84**, 5304 (2000).
- [33] M. V. Fedorov, Yu. M. Mikhailova, and P. A. Volkov, *J. Phys. B: At. Mol. Opt.* **42**, 175503 (2009).
- [34] M. V. Fedorov, M. A. Efremov, P. A. Volkov, E. V. Moreva, S. S. Straupe, and S. P. Kulik, *Phys. Rev. A* **77**, 032336 (2008).
- [35] A. Allevi, O. Jedrkiewicz, E. Brambilla, A. Gatti, J. Perina, Jr., O. Haderka, and M. Bondani, *Phys. Rev. A* **90**, 063812 (2014).
- [36] I. V. Dyakonov, P. R. Sharapova, T. Sh. Iskhakov, and G. Leuchs, *Laser Phys. Lett.* **12**, 065202 (2015).
- [37] X. Guo, N. Liu, X. Li, and Z. Y. Ou, *Opt. Express* **23**, 29369 (2016).
- [38] M. V. Chekhova and Z. Y. Ou, *Adv. Opt. Photon.* **8**, 104 (2016).
- [39] D. N. Klyshko, *Photons and Nonlinear Optics* (Gordon and Breach, Philadelphia, 1988).
- [40] X. Y. Zou, L. J. Wang, and L. Mandel, *Phys. Rev. Lett.* **67**, 318 (1991).
- [41] M. Fushitani, *Annu. Rep. Prog. Chem., Sect. C: Phys. Chem.* **104**, 272 (2008).
- [42] H. Katsuki, K. Hosaka, H. Chiba, and K. Ohmori, *Phys. Rev. A* **76**, 013403 (2007).

Chapter 4

Properties of bright squeezed vacuum at increasing brightness

This work is part of an ongoing effort to understand and harness PDC in the high-gain regime. In particular, we solve the set integro-differential equations for the creation and annihilation operators for an arbitrary parametric gain and spatial profile of the pump laser. Then, we perform a Schmidt-mode decomposition on the output operators, providing valuable information about high-gain PDC as a resource in quantum metrology. This work builds upon the treatment presented by Klyshko, which considers only a planewave monochromatic pump [12].

I provided experimental results for the two-crystal configuration, and wrote parts of section IV. I have worked out a very similar derivation to compute the variance in the photon-number difference between the signal and the idler for applications in imaging [31]. Consequently, I helped revise and write the theory in section II of the article.

Properties of bright squeezed vacuum at increasing brightness

P. R. Sharapova,¹ G. Frascella,^{2,3} M. Riabinin,¹ A. M. Pérez,^{2,3} O. V. Tikhonova,^{4,5} S. Lemieux,⁶ R. W. Boyd,^{6,7} G. Leuchs,² and M. V. Chekhova^{2,3,4}

¹Department of Physics, University of Paderborn, Warburger Straße 100, Paderborn D-33098, Germany

²Max-Planck Institute for the Science of Light, Staudtstr. 2, Erlangen D-91058, Germany

³University of Erlangen-Nürnberg, Staudtstr. 7/B2, 91058 Erlangen, Germany

⁴Physics Department, Moscow State University, Leninskiye Gory 1-2, Moscow 119991, Russia

⁵Skobeltsyn Institute of Nuclear Physics, Lomonosov Moscow State University, Moscow 119234, Russia

⁶Department of Physics, University of Ottawa, 25 Templeton Street, Ottawa, Ontario, Canada K1N 6N5

⁷Institute of Optics, University of Rochester, Rochester, New York 14627, USA



(Received 28 June 2019; accepted 19 February 2020; published 27 March 2020)

A bright squeezed vacuum (BSV) is a nonclassical macroscopic state of light, which is generated through high-gain parametric down-conversion or four-wave mixing. Although the BSV is an important tool in quantum optics and has a lot of applications, its theoretical description is still not complete. In particular, the existing description in terms of Schmidt modes with gain-independent shapes fails to explain the spectral broadening observed in the experiment as the mean number of photons increases. Meanwhile, the semiclassical description accounting for the broadening does not allow us to decouple the intermodal photon-number correlations. In this work, we present a new generalized theoretical approach to describe the spatial properties of a multimode BSV. In the multimode case, one has to take into account the complicated interplay between all involved modes: each plane-wave mode interacts with all other modes, which complicates the problem significantly. The developed approach is based on exchanging the (\mathbf{k}, t) and (ω, z) representations and solving a system of integrodifferential equations. Our approach predicts correctly the dynamics of the Schmidt modes and the broadening of the angular distribution with the increase in the BSV mean photon number due to a stronger pumping. Moreover, the model correctly describes various properties of a widely used experimental configuration with two crystals and an air gap between them, namely, an SU(1,1) interferometer. In particular, it predicts the narrowing of the intensity distribution, the reduction and shift of the side lobes, and the decline in the interference visibility as the mean photon number increases due to stronger pumping. The presented experimental results confirm the validity of the new approach. The model can be easily extended to the case of the frequency spectrum, frequency Schmidt modes, and other experimental configurations.

DOI: [10.1103/PhysRevResearch.2.013371](https://doi.org/10.1103/PhysRevResearch.2.013371)

I. INTRODUCTION

At a high parametric gain, parametric down-conversion (PDC) and four-wave mixing (FWM) generate a bright squeezed vacuum (BSV). The BSV is a nonclassical state of light without a coherent component (displacement) but with a large (macroscopic) number of photons per mode. This state has strong photon-number correlations (twin-beam squeezing) [1–4], quadrature squeezing [5], multimode structure [6–8], and polarization entanglement if the generated photons have orthogonal polarizations [9]. The BSV is a promising tool for a lot of applications in quantum optics and metrology: imaging [10–14], quantum state engineering [15,16], nonlinear interferometry [17–19], super-resolution, and phase sensitivity beyond the shot-noise limit [20,21]. Due to the high

mean photon number and the large number of modes involved, a theoretical description of a BSV is complicated.

Several works on a description of a multimode BSV are based on the coupled differential equations for the signal and idler plane-wave operators under the plane-wave pump approximation [22–25]. This approximation implies that each plane-wave signal mode interacts with only one plane-wave idler mode. This simplifies the problem significantly and provides analytical expressions for the output operators. In other works, equations similar to the classical propagation equations were derived and their solutions based on the Green function method were suggested [26]. Integrodifferential equations for PDC with a fixed spectral profile of the pump were written in Refs. [27–30]. Multimode PDC in the frequency domain was studied in Refs. [31,32] using the Magnus expansion.

The broadband-mode approach for the temporal domain based on the independent Schmidt modes was introduced in Ref. [27] and developed in Ref. [28]; the Schmidt mode approach for the spatial domain was developed and applied to experiment in Ref. [33]. This approach describes several effects observed for a BSV and is very convenient for the

Published by the American Physical Society under the terms of the [Creative Commons Attribution 4.0 International](https://creativecommons.org/licenses/by/4.0/) license. Further distribution of this work must maintain attribution to the author(s) and the published article's title, journal citation, and DOI.

analytical treatment of the problem. However, the existing Schmidt mode theory neglects the energy mismatch between the pump, signal, and idler photons and therefore leads to gain-independent shapes of the Schmidt modes. For this reason, it cannot describe the broadening of the spectrum, which is observed in experiment [34] as the BSV gets brighter due to the increase in the parametric gain (stronger pumping).

Moreover, the behavior of BSV properties with the increase of the parametric gain can be completely different depending on the geometry of experiment. For PDC in a single crystal, the spatial intensity distribution has a typical “sinc-squared” shape at low parametric gain, and it broadens as the parametric gain increases (see the results below). Similar behavior was observed for the frequency spectrum in Ref. [34]. In contrast, a two-crystal configuration with an air gap in between leads to a complicated interference pattern of intensity with side lobes, which gets narrower with increasing parametric gain [17,33,35]. This configuration is known as the SU(1,1) interferometer [18], and it has recently attracted a lot of attention due to its metrological applications [21,36–39].

In this work, we present a new theoretical approach to the description of the spatial properties of the spatially multimode BSV taking into account the mode correlations. Our approach is based on exchanging the (\mathbf{k}, t) and (ω, z) representations and solving the high-dimensional system of integrodifferential equations for plane-wave operators. This approach describes various features of the BSV, such as the intensity distribution and the shapes of the Schmidt modes, as well as their evolution with increasing parametric gain, both in the case of a single crystal and in the case of a two-crystal configurations. In full agreement with the experiment, the theory predicts the broadening of both the intensity distribution and the Schmidt mode shapes with increasing gain in the case of a single crystal and the reduction of the side lobes in the two-crystal configuration. The suggested approach does not include any limitations on the pump waist width and the number of modes, as it was the case in the previous considerations, and it does not assume that the Hamiltonian commutes with itself at different moments of time.

The paper is organized as follows. Section II describes the theoretical approach and applies it to the case of high-gain PDC in a single crystal. The Schmidt modes at variable parametric gain are considered in Sec. III. Section IV deals with the two-crystal configuration. In all sections, experimental results are also presented and compared with the theory. Finally, Sec. V is the conclusion.

II. HIGH-GAIN PDC IN A SINGLE CRYSTAL

The Hamiltonian of PDC in a crystal with a quadratic susceptibility $\chi^{(2)}(\mathbf{r})$ is given by [23]

$$H \sim \int d^3r \chi^{(2)}(\mathbf{r}) E_p^{(+)}(\mathbf{r}, t) \hat{E}_s^{(-)}(\mathbf{r}, t) \hat{E}_i^{(-)}(\mathbf{r}, t) + \text{H.c.}, \quad (1)$$

where $\hat{E}_{s,i}$ are electromagnetic field operators for signal/idler photons, the pump is assumed to be a classical beam with a Gaussian envelope, propagating along the z axis, $E_p^{(+)}(\mathbf{r}, t) = E_0 e^{-\frac{x^2+y^2}{2\sigma^2}} e^{i(k_p z - \omega_p t)}$, with the full width at half maximum (FWHM) of the intensity distribution being $2\sqrt{\ln 2}\sigma$. By

using the quantization of the electromagnetic field, $\hat{E}_{s,i}^{(-)}(\mathbf{r}, t) = \int d\mathbf{k}_{s,i} C_{\mathbf{k}_{s,i}} e^{-i(\mathbf{k}_{s,i}\mathbf{r} - \omega_{s,i}t)} a_{\mathbf{k}_{s,i}}^\dagger$, where $a_{\mathbf{k}_{s,i}}^\dagger$ are the creation plane-wave operators, $C_{\mathbf{k}_{s,i}}$ are the coefficients of the decomposition, the Hamiltonian becomes

$$H = \frac{i\hbar\tilde{\Gamma}}{2\pi} \iint d\mathbf{k}_s d\mathbf{k}_i d^3\mathbf{r} e^{-\frac{x^2+y^2}{2\sigma^2}} e^{ik_p z} e^{-i(\mathbf{k}_s+\mathbf{k}_i)\mathbf{r}} \times e^{i(\omega_s+\omega_i-\omega_p)t} a_{\mathbf{k}_s}^\dagger a_{\mathbf{k}_i}^\dagger + \text{H.c.} \quad (2)$$

Here we neglect the dependence of the coefficients $C_{\mathbf{k}_{s,i}}$ on $\mathbf{k}_{s,i}$ and suppose that the interaction strength $\tilde{\Gamma}$, involving $\chi^{(2)}(\mathbf{r})$, the pump field amplitude, and other parameters is a constant. In the existing Schmidt mode approach, unlike the current approach, the frequency mismatch $\omega_s + \omega_i - \omega_p$ is neglected, which makes the Hamiltonian independent of time and ultimately leads to gain-independent Schmidt modes.

For simplicity we consider a 2D model, using only one transverse coordinate x . In systems with the radial symmetry, without loss of generality, the 2D case can be easily extended to a 3D case by taking into account the additional integral over the y coordinate. After integration over x and substituting $d\mathbf{k}_{s,i} = dq_{s,i} dk_{sz,i} dz$, where $q_{s,i}$ are the transverse wave vectors and $k_{sz,i} dz$ are the longitudinal wave vectors of signal (idler) radiation, the Hamiltonian can be represented in the form

$$H = \frac{i\hbar\tilde{\Gamma}}{2\pi} \iint dq_s dk_{sz} dq_i dk_{iz} dz e^{-\frac{(q_s+q_i)^2 \sigma^2}{2}} e^{i(k_p - k_{sz} - k_{iz})z} \times e^{i(\omega_s+\omega_i-\omega_p)t} a_s^\dagger(q_s, k_{sz}, t) a_i^\dagger(q_i, k_{iz}, t) + \text{H.c.} \quad (3)$$

This Hamiltonian is written in the momentum-time (\mathbf{k}, t) representation. In this picture, the Heisenberg equation of motion for the signal plane-wave operators takes the form

$$\frac{da_s(q_s, k_{sz}, t)}{dt} = \frac{\tilde{\Gamma}}{2\pi} \int dq_i dk_{iz} dz e^{-\frac{(q_s+q_i)^2 \sigma^2}{2}} \times e^{i(k_p - k_{sz} - k_{iz})z} e^{i(\omega_s+\omega_i-\omega_p)t} a_i^\dagger(q_i, k_{iz}, t), \quad (4)$$

and similarly for the idler operators. The operators $a_{s,i}^\dagger(q_{s,i}, k_{sz,iz}, t)$ and $a_{s,i}(q_{s,i}, k_{sz,iz}, t)$ defined before are the slowly varying parts of creation and annihilation operators. In other words, these operators are solutions to the Heisenberg equation in the rotating frame of reference. Taking into account the free-propagation Hamiltonian for the signal and idler fields, one can obtain solutions in the fixed frame of reference. We called these solutions fast varying components. The fast varying components are connected with the slowly varying parts as

$$\bar{a}_{s,i}^\dagger(q_{s,i}, k_{sz,iz}, t) = e^{i\omega_{s,i}t} a_{s,i}^\dagger(q_{s,i}, k_{sz,iz}, t), \\ \bar{a}_{s,i}^\dagger(q_{s,i}, \xi, \tilde{\omega}_{s,i}) = a_{s,i}^\dagger(q_{s,i}, \xi, \tilde{\omega}_{s,i}) e^{-ik_{sz,iz}(\tilde{\omega}_{s,i}-\omega_{s,i})\xi}. \quad (5)$$

Here we assume long pump pulses and short crystals, so that the pulse covers the entire crystal at the same time. The Fourier transformation allows one to pass from (q, k_z, t) to (q, z, ω) representation. For example, for the fast varying part of the idler creation operator, the Fourier transformation is

$$\bar{a}_i^\dagger(q_i, k_{iz}, t) = \frac{1}{2\pi} \int \bar{a}_i^\dagger(q_i, \xi, \tilde{\omega}_i) e^{i\tilde{\omega}_i t} e^{ik_{iz}\xi} d\tilde{\omega}_i d\xi. \quad (6)$$

After substituting (6) and (5) into (4) and integrating its left and right parts from $\tau_0 = -\infty$ to $\tau = +\infty$ over the

interaction time, Eq. (4) takes the form

$$a_s(q_s, k_{sz}, \tau) - a_s(q_s, k_{sz}, \tau_0) = \frac{\tilde{\Gamma}}{(2\pi)^2} \int dq_i dk_{iz} dz dt d\tilde{\omega}_i d\xi e^{-\frac{(q_s+q_i)^2 \sigma^2}{2}} e^{i(k_p - k_{sz} - k_{iz})z} \times e^{-i(\omega_s + \tilde{\omega}_i - \omega_p)t} e^{ik_{iz}\xi} a_i^\dagger(q_i, \xi, \tilde{\omega}_i) e^{-ik_{iz}(\tilde{\omega}_i, q_i)\xi}. \quad (7)$$

In real experiments, the final time τ corresponds to the end of a long interaction. Please note that $k_{iz}(\tilde{\omega}_i, q_i)$ is a function of $\tilde{\omega}_i$ and q_i , while k_{iz} is the integration variable.

The operators at the final $a_s(q_s, k_{sz}, \tau)$ and initial $a_s(q_s, k_{sz}, \tau_0)$ moments of time describe the boundary conditions. Due to these conditions, we have an equality between the operators in the end (beginning) of the interaction and operators corresponding to further (previous) free propagation in the linear medium. Outside the nonlinear medium, \mathbf{k} and ω are connected by the dispersion law $\omega = \omega(\mathbf{k})$ such that $a_{s,i}(q_{s,i}, k_{sz,i}, t)$ does not depend on t and $a_{s,i}(q_{s,i}, z, \omega_{s,i})$ does not depend on z . In this case, Eq. (6) with the substitution $k_{sz} = \frac{\omega_s}{u_{k_{sz}}}$ leads to the link between boundary conditions in different representations: $a_s(q_s, k_{sz}, \tau) = u_{k_{sz}} a_s(q_s, L, \omega_s)$, $a_s(q_s, k_{sz}, \tau_0) = u_{k_{sz}} a_s(q_s, 0, \omega_s)$ [23], where $u_{k_{sz}}$ is the projection of the group velocity vector of the signal photon on the z axis and L is the length of the nonlinear medium.

In the right-hand side of Eq. (7), integration over time and longitudinal momentum leads to the δ functions,

$$\frac{1}{2\pi} \int dt e^{-i(\omega_s + \tilde{\omega}_i - \omega_p)t} = \delta(\tilde{\omega}_i - \omega_p + \omega_s), \quad \frac{1}{2\pi} \int dk_{iz} e^{ik_{iz}(z-\xi)} = \delta(z - \xi), \quad (8)$$

the first of them defines the idler frequency through the signal and pump frequencies.

The δ functions allow one to take integrals over $d\tilde{\omega}$ and $d\tilde{z}$ and simplify Eq. (7):

$$a_s(q_s, L, \omega_s) - a_s(q_s, 0, \omega_s) = \Gamma \int dq_i \int_0^L dz e^{-\frac{(q_s+q_i)^2 \sigma^2}{2}} e^{i(k_p - k_{sz} - k_{iz}(\omega_p - \omega_s))z} \times a_i^\dagger(q_i, z, \omega_p - \omega_s), \quad (9)$$

where $\Gamma = \tilde{\Gamma}/u_{k_{sz}}$ and we assume $u_{k_{sz}} = u_{k_{iz}} = u_{k_z}$. In Eq. (9), the idler frequency is defined through the signal and pump frequencies due to Eq. (8); to emphasize it, we wrote the frequency dependence explicitly for k_{iz} in the brackets. Differentiation of the left- and right-sides of Eq. (9) with respect to the L leads to the coupled integrodifferential equations for the signal/idler annihilation/creation operators,

$$\frac{da_s(q_s, L, \omega_s)}{dL} = \Gamma \int dq_i e^{-\frac{(q_s+q_i)^2 \sigma^2}{2}} \times e^{i\Delta k L} a_i^\dagger(q_i, L, \omega_p - \omega_s), \quad (10)$$

where $\Delta k = k_p - k_{sz}(\omega_s) - k_{iz}(\omega_p - \omega_s)$. A similar equation can be written for the idler frequency,

$$\frac{da_i^\dagger(q_i, L, \omega_p - \omega_s)}{dL} = \Gamma \int dq_s e^{-\frac{(q_s+q_i)^2 \sigma^2}{2}} \times e^{-i\Delta k L} a_s(q_s, L, \omega_s). \quad (11)$$

The solution to the system of coupled integrodifferential equations (10) and (11) can be found in the form

$$a_s(q_s, L, \omega_s) = a_s(q_s) + \int dq'_s \eta(q_s, q'_s, L, \Gamma) a_s(q'_s) + \int dq'_i \beta(q_s, q'_i, L, \Gamma) a_i^\dagger(q'_i), \quad a_i^\dagger(q_i, L, \omega_i) = a_i^\dagger(q_i) + \int dq'_i \eta^*(q_i, q'_i, L, \Gamma) a_i^\dagger(q'_i) + \int dq'_s \beta^*(q_i, q'_s, L, \Gamma) a_s(q'_s), \quad (12)$$

where $\eta(q_s, q'_s, L, \Gamma)$, $\beta(q_s, q'_i, L, \Gamma)$ are functions of the transverse wave vectors, crystal length and the interaction strength, and $a_s(q_s) = a_s(q_s, L = 0, \omega_s)$, $a_i^\dagger(q_i) = a_i^\dagger(q_i, L = 0, \omega_i)$ are the initial plane-wave operators. In the case of an arbitrary pump and a high gain, the functions $\eta(q_s, q'_s, L, \Gamma)$ and $\beta(q_s, q'_i, L, \Gamma)$ can be found only numerically. However, in the low-gain regime, Eqs. (12) coincide with the solutions given by the Schmidt mode approach [33]. In addition, with the spatially broad pump, Eqs. (12) coincide with the well-known analytical solution for the plane-wave pump approximation [23].

Finally, by solving the system of integrodifferential equations (10) and (11) in the form of Eqs. (12), various characteristics of the BSV can be found. For example, the mean photon-number distribution over transverse wave vectors is

$$N_s(q_s) = \langle a_s^\dagger(q_s, L, \omega_s) a_s(q_s, L, \omega_s) \rangle = \int dq'_i |\beta(q_s, q'_i, L, \Gamma)|^2. \quad (13)$$

In what follows, we assume small angles of emission $\theta_{s,i}$, so that $q_s \approx k_s \theta_s$, and consider angular intensity distributions.

Please note that, to generalize our approach, we have considered signal and idler photons distinguishable in at least one degree of freedom (for example, noncollinear emission) and marked their operators with different indices s and i . Nevertheless, this approach can be simplified to the case of degenerate type-I PDC under the substitution $a_s = a_i$ and with taking into account the corresponding commutation relation.

To find the connection between the theoretical parameter Γ and the measured experimental gain, we have modelled the single plane-wave mode by calculating the total photon number in the collinear direction ($q_s = q_i = 0$) from Eq. (13) as a function of Γ and fitted this dependence by the well-known dependence for the single-mode regime, $y = B \sinh^2(A\Gamma)$, where A and B are the fitting parameters. Then the parametric gain is defined as $G = A\Gamma$. A similar procedure was performed in the experiment. Using a pinhole, the dependence of the total intensity in the collinear direction on the parametric gain was measured and fitted by the function $y = B_e \sinh^2(A_e \sqrt{P})$, where A_e and B_e are the fitting parameters, P is the pump power. In this case, the experimental gain is defined as $G_e = A_e \sqrt{P}$, and the theoretical and experimental gains have to coincide.

To compare the predictions of the described theory with the experiment, we considered a 2-mm-thick BBO crystal and a pump laser with the wavelength 354.7 nm and with a beam waist of FWHM 170 μm . The angular intensity

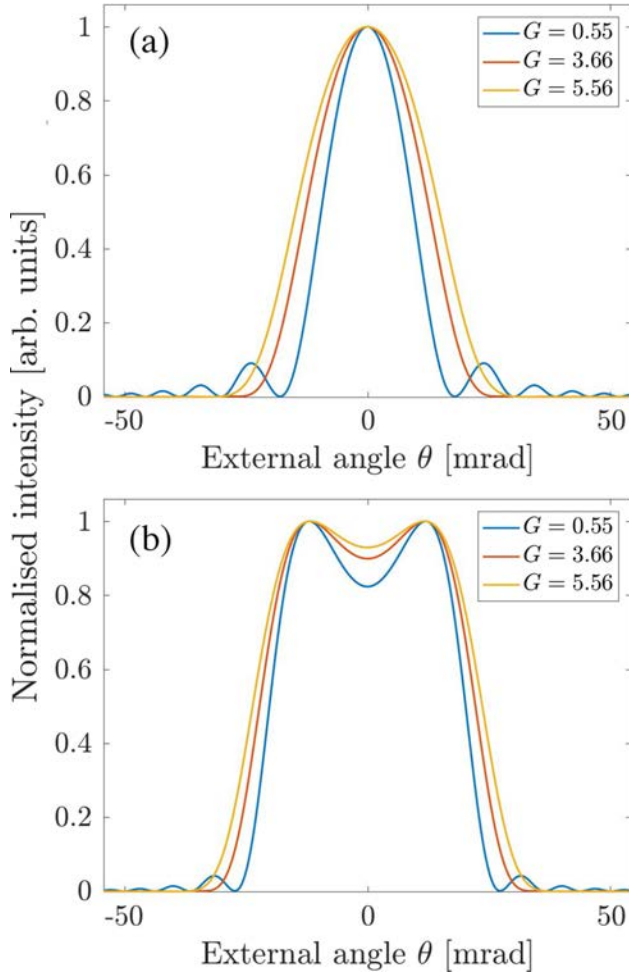


FIG. 1. The calculated normalized BSV intensity distributions for different values of the parametric gain and phase mismatch $\delta k = 4530$ (a) and -3200 m^{-1} (b).

distributions of type-I PDC were calculated using Eq. (13) for different values of the parametric gain G , as shown in Fig. 1. For ideal experimental conditions the phase mismatch $\delta k = k_p(\theta_{\text{axis}}, \omega_p) - 2k_{s,i}(\omega_{s,i}) = 0$, with θ_{axis} being the angle between the pump wave vector and the optic axis of the crystal. Due to imperfect crystal alignment, the phase mismatch can be slightly nonzero. Such a deviation is hard to fix in the experiment but has a considerable effect on the shape of the intensity distribution, which is shown in panels (a) and (b) of Fig. 1.

It is clearly seen that with increasing parametric gain the angular intensity distribution broadens. The broadening is directly connected with the fact that the angular variables and the parametric gain both enter the functions β and η . In contrast, in the Schmidt mode approach, the angular variables and the parametric gain are separate: the eigenmodes depend only on the angular variables, the eigenvalues depend only on the parametric gain, the broadening is not expected. The origin of the broadening can be clearly seen under the plane-wave pump approximation, where strong correlations between the signal and the idler photons take place: $q_s = -q_i$.

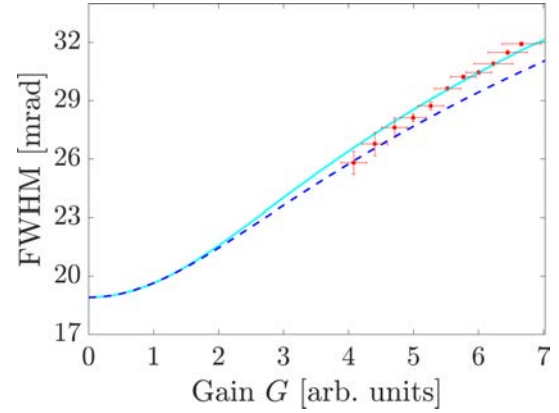


FIG. 2. The theoretical FWHM of the BSV intensity distribution vs parametric gain for a $170 \text{ }\mu\text{m}$ FWHM pump (cyan solid line) and plane-wave pump (blue dashed line) calculated according to the approach of Refs. [23,24], and the experimental data (red dots).

In experiment, a BSV was obtained through PDC pumped by the third harmonic radiation (wavelength 354.7 nm) of a pulsed Nd:YAG laser. The pulsed radiation (pulse width 18 ps , repetition rate 1 kHz) is essential to reach the high-gain regime. The intensity distributions were recorded with a charge-coupled device (CCD) camera in the Fourier plane of a lens with the focal length of 100 mm . The spectral filtering was performed using a band-pass filter with the transmission centered around the wavelength 710 nm and with a bandwidth of 10 nm .

The dependence of the FWHM of the spatial intensity distribution of the BSV on the parametric gain for $\delta k = 4530 \text{ m}^{-1}$ (obtained by fitting the experimental distributions and fixed for further calculations) was calculated and compared with the experimental data, see Fig. 2. In the low-gain regime, the FWHM of the BSV intensity distribution coincides with the value calculated using the first-order perturbation theory [40]. As the parametric gain increases, the FWHM monotonically grows. The same tendency is observed in the experiment (red points) and is in good agreement with the theoretical dependence (cyan line). The blue dashed line, calculated for the case of a plane-wave pump, predicts a slower broadening of the angular distribution than the one with a focused pump. Note that in the gain-independent Schmidt mode approach, the FWHM decreases with increasing gain, contrary to experiment.

III. SCHMIDT MODES

The BSV radiation is strongly multimode. This multimode structure is important for a lot of applications [11] but, at the same time, is difficult to analyze. The most useful way to describe the multimode BSV radiation is by introducing a system of normalized orthogonal Schmidt modes. Within the Schmidt mode basis, each signal mode is only correlated with a single matching idler mode, which greatly facilitates the analysis.

In a simplified Schmidt mode approach [33], the shapes of the BSV Schmidt modes do not depend on the parametric gain. In addition, the natural mode competition mechanism,

i.e., low-order modes acquiring larger weights at larger gain, leads to the reduction in the number of Schmidt modes with increasing gain. These two statements lead to the angular (and frequency) narrowing of the intensity distribution, which is in contradiction with the observed broadening. The broadening can be only understood in the framework of the new approach considered here, and, as shown below, is connected with the mode widths changing with the gain.

The complex function β in Eq. (12) can be written using the Schmidt decomposition with respect to the transverse wave vectors,

$$\beta(q_s, q'_i, L, \Gamma) = \sum_n \sqrt{\Lambda_n} e^{i\phi_n} u_n(q_s, \Gamma) \psi_n(q'_i, \Gamma), \quad (14)$$

where gain-dependent eigenfunctions $u_n(q_s, \Gamma)$ and $\psi_n(q'_i, \Gamma)$ for the signal and idler beams, respectively, are labeled with the index n , while Λ_n represent gain-dependent weights of the decomposition, and ϕ_n are constant phases. Similarly, the function η can be decomposed with eigenvalues $\tilde{\Lambda}_n$, constant phases φ_n , and eigenfunctions $v_n(q_s, \Gamma)$ and $\xi_n(q'_i, \Gamma)$:

$$\eta(q_s, q'_i, L, \Gamma) = \sum_n \sqrt{\tilde{\Lambda}_n} e^{i\varphi_n} v_n(q_s, \Gamma) \xi_n(q'_i, \Gamma). \quad (15)$$

From direct numerical decomposition of $\beta(q_s, q'_i, L, \Gamma)$ and $\eta(q_s, q'_i, L, \Gamma)$ the following relations between eigenfunctions are ensued: $v_n(q, \Gamma) = u_n(q, \Gamma)$, $\xi_n^*(q, \Gamma) = \psi_n(q, \Gamma)$, and the absolute values of all functions are equal: $|\psi_n| = |u_n| = |\xi_n| = |v_n|$. The gain-dependent weights Λ_n and $\tilde{\Lambda}_n$ are different in the low-gain regime ($\Lambda_n = \sinh^2(\sqrt{\lambda_n} \Gamma)$ and $\tilde{\Lambda}_n = 4 \sinh^4(\frac{\sqrt{\lambda_n} \Gamma}{2})$, where λ_n are eigenvalues of the Schmidt decomposition of the two-photon amplitude [33]) but are getting closer with increasing the gain and become equal in the high-gain regime ($\Lambda_n \approx \tilde{\Lambda}_n \sim \exp[2\sqrt{\lambda_n} \Gamma]$). This behavior of the renormalized weights is in full agreement with the gain-independent Schmidt mode approach [33]. Using the Schmidt decompositions in Eqs. (14) and (15), we can introduce new photon creation/annihilation operators for the collective spatial Schmidt modes (the Schmidt mode operators) of the radiation as a result of the nonlinear interaction,

$$\begin{aligned} A_n^\dagger &= \int dq_s \xi_n^*(q_s, \Gamma) a_s^\dagger(q_s), \\ B_n^\dagger &= \int dq_i \psi_n(q_i, \Gamma) a_i^\dagger(q_i). \end{aligned} \quad (16)$$

The operators A_n^\dagger and B_n^\dagger have the same form but they are related with the signal and idler plane-wave creation operators, respectively. Equations (12) can be written in terms of the Schmidt operators,

$$\begin{aligned} a_s(q_s, L, \omega_s) &= a_s(q_s) + \sum_n u_n(q_s, \Gamma) (\sqrt{\Lambda_n} e^{i\phi_n} A_n \\ &\quad + \sqrt{\tilde{\Lambda}_n} e^{i\phi_n} B_n^\dagger), \\ a_i^\dagger(q_i, L, \omega_i) &= a_i^\dagger(q_i) + \sum_n v_n^*(q_i, \Gamma) (\sqrt{\tilde{\Lambda}_n} e^{-i\varphi_n} B_n^\dagger \\ &\quad + \sqrt{\Lambda_n} e^{-i\varphi_n} A_n). \end{aligned} \quad (17)$$

Equations (17) clearly show that the output signal and idler plane-wave operators are connected with the same functions $u_n(q, \Gamma) = v_n(q, \Gamma)$, which is because we assumed frequency degeneracy.

The input/output relations (17) are similar to the ones of Ref. [33]. However, in Eqs. (17) not only the weights Λ_n , $\tilde{\Lambda}_n$ but also the functions $u_n(q_s, \Gamma)$, $v_n(q_i, \Gamma)$ depend on the parametric gain Γ . Thereby, the output operators are now defined by the Schmidt modes whose shapes are gain-dependent. Using Eqs. (17), the intensity distribution Eq. (13) can be written in a simple form as a sum of the squared absolute values of the Schmidt modes with the corresponding weights:

$$N_s(q_s) = \sum_n \Lambda_n |u_n(q_s, \Gamma)|^2. \quad (18)$$

The Schmidt eigenmodes and eigenvalues of the BSV can be reconstructed from the covariance of its intensity distribution [41]. Indeed, consider the sum of the contributions of the signal and idler radiation for a fixed gain, i.e., $I_\Sigma(q) = I_s(q) + I_i(q)$, the covariance of intensities measured at positions q and q' is defined as

$$\text{Cov}(q, q') = \langle I_\Sigma(q) I_\Sigma(q') \rangle - \langle I_\Sigma(q) \rangle \langle I_\Sigma(q') \rangle. \quad (19)$$

Calculation of the covariance distribution in terms of the Schmidt modes, using the input/output relations of Eqs. (17), leads to

$$\begin{aligned} \text{Cov}(q, q') &\propto \left[\sum_n \Lambda_n u_n(q) u_n^*(q') \right]^2 \\ &\quad + \left[\sum_n \Lambda_n v_n(q) v_n^*(q') \right]^2 \\ &\quad + 2 \left| \sum_n \Lambda_n u_n(q) v_n(q') \right|^2, \end{aligned} \quad (20)$$

where we suppose that $\Lambda_n = \tilde{\Lambda}_n$ for high gain. The first two terms of Eq. (20) are related to the autocorrelation of intensity fluctuations, respectively, of the signal and idler beams, while the third one represents the cross-correlation between the signal and idler radiation.

For simplifying the reconstruction of the Schmidt modes, in experiment we eliminated the cross-correlations between the signal and idler radiation by filtering a wavelength slightly shifted from the degeneracy point, so that the detected signal photons did not have idler matches. In this case, in the covariance (20) only the first term should remain, containing the signal Schmidt modes $u_n(q)$. Simultaneously, if the filtered wavelengths are still rather close to degeneracy, one can assume $u_n(q) = v_n(q)$. The Schmidt modes and weights were found by performing the singular value decomposition (SVD) of the square root of the covariance distribution [42].

In experiment, we filtered the signal radiation using a band-pass filter with the central wavelength 700 nm and a bandwidth of 10 nm. Since the length of the nonlinear crystal was small enough (2 mm), we could neglect the effect of spatial walk-off. Accordingly, the BSV radiation was axially symmetric and one could assume the factorability of the x and y degrees of freedom. Therefore the analysis was restricted

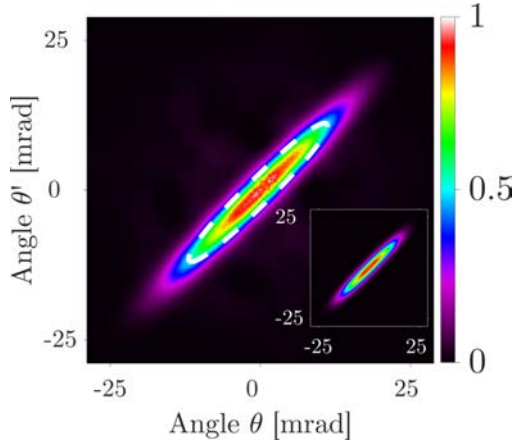


FIG. 3. Experimental distribution of the covariance in normalized units for the parametric gain $G_e = 6$. Cross-correlations are removed by using a filter selecting only the signal radiation. For comparison, the white dashed line denotes the 0.5 level of the fitted distribution, shown in the inset.

to the intensity profiles along the x direction. For a better signal-to-noise ratio, we integrated the intensity distributions in the y direction within the range from -2 to 2 mrad of the angle $q_y/|\mathbf{q}|$, where $\mathbf{q} = (q_x, q_y)$. Around 2000 single-shot intensity profiles $I(\theta)$ with $\theta = q_x/|\mathbf{q}|$ were measured, and the 2D covariance distribution $\text{Cov}(\theta, \theta')$ was calculated.

Figure 3 shows the experimental distribution of the covariance for $G_e = 6$ in normalized units. The autocorrelation part is distributed along the main diagonal, where $\theta = \theta'$. Conversely, the cross-correlation, which would lead to nonzero covariance values along the complementary diagonal $\theta = -\theta'$, is absent due to spectral filtering. In order to get rid of the background noise, a 2D fit was performed on the covariance distribution. Given the high-gain version of the intensity profile of the PDC radiation [24] and the fact that the covariance distribution along the main diagonal behaves as the squared intensity profile, the function used for the fit was

$$\text{Cov}(\theta, \theta') = A + B e^{-C(\theta - \theta')^2} \times \left[\frac{\sinh^2 \sqrt{G_e^2 - (D(\theta + \theta')^2 + E)^2}}{G_e^2 - (D(\theta + \theta')^2 + E)^2} \right]^2, \quad (21)$$

with A, B, C, D being fitting parameters and E being an experimentally determined quantity dependent on the phase mismatch. The inset of Fig. 3 demonstrates the fitted distribution for $G_e = 6$, which is indeed equivalent to the experimental one. The white dashed line in the main figure represents the half-maximum level of the fitted covariance distribution and shows a good agreement with the half-maximum level (in cyan) for the experiment.

The broadening of the covariance distribution with the increase of the parametric gain is shown in Fig. 4. The experimental FWHM follows the predicted trend from the theory for both the main and the complementary diagonals. For low gain, the theoretical dependence coincides with the covariance obtained through the first-order perturbation theory. The dependence of the main diagonal on the gain (blue solid curve

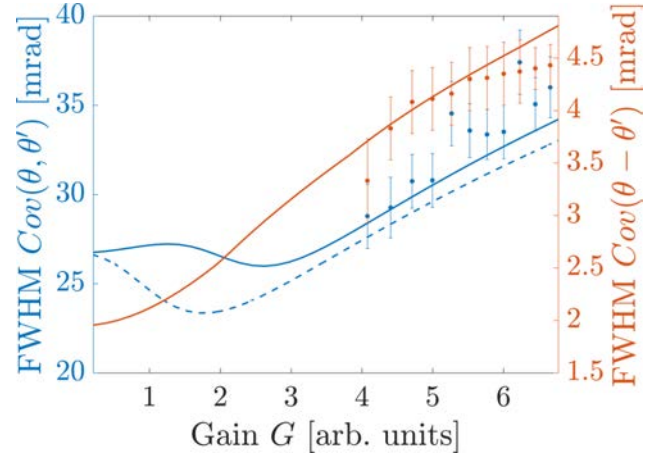


FIG. 4. Dependence of the FWHM of the covariance main (blue) and complementary (orange) diagonals on the parametric gain. (Please note the different axis scales.) The solid lines represent theoretical calculations, while the points stand for the experimental data. The dashed blue line corresponds to the main diagonal of covariance calculated under the plane-wave pump approximation [23,24].

in Fig. 4) has a minimum. This minimum is also observed in the case of a plane-wave pump (blue dashed line in Fig. 4) and qualitatively separates the low- and high-gain regimes.

The shapes and the weights of the Schmidt modes can be obtained through the SVD of the function $\sqrt{\text{Cov}(\theta, \theta')}$. This procedure has been performed for both the theoretical, Eq. (20), and the fitted experimental covariance distributions. The results of the reconstruction for different gain values are shown in Fig. 5 for the first and the second Schmidt modes. The shapes of the modes are close to the Hermite functions and their widths depend on the gain. The general tendency is the broadening of the Schmidt modes with increasing gain, this broadening being more pronounced for the higher-order modes. The theoretical results show a good agreement with the experimental data.

IV. TWO-CRYSTAL CONFIGURATION

The method described above can be extended to the two-crystal configuration, with the two crystals separated by an air gap of length d , known in the literature as the SU(1,1) interferometer [7,18,36–38]. The earlier models, for example, the gain-independent Schmidt mode approach, describe sufficiently well the BSV at the output of an SU(1,1) interferometer, including the redistribution of the mode weights and the narrowing of the spatial distribution. Qualitatively an agreement between theory and experiment is observed. Quantitatively, there is a small disagreement in the width of the spatial distribution, especially as the gain increases [33]. This disagreement is eliminated in the new model.

In the two-crystal case, one should take into account that during the free propagation in the air gap the signal, idler and pump photons acquire an additional phase. This phase creates a factor of $e^{i\Delta k' d}$ standing in front of the integral over the second crystal, where $\Delta k' = k_p^{\text{air}} - k_s^{\text{air}} - k_i^{\text{air}}$ is the wave-vector mismatch in the air [43]. Considering the problem

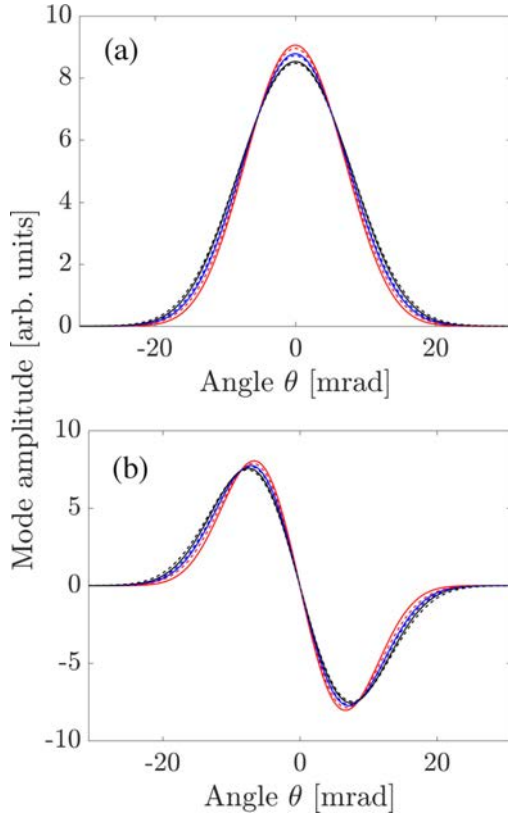


FIG. 5. (a) The first and (b) the second Schmidt modes for different parametric gain values: $G = 5.0$ (red), 5.7 (blue), and 6.6 (black). Solid lines represent theoretical calculations. Dashed lines stand for modes retrieved from the experiment.

step by step, we modify Eq. (7) by taking into account the δ function conditions in Eq. (8):

$$\begin{aligned}
 & a_s(q_s, k_{sz}, t = \tau) - a_s(q_s, k_{sz}, t = 0) \\
 &= \Gamma \int dq_i e^{-\frac{(q_s+q_i)^2 \sigma^2}{2}} \left[\int_0^L dz e^{i\Delta k z} a_i^\dagger(q_i, z, \omega_p - \omega_s) \right. \\
 & \quad \left. + e^{i\Delta k' d} \int_L^{2L} dz e^{i\Delta k z} a_i^\dagger(q_i, z, \omega_p - \omega_s) \right]. \quad (22)
 \end{aligned}$$

The boundary conditions connect the beginning and the end of the interaction in different representations: $a_s(q_s, k_{sz}, t = 0) \sim a_s(q_s, L = 0, \omega_s)$, $a_s(q_s, k_{sz}, t = \tau) \sim a_s(q_s, 2L, \omega_s)$.

Differentiation of Eq. (22) in L gives

$$\begin{aligned}
 \frac{da_s(q_s, 2L, \omega_s)}{dL} &= \Gamma \int dq_i e^{-\frac{(q_s+q_i)^2 \sigma^2}{2}} \\
 & \quad \times (e^{i\Delta k L} (1 - e^{i\Delta k' d}) a_i^\dagger(q_i, L, \omega_p - \omega_s) \\
 & \quad + 2e^{i\Delta k' d} e^{2i\Delta k L} a_i^\dagger(q_i, 2L, \omega_p - \omega_s)), \quad (23)
 \end{aligned}$$

and for the idler creation operator,

$$\begin{aligned}
 \frac{da_i^\dagger(q_i, 2L, \omega_p - \omega_s)}{dL} &= \Gamma \int dq_s e^{-\frac{(q_s+q_i)^2 \sigma^2}{2}} \\
 & \quad \times (e^{-i\Delta k L} (1 - e^{-i\Delta k' d}) a_s(q_s, L, \omega_s) \\
 & \quad + 2e^{-i\Delta k' d} e^{-2i\Delta k L} \\
 & \quad \times a_s(q_s, 2L, \omega_s)), \quad (24)
 \end{aligned}$$

where $a_i^\dagger(q_i, L, \omega_p - \omega_s)$ and $a_s(q_s, L, \omega_s)$ can be found by solving Eqs. (10) and (11) for the single crystal.

The intensity distribution in the presence of the air gap is completely different from the single-crystal case and depends on the length of the air gap. Due to the different refractive indices of the pump and BSV photons in the air, an additional phase is acquired in the gap and the intensity of light emitted in the collinear direction oscillates from minimum to maximum as d increases. Also, an increase in d leads to more and more frequent interference fringes in the intensity distribution [Fig. 6(a)].

In the experiment, we pumped two nonlinear crystals with the third harmonic of a pulsed Nd:YAG laser (repetition rate 50 Hz, wavelength 354.7 nm, and pulse duration 29.4 ps) with a FWHM diameter of approximately 0.3 mm. The two BBO crystals (3-mm thick, cut for degenerate type-I PDC) were aligned, in turn, for degenerate phase matching. A dichroic mirror and a color-glass filter suppressed the pump after the nonlinear interaction. A band-pass filter selected a 10-nm bandwidth (FWHM) of the PDC around the wavelength 710 nm. A lens brought the PDC to the momentum space, where a CMOS camera was introduced. On the camera, the background was subtracted and the data was acquired for 200 ms. The pump energy per pulse was measured before the crystals with a calibrated energy meter. The distance between the crystals was varied by changing the position of the first crystal using a translation stage. Neutral density filters were used to avoid the saturation of the camera. The ring patterns measured with the camera were then transformed into polar coordinates. To increase the accuracy, the radial profiles were obtained by averaging out the polar plots over the azimuthal angle. Due to the radial symmetry, this procedure is equivalent to fixing one of the Cartesian coordinates in theoretical calculations and calculating the intensity distribution over the other coordinate.

As the pump power increases, the parametric gain in each crystal grows (the gain after two crystals with a gap grows nonmonotonically). Figures 6(a)–6(c) shows the resulting spectra both calculated (blue) and measured (red), with the parametric gain and the pump pulse energy shown in each panel. (In the low-gain case, the measurement was not possible because of the small intensity.) Apart of a small shift in the fringes, increasing the pump power leads to the reduction of the side peaks. Therefore the envelope of the angular distribution gets narrower as the parametric gain grows, in contrast to the single-crystal case. Moreover, from Figs. 6(a)–6(c), it is clearly seen that the visibility of the interference fringes drops down with increasing pump power. Note that with stronger pumping the Kerr effect, which leads to an additional phase (mostly manifested in the collinear direction [41]), becomes more pronounced and was taken into account here.

In Figs. 6(d)–6(f), one can observe that with increasing the distance between the crystals, the total width of the angular distribution for the same pump power (or for the same gain in each crystal) is reduced, as reported in Ref. [33]. This happens due to diffraction, which leads to the reduction of the angular width of the BSV that overlaps with the pump and is amplified in the second crystal; diffraction is more pronounced for larger distances. As it was mentioned above, the second mechanism leading to the narrowing of the spatial intensity distribution

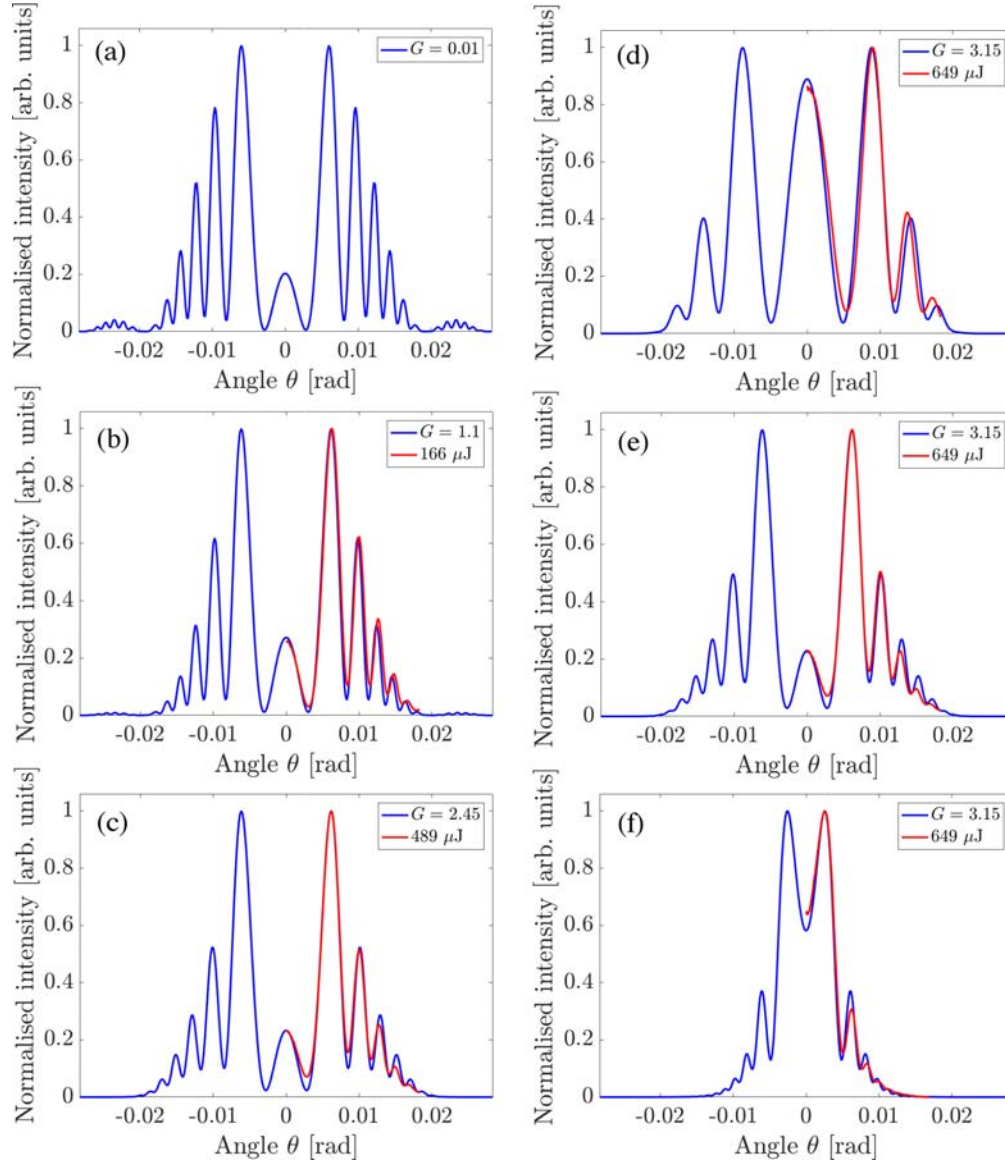


FIG. 6. The normalized intensity distributions of the BSV in the two-crystal configuration with an air gap. [(a)–(c)] The distance between the crystals is 10.66 mm, the gain in each crystal is (a) $G = 0.01$, (b) 1.1, and (c) 2.45. [(d)–(f)] The gain is fixed, $G = 3.15$, the distance between the crystals is (d) 5.58, (e) 10.66, and (f) 23.36 mm. Blue curves are theoretical calculations, red curves present the experimental data. The legends also show the values of the pump energy per pulse.

in the two-crystal configuration is the increase of the pump power (the parametric gain in each crystal). Simultaneously, these two mechanisms diminish the number of the Schmidt modes in the system, allowing one to create different shapes of intensity distributions and to control the number of modes in the BSV.

V. CONCLUSION

We have presented a new theoretical approach to describe the spatial properties of a BSV generated through high-gain PDC. In this approach, we derived and solved the integrodifferential equations for plane-wave operators without limitations on the pump waist width, number of modes and commutation of the Hamiltonian at different moments of time. The developed approach correctly captures a lot

of features of the BSV. On the one hand, it is compatible with the Schmidt mode representation. On the other hand, it properly describes the broadening of the angular distribution with increasing parametric gain. As a result, the new treatment correctly predicts the dependence of the Schmidt mode widths on the parametric gain. The model describes different experimental configurations: the single-crystal case and the configuration of two crystals with an air gap between them. For the verification of our theoretical model, we have performed several experiments, both with a single-crystal and with a two-crystal PDC sources [SU(1,1) interferometer]. The presented experimental results are in good agreement with performed theoretical calculations. Our model gives a deep insight into the properties of high-gain PDC, its mode structure and the origin of nonclassical correlations.

ACKNOWLEDGMENTS

Financial support of the Deutsche Forschungsgemeinschaft (DFG) through TRR 142, Project No. C02 is gratefully acknowledged. P.R.S. thanks the state of Nordrhein-Westfalen

for support by the *Landesprogramm für geschlechtergerechte Hochschulen*. We also acknowledge financial support of the DFG project SH 1228/3-1 and joint DFG-Russian Science Foundation (RSF) project SH 1228/2-1, ME 1916/7-1 - No.19-42-04105.

- [1] O. Jedrkiewicz, Y.-K. Jiang, E. Brambilla, A. Gatti, M. Bache, L. A. Lugiato, and P. Di Trapani, *Phys. Rev. Lett.* **93**, 243601 (2004).
- [2] M. Bondani, A. Allevi, G. Zambra, M. G. A. Paris, and A. Andreoni, *Phys. Rev. A* **76**, 013833 (2007).
- [3] G. Brida, L. Caspani, A. Gatti, M. Genovese, A. Meda, and I. R. Berchera, *Phys. Rev. Lett.* **102**, 213602 (2009).
- [4] I. N. Agafonov, M. V. Chekhova, and G. Leuchs, *Phys. Rev. A* **82**, 011801(R) (2010).
- [5] N. Corzo, A. M. Marino, K. M. Jones, and P. D. Lett, *Opt. Express* **19**, 21358 (2011).
- [6] C. K. Law, I. A. Walmsley, and J. H. Eberly, *Phys. Rev. Lett.* **84**, 5304 (2000).
- [7] A. M. Pérez, T. Sh. Iskhakov, P. Sharapova, S. Lemieux, O. V. Tikhonova, M. V. Chekhova, and G. Leuchs, *Opt. Lett.* **39**, 2403 (2014).
- [8] X. Guo, N. Liu, X. Li, and Z. Y. Ou, *Opt. Express* **23**, 29369 (2016).
- [9] T. Sh. Iskhakov, I. N. Agafonov, M. V. Chekhova, and G. Leuchs, *Phys. Rev. Lett.* **109**, 150502 (2012).
- [10] L. A. Lugiato, A. Gatti, and E. Brambilla, *J. Opt. B: Quantum Semiclass. Opt.* **4**, S176 (2002).
- [11] V. Boyer, A. M. Marino, R. C. Pooser, and P. D. Lett, *Science* **321**, 544 (2008).
- [12] V. Boyer, A. M. Marino, and P. D. Lett, *Phys. Rev. Lett.* **100**, 143601 (2008).
- [13] G. Brida, M. Genovese, and I. R. Berchera, *Nat. Photonics* **4**, 227 (2010).
- [14] A. Allevi and M. Bondani, *J. Opt.* **19**, 064001 (2017).
- [15] A. Ourjoumtsev, H. Jeong, R. Tualle-Brouiri, and P. Grangier, *Nature (London)* **448**, 784 (2007).
- [16] G. Harder, T. J. Bartley, A. E. Lita, S. W. Nam, T. Gerrits, and C. Silberhorn, *Phys. Rev. Lett.* **116**, 143601 (2016).
- [17] S. Lemieux, M. Manceau, P. R. Sharapova, O. V. Tikhonova, R. W. Boyd, G. Leuchs, and M. V. Chekhova, *Phys. Rev. Lett.* **117**, 183601 (2016).
- [18] B. Yurke, S. L. McCall, and J. R. Klauder, *Phys. Rev. A* **33**, 4033 (1986).
- [19] M. V. Chekhova and Z. Y. Ou, *Adv. Opt. Photonics* **8**, 104 (2016).
- [20] G. Brida, I. P. Degiovanni, M. Genovese, M. L. Rastello, and I. Ruo-Berchera, *Opt. Express* **18**, 20572 (2010).
- [21] M. Manceau, G. Leuchs, F. Ya. Khalili, and M. V. Chekhova, *Phys. Rev. Lett.* **119**, 223604 (2017).
- [22] M. I. Kolobov, *Rev. Mod. Phys.* **71**, 1539 (1999).
- [23] D. N. Klyshko, *Photons and Nonlinear Optics* (Gordon and Breach Science Publishers, Amsterdam, 1988).
- [24] B. Dayan, *Phys. Rev. A* **76**, 043813 (2007).
- [25] E. Brambilla, L. Caspani, O. Jedrkiewicz, L. A. Lugiato, and A. Gatti, *Phys. Rev. A* **77**, 053807 (2008).
- [26] W. Wasilewski, A. I. Lvovsky, K. Banaszek, and C. Radzewicz, *Phys. Rev. A* **73**, 063819 (2006).
- [27] A. Christ, B. Brecht, W. Mauerer, and C. Silberhorn, *New J. Phys.* **15**, 053038 (2013).
- [28] A. Eckstein, B. Brecht, and C. Silberhorn, *Opt. Express* **19**, 13770 (2011).
- [29] R. S. Bennink and R. W. Boyd, *Phys. Rev. A* **66**, 053815 (2002).
- [30] N. Quesada, G. Triginer, M. D. Vidrighin, and J. E. Sipe, *arXiv:1907.01958v2*.
- [31] N. Quesada and J. E. Sipe, *Phys. Rev. A* **90**, 063840 (2014).
- [32] N. Quesada and J. E. Sipe, *Phys. Rev. Lett.* **114**, 093903 (2015).
- [33] P. Sharapova, A. M. Pérez, O. V. Tikhonova, and M. V. Chekhova, *Phys. Rev. A* **91**, 043816 (2015).
- [34] K. Yu. Spasibko, T. Sh. Iskhakov, and M. V. Chekhova, *Opt. Express* **20**, 7507 (2012).
- [35] P. R. Sharapova, O. V. Tikhonova, S. Lemieux, R. W. Boyd, and M. V. Chekhova, *Phys. Rev. A* **97**, 053827 (2018).
- [36] F. Hudelist, J. Kong, C. Liu, J. Jing, Z. Y. Ou, and W. Zhang, *Nature Comm.* **5**, 3049 (2014).
- [37] P. Gupta, B. L. Schmittberger, B. E. Anderson, K. M. Jones, and P. D. Lett, *Opt. Express* **26**, 391 (2018).
- [38] X. Ma, C. You, S. Adhikari, E. S. Matekole, R. T. Glasser, H. Lee, and J. P. Dowling, *Opt. Express* **26**, 18492 (2018).
- [39] Y. Shaked, Y. Michael, R. Z. Vered, L. Bello, M. Rosenbluh, and A. Pe'er, *Nat. Commun.* **9**, 609 (2018).
- [40] A. V. Burlakov, M. V. Chekhova, D. N. Klyshko, S. P. Kulik, A. N. Penin, Y. H. Shih, and D. V. Strekalov, *Phys. Rev. A* **56**, 3214 (1997).
- [41] L. Beltran, G. Frascella, A. M. Pérez, R. Fickler, P. R. Sharapova, M. Manceau, O. V. Tikhonova, R. W. Boyd, G. Leuchs, and M. V. Chekhova, *J. Opt.* **19**, 044005 (2017).
- [42] M. A. Finger, N. Y. Joly, P. St. J. Russell, and M. V. Chekhova, *Phys. Rev. A* **95**, 053814 (2017).
- [43] D. N. Klyshko, *JETP* **77**, 222 (1993).

Chapter 5

Phase sensitivity of gain-unbalanced nonlinear interferometers

It is customary to compare interferometric schemes on the basis on their scaling of the phase-sensitivity with respect to n , the number of photons inside the interferometer. With the growing interest in $SU(1,1)$ interferometry, several new strategies to mitigate undesired effects, such as loss, were developed. One such strategy is to unbalance the parametric gain between the two OPAs [47]. This sparked a debate about the meaning of n , which led us to explore the effects of gain unbalancing on the performance of $SU(1,1)$ interferometers. Importantly, we discovered that comparing the phase sensitivity of $SU(1,1)$ interferometers and conventional interferometers is not straightforward. This article aims to provide a discussion about phase sensitivity in nonlinear interferometers, in different scenarios where gain unbalancing and losses are considered.

I helped lay out the general idea and develop the theory. I provided insight from an experimental perspective.

Phase sensitivity of gain-unbalanced nonlinear interferometers

Enno Giese,¹ Samuel Lemieux,¹ Mathieu Manceau,² Robert Fickler,¹ and Robert W. Boyd^{1,3}

¹*Department of Physics, University of Ottawa, 25 Templeton Street, Ottawa, Ontario K1N 6N5, Canada*

²*Max-Planck-Institute for the Science of Light, Staudtstraße 2, 91058 Erlangen, Germany*

³*Institute of Optics, University of Rochester, Rochester, New York 14627, USA*

(Received 29 September 2017; published 29 November 2017)

The phase uncertainty of an unseeded nonlinear interferometer, where the output of one nonlinear crystal is transmitted to the input of a second crystal that analyzes it, is commonly said to be below the shot-noise level but highly dependent on detection and internal loss. Unbalancing the gains of the first (source) and second (analyzer) crystals leads to a configuration that is tolerant against detection loss. However, in terms of sensitivity, there is no advantage in choosing a stronger analyzer over a stronger source, and hence the comparison to a shot-noise level is not straightforward. Internal loss breaks this symmetry and shows that it is crucial whether the source or analyzer is dominating. Based on these results, claiming a Heisenberg scaling of the sensitivity is more subtle than in a balanced setup.

DOI: [10.1103/PhysRevA.96.053863](https://doi.org/10.1103/PhysRevA.96.053863)

I. INTRODUCTION

A nonlinear interferometer (NLI), characterized by the Lie group $SU(1,1)$ and consisting of two consecutive nonlinear crystals [1], is a potential alternative to a linear interferometer seeded by a squeezed state [2] for high-precision measurements because of its supreme phase sensitivity [3]. Indeed, it is said to feature a “Heisenberg scaling” when the gains in both crystals are equal [1,4]. It has been suggested that one can suppress the influence of detection loss by using unbalanced gains in the two crystals [5,6], and in fact sub-shot-noise phase sensitivity in an unseeded NLI with this method was recently demonstrated [7].

In this article, we show that (i) the photon statistics of an unseeded and gain-unbalanced NLI lead to a suppression of the deleterious influence of detection loss, (ii) the phase sensitivity is in this case ultimately limited by the *lower* gain and is therefore symmetric with respect to the two crystals, (iii) a comparison to the shot-noise level is not straightforward, and (iv) internal loss breaks the symmetry so that a *higher* gain in the source crystal might be beneficial. Since NLIs may be intrinsically gain-unbalanced, claiming a Heisenberg scaling has to be carefully justified in each individual case.

An NLI characterized by the $SU(1,1)$ group typically consists of two nonlinear crystals *A* and *B*, as shown in Figs. 1 and 4. In the original proposal [1], crystal *A* is the *source* of the radiation, which is transmitted into crystal *B* acting as an *analyzer*. The NLI can be operated at constructive interference where both crystals generate radiation, a method that has, for example, been explored to create and tailor bright squeezed vacuum states of light [8–11]. In addition, it was shown that by seeding the NLI with a light field, the phase sensitivity is boosted even further, for both a coherent- and a squeezed-state input field [5,12,13], and the influence of internal loss may be decreased [14,15]. To focus on the physical mechanisms of an NLI, we restrict ourselves in this article to the unseeded case with vacuum input modes, which has no correspondence in a conventional interferometer.

As it is the case in other quantum physical processes with multiple nonlinear crystals, such as induced coherence [16,17], it is essential that the two crystals are pumped coherently. Nevertheless, the gains in both crystals can be controlled separately

and the relative phase of the pump field can be varied. In fact, it would be experimentally difficult to ensure that the gain of the source and the gain of the analyzer are *exactly equal*, especially since the number of photons produced scales exponentially with the electric field amplitude of the pump. Unbalanced gains give an additional degree of freedom to optimize the properties of the NLI. In this spirit, it was shown theoretically that the deleterious effects of detection loss [14] can be overcome by intentionally *unbalancing* the gains [5,6,18]. This effect was recently demonstrated experimentally [7] for the case in which the analyzer is pumped more strongly than the source. On the other hand, the significance of the analyzing crystal is questioned by proposals to operate the device in a truncated mode of operation, with only the source as a squeezer [19]. At first sight, these considerations imply an opposite role of the analyzing crystal and make it necessary to investigate the effect of gain unbalancing in more detail to understand the ultimate limit of the sensitivity of the device. A seeded and gain-unbalanced setup has been investigated in [20], but without explicit consideration of the limitations on the sensitivity.

In Sec. II we use simple transformations to derive exact analytical expressions for the detected photon number, its variance, and the phase sensitivity that can be applied to a situation with unbalanced gains, and we show the conditions under which detection loss is significant or can be overcome. In Sec. III we calculate the phase sensitivity of a gain-unbalanced NLI. The effect of internal loss breaks the symmetry between source and analyzer so that, depending on the parameters of the setup, it makes a difference which crystal is pumped more strongly, as we show in Sec. IV. Because all of these calculations focus on a degenerate NLI, we generalize in Sec. V our approach to compare the results to a nondegenerate setup, before we conclude in Sec. VI. To keep this paper self-contained, we include the detailed calculations for the degenerate NLI in Appendix A, the quantum Fisher information in a lossless and balanced setup in Appendix B, and the nondegenerate NLI in Appendix C.

II. THEORETICAL DESCRIPTION

There are two intrinsically different approaches to realize an NLI. The *degenerate* scheme employs two parametric

Hence, the phase sensitivity is modified in the presence of detection loss. In particular, it depends on the inverse Fano factor $N_d/\Delta N_d^2$, the ratio of photon number and its variance. Therefore, the photon statistics are crucial in determining the influence of detection loss. It is obvious from Eq. (5) that detection loss is suppressed if the inverse Fano factor is small. Note that a similar expression for the nondegenerate case was derived in [5,14] for the sum of the signal of the two output ports in the nondegenerate NLI. We discuss the limitations for this specific case in Sec. V. An expression for the phase sensitivity in the degenerate case for equal internal and detection loss was analyzed in [22].

Example: Balanced gain. In the original work [1] the gains in the two crystals were balanced, i.e., $V_A = V_B \equiv V$ as well as $U_A = U_B \equiv U$, and no internal loss was considered, thus setting $R_d = 0$. Hence, we find from Eq. (2) the form $N_d = 2UV(1 - \cos \phi)$. From Eq. (4) we obtain

$$\Delta \phi_d^2|_{\phi=0} = \frac{1 + 2UV(1 - \cos \phi)}{UV(1 + \cos \phi)} \Big|_{\phi=0} = \frac{1}{2UV}. \quad (6)$$

Note that $U = 1 + V$, and that V corresponds to the number of photons that are produced by crystal A and are annihilated by crystal B . Because V photons are inside the NLI and interact with a possible object, it is said that the NLI has a Heisenberg scaling of the phase sensitivity. The choice of $\phi = 0$ corresponds to the phase where the phase uncertainty $\Delta \phi_d^2$ is minimal [1]. Therefore, the NLI would be ideally operated at this point. We show in Appendix B that the quantum Fisher information is $2UV$ and, therefore, Eq. (6) saturates the quantum Cramér-Rao bound.

However, with equal gains and for this phase all photons created by the source are annihilated by the analyzer and we have $N_d|_{\phi=0} = 0$, i. e., we expect to measure no photons in the output of the NLI. This fact is particularly unfavorable because it means that vacuum fluctuations are of the same order of magnitude. Since in a realistic experiment these fluctuations are introduced by nonperfect detectors, in our treatment modeled by S_{η_d} , they significantly reduce the phase sensitivity.

The effect becomes obvious when we note that the inverse Fano factor $N_d/\Delta N_d^2 = 1/(2 + 2N_d)$ and, following Eq. (5), we arrive at

$$\frac{\Delta \phi_{\eta_d}^2}{\Delta \phi_d^2} - 1 = \frac{1 - \eta_d}{2\eta_d} \frac{1}{1 + 2UV(1 - \cos \phi)}. \quad (7)$$

To provide a quantitative analysis of the relative deviation of the phase uncertainty from the uncertainty without detection loss, we plot Eq. (7) in Fig. 2 as a function of detection loss η_d . The deviation depends on the phase, the loss, and the gain. For constructive interference ($\phi = \pi$), we see that the deviation is the smallest and even further reduced with increasing gain. At destructive interference ($\phi = 0$), we have a deviation that has a similar functional behavior, but is orders of magnitude larger than for constructive interference. Moreover, increasing the gain does not decrease the deviation (the black solid and dashed lines overlap). In fact, it can be easily seen that Eq. (7) reduces to $\Delta \phi_{\eta_d}^2 = \Delta \phi_d^2(1 + \eta_d)/(2\eta_d)$ for $\phi = 0$, in total agreement

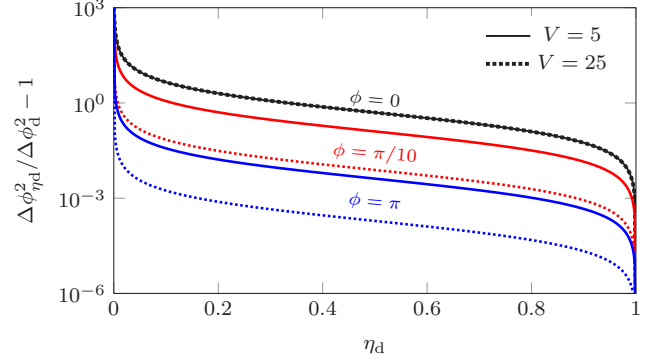


FIG. 2. Relative deviation of the phase uncertainty under the influence of detection loss η_d from the lossless case for equal gain. We show Eq. (7) for three different phases 0 , $\pi/10$, and π (black, red, and blue) for two different gain parameters $V = 5$ and 25 (solid and dashed lines). At destructive interference, the influence of detection loss is the highest and is always the same, independent of the gain.

with the expression for the phase uncertainty of the sum of the two output ports in the nondegenerate NLI discussed in [5,14]. If we were not to operate this NLI at or close to destructive interference, we could get a significant number of photons exiting the device and therefore suppress the influence of the detection loss. However, the minimal phase uncertainty occurs exactly at vanishing ϕ and with it at vanishing N_d , and only in this case do we obtain the unique Heisenberg scaling of the uncertainty.

As this example demonstrates, the effect of detection loss in an unseeded NLI is governed by the intensity $N_d(\phi)$ in the output of the interferometer. Since we are mainly interested in the phase where its uncertainty is minimal, we do not have the flexibility to operate the interferometer at a different phase, e.g., at constructive interference where $N_d(\phi)$ is maximal. However, there is a different option for increasing $N_d(\phi)$, namely, using different gain values for the two crystals, that is, unbalancing the gains. If, for example, the source is stronger than the analyzer, all the photons created in crystal A can never be annihilated in crystal B , even if the interferometer is set to destructive interference. In the opposite case in which the analyzer is weaker than the source, crystal B not only annihilates all photons emerging from crystal A , but overcompensates and creates additional photons. Therefore, the larger the gain difference, the higher the intensity in the output of the interferometer and the smaller the impact of detection loss. Hence, we expect a suppression of detection loss for a gain-unbalanced setup [5–7].

III. PHASE SENSITIVITY FOR UNBALANCED GAIN

In the section above, we established that unbalancing the gain can be beneficial if there is significant detection loss in the NLI. However, even though the impact of detection loss is reduced, the effect of unbalanced gain on the phase uncertainty itself has not been studied yet. In this section, we derive the minimal phase uncertainty for vanishing internal loss $R_d = 0$.

For that, we minimize Eq. (4) for arbitrary gains and find that the minimum uncertainty occurs at the phase

$$\phi_{\min} = \pm \arctan \sqrt{\frac{V_{\max} U_{\max} - V_{\min} U_{\min}}{(U_{\max} + V_{\max})^2 V_{\min} U_{\min}}}, \quad (8)$$

which leads with Eq. (2) to the number of photons

$$N_d(\phi_{\min}) = \frac{V_{\max} - V_{\min}}{U_{\min} + V_{\min}}. \quad (9)$$

Here, we defined $V_{\min} = \min[V_A, V_B]$ and $V_{\max} = \max[V_A, V_B]$ as the smaller and the larger parameter, respectively. The parameters U_{\min} and U_{\max} are defined in an analogous way. Moreover, we see that $N_d(\phi_{\min}) \gg 1$ if $V_{\min} \ll V_{\max}$. In this case, detection loss has practically no impact on the phase uncertainty, which one can directly see from Eq. (5). Note further that for $V_A \neq V_B$, the optimal sensitivity is achieved if the NLI is not operated at destructive interference $\phi_{\min} \neq 0$.

With the phase from Eq. (8) we find that the minimal phase uncertainty takes the form

$$\Delta\phi_d^2(\phi_{\min}) = \frac{1}{2U_{\min}V_{\min}}. \quad (10)$$

Hence, the phase sensitivity is limited by the crystal with *smaller* gain, independent on whether it is crystal *A* or *B*. In the numerical analysis of [5] it was implicitly seen that the smaller gain limits the sensitivity, but this fact was not commented upon further.

Quantum limitations. The attention that NLIs have attracted is due to the scaling behavior of their phase uncertainty, which is often referred to as the “Heisenberg scaling.” Indeed, we saw from Eq. (6) in a gain-balanced NLI with $V_A = V_B = V \gg 1$ that $\Delta\phi_d(0) \cong 1/(\sqrt{2}V)$. Since V corresponds to the number of photons produced by the source, the connection to the Heisenberg scaling is evident. However, a disadvantage of a gain-balanced NLI is that it is very susceptible to detection loss.

In an unbalanced setup at high gain, we find from Eq. (10) that $\Delta\phi_d(\phi_{\min}) \cong 1/(\sqrt{2}V_{\min})$, where V_{\min} is the smaller gain parameter. If the source is weaker than the analyzer ($V_A < V_B$), the sensitivity is limited by V_A and therefore by the number of photons that interact with the object. A comparison to the shot-noise level of this photon number seems obvious and the phase sensitivity indeed displays a Heisenberg scaling. Such phase measurements below the shot-noise level determined by V_A have recently been performed using direct detection [7].

If the analyzer is weaker than the source ($V_B < V_A$), the sensitivity is limited by V_B , which is completely independent of how many photons interacted with the object or were inside the NLI, described by V_A . However, it is V_A that is conventionally used [5] to determine a shot noise or Heisenberg scaling behavior. In this case, the comparison would be somewhat artificial because the sensitivity is not limited by this number.

Of course, if the sample in the interferometer is very sensitive and gets easily destroyed by high intensities or if radiation pressure on mirrors degrades the sensitivity, one would always operate the NLI with the smaller number of

photons inside and naturally choose $V_A < V_B$ so that the analyzer is stronger. But, if there is no limitation on how many photons might interact with an object inside the NLI, there is no preference as to which of the two gains should be the lower one because the resulting sensitivity is exactly the same. The interferometer is completely symmetric and the only limiting factor is the crystal with smaller gain, independent of which crystal it is. Hence, a comparison to a Heisenberg limit is not straightforward and has to be justified in each case, let alone the fact that the pump is assumed to be undepleted. In fact, other variations of an NLI give a phase sensitivity that scales with the shot-noise level of pump photons [23].

In conclusion, the second crystal has to be considered an essential part of the interferometer. Of course, it is valid to employ truncated schemes [19] if the output of an NLI is detected by homodyne detection [26], but the original proposal [1] only involves a much simpler direct detection scheme [4,7], in which the analyzing crystal is vital. On the same note, the quantum Fisher information and the quantum Cramér-Rao bound do not specify a particular detection scheme and are usually calculated for the state inside the interferometer [5,18,19,27]. Because the analyzer is seen as a part of the detection, the bound is independent of the gain of crystal *B* and since one optimizes over all possible detection schemes, it is implicitly assumed that this gain can be arbitrarily high. On the other hand, if one sees crystal *B* as an integral component of the interferometer, one cannot just optimize over all possible parameters but is restricted by the experimental limitations.

IV. BREAKING THE SYMMETRY THROUGH INTERNAL LOSS

In the previous section, we pointed out that the phase sensitivity is limited by the lower gain, and therefore is completely symmetric with respect to the source and analyzer. If we introduce internal loss, this symmetry is broken.

It is straightforward to see that including internal loss, i.e., a beam splitter S_d with $T_d < 1$ in-between the two crystals as shown in Fig. 1, affects solely the photons created in crystal *A* and only indirectly through a modified input the action of crystal *B*. This fact stands out most clearly by observing that in both Eqs. (2) and (3) the quantity V_A always appears together with the transmittance T_d . For simplicity, we introduce the notation $V_t \equiv T_d V_A$, which describes the number of photons that are transmitted from crystal *A* to crystal *B*. In agreement with the previous notation, we also use $U_t \equiv 1 + V_t$. In the following, we first give an intuitive explanation of the influence of internal loss on the sensitivity, before turning to the exact results.

If internal loss is small, we can neglect the term $-R_d T_d V_A$ in Eq. (3) for the variance. Moreover, if operated at high gain, $V_t \gg 1$, the photon number as described in Eq. (2) takes the form

$$N_d(\phi) \cong V_t + V_B + 2V_t V_B - 2\sqrt{U_t U_B V_t V_B} \cos \phi \quad (11)$$

and therefore we arrive at the same result as in Eq. (10) for the minimal phase uncertainty, with only V_A replaced by V_t . In fact, an expansion of the exact treatment given below in orders of R_d gives rise, up to lowest order, to the

phase uncertainty $\Delta\phi^2 \cong 1/(2U_{\min}V_{\min})$, where now $V_{\min} = \min[V_t, V_B]$ and $V_{\max} = \max[V_t, V_B]$. Because V_t depends on T_d , the phase uncertainty is independent of the transmittance only if $V_B < V_t$. Thus, if internal loss dominates, it is better to have a stronger source than analyzer, the opposite case of what was used in [5–7].

$$N_{d,\min} = \frac{2(V_B - V_t)^2 + \mathcal{L} + \sqrt{4(V_B - V_t)^2(U_B + V_t)^2 + 4U_B V_B \mathcal{L} + R_d V_t [2U_B V_B - U_t V_t] + \mathcal{L}^2}}{2(U_B + V_B)(U_t + V_t)}, \quad (12)$$

where we defined a loss-dependent term $\mathcal{L} \equiv R_d V_t (1 + 8U_B V_B)$. With this analytic expression we are able to determine the variance $\Delta N_{d,\min}^2 = 2N_{d,\min}(1 + N_{d,\min}) - R_d V_t$ from Eq. (3). The inverse Fano factor $N_{d,\min}/\Delta N_{d,\min}^2$ that suppresses the effect of detection loss according to Eq. (5) can be calculated for different parameters. We plot this factor in Fig. 3(a) on a logarithmic scale. For $R_d = 0$ unbalancing the gains decreases the influence of detection loss significantly: the dotted line describing the balanced configuration is much higher than the red and blue solid lines with a stronger analyzer and source, respectively. However, the number of photons transmitted to crystal B, $V_t = (1 - R_d)V_A$, decreases for $R_d > 0$ and for an initially balanced situation we arrive effectively at a gain-unbalanced setup with $V_t < V_B$. Hence, the dotted line decreases rapidly until it is very close to the case of a stronger analyzer (blue line).

For the same reason, a stronger source at first slightly increases the inverse Fano factor because the unbalancing is effectively lowered, making detection loss more significant again. On the other hand, for a stronger analyzer we see a decrease of the inverse Fano factor, because due to internal loss the gain unbalancing effectively increases and we have $V_t < V_A < V_B$. Hence, detection loss is further suppressed and in this sense the setup improves. The plot also demonstrates that it is better to have a stronger analyzer to suppress the effect of detection loss in the presence of internal loss, which is the configuration that was investigated in [5–7]. Note further that only for $R_d \cong 0$ we see that there is a significant advantage of gain unbalancing and in this case it does not matter much which one of the crystals has higher gain.

After considering the inverse Fano factor $N_d/\Delta N_d^2$ that suppresses detection loss, we now turn to the minimal phase uncertainty itself. We find the analytical expression

$$\Delta\phi_{d,\min}^2 = [N_{d,\min}(U_B + V_B)(U_t + V_t) + U_B V_t + U_t V_B - R_d V_t][4U_B V_B(U_t - R_d)V_t]^{-1} \quad (13)$$

for the phase uncertainty without detection loss and plot it in Fig. 3(b). Here, the effect of internal loss is exactly opposite to the one on detection loss: for an unbalanced situation, the phase sensitivity is always better if the source is stronger (red solid line), compared to the case where the analyzer is stronger (blue solid line). This can be intuitively understood considering that internal loss can affect the output of crystal A directly and the action of crystal B only indirectly by modifying its input.

However, for a more accurate description of the NLI we derive from (4) an expression for the phase where its uncertainty is minimized. We can perform this calculation analytically, but the expressions are rather cumbersome and we therefore refrain from presenting them. When we use this phase in Eq. (2) to calculate the photon number, we find

Hence, it is beneficial to have a stronger source so that the reduced number of photons in the interferometer is still large enough to not limit the sensitivity.

Not surprisingly, for equal gain (using the higher of the two gains for both crystals) always outperforms the unbalanced

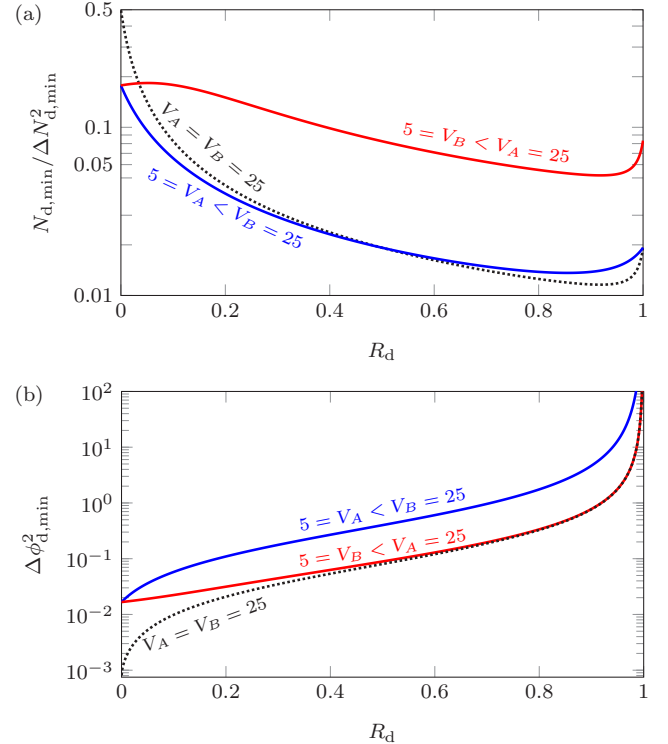


FIG. 3. Effect of internal loss R_d on $N_{d,\min}/\Delta N_{d,\min}^2$ in (a) and on $\Delta\phi_{d,\min}^2$ in (b). In (a) we demonstrate that the inverse Fano factor $N_d/\Delta N_d^2$ decreases rapidly for the gain-balanced situation (dotted line) because internal loss deteriorates the number of transmitted photons V_t . Therefore, the gain of crystal A is effectively lower and detection loss is suppressed. The same is true if the analyzer is stronger than the source (blue solid line) and the advantage of unbalancing the gain decreases. If the source is stronger (red solid line), the inverse Fano factor increases slightly at first. Moreover, it is always larger than for the opposite case. In (b) we show that the phase uncertainty (without detection loss) is the smallest for a gain-balanced setup (dotted line). For large loss R_d , the case of a stronger source (red line) is very close to the gain-balanced result. Moreover, for an unbalanced setup it is always beneficial to work with a stronger source than with a stronger analyzer (blue line).

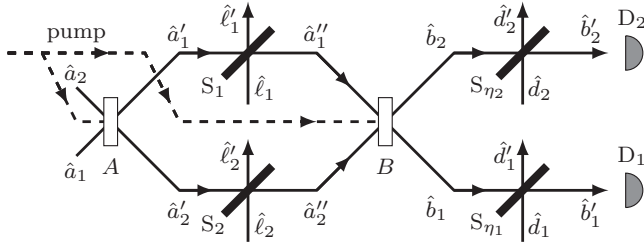


FIG. 4. Schematic of a nondegenerate nonlinear interferometer consisting of two coherently pumped nonlinear crystals A and B . Internal loss is modeled by a beam splitter $S_{1,2}$ in each arm, detection loss by a beam splitter $S_{\eta_{1,2}}$ in front of each detector $D_{1,2}$.

setup. However, for sufficiently large loss, the balanced situation is very close to the case of a stronger source.

Since in a gain-unbalanced setup with internal loss a stronger analyzer suppresses the effect of detection loss, whereas a stronger source in addition reduces the influence of internal loss, the latter one seems at first sight advantageous. However, a stronger source suppresses detection loss not as well as a stronger analyzer and is only beneficial for small internal loss when compared to the balanced setup. Therefore, the decision which crystal to pump stronger has to be made based on the order of magnitude of the internal and detection losses. In each individual case, it might be beneficial to have stronger source or a stronger analyzer.

V. COMPARISON OF DEGENERATE AND NONDEGENERATE CONFIGURATION

So far we have only considered a degenerate setup. However, we generalize our results to the case of a nondegenerate NLI (see Appendix C) and compare them in this section to the degenerate ones obtained above. The setup is shown in Fig. 4, where we now have different input and output modes 1 and 2. Even though the expressions for the photon number and variance are different from the degenerate configuration, they

are similar enough so that our previous discussion can also be applied, with some limitations, to the nondegenerate case.

The photon number detected by detector D_j in a nondegenerate as well as a degenerate configuration takes the form

$$N_{\eta j} = \eta_j N_j = \eta_j (\mathcal{A}_j - \mathcal{K}_j \cos \phi), \quad (14)$$

where \mathcal{A}_j is the amplitude and \mathcal{K}_j the contrast of the signal and the index $j = d, 1, 2$. Here, η_j is the efficiency of the detector j modeled by a beam splitter $S_{\eta j}$ and T_j the transmittance of the beam splitter S_j between the two crystals. R_j is the corresponding reflectivity. The explicit form of \mathcal{A}_j and \mathcal{K}_j is summarized in Table I for all cases. The internal loss in each arm of the NLI may be different and has an effect on the signal and variance [28]. Note that ϕ is defined slightly different from the degenerate case to account for the different phases in the two branches of the NLI.

In the nondegenerate setup one can, in addition to considering both exit ports separately, analyze the sum of the two signals [1]. Without detection loss, we therefore define the sum of the two signals $N_+ \equiv N_1 + N_2$. Ultimately, we are interested in the phase uncertainty $\Delta \phi_j^2$ which can be analogously defined to Eq. (4) where we replace the index d by $j = 1, 2, +$. To obtain the phase uncertainty, we first need the variance of the photon number.

We display in the table the variances $\Delta N_{\eta j}^2$ and ΔN_j^2 with and without detection loss, respectively, and note that only for $j = d, 1, 2$ the relation

$$\Delta N_{\eta j}^2 = \eta_j^2 \Delta N_j^2 + \eta_j (1 - \eta_j) N_j \quad (15)$$

holds, but not for the sum of the two signals. Therefore, the suppression of the detection loss for phase sensitivity of the signal sum is not as straightforward. However, if $\eta_1 = \eta_2 \equiv \eta_+$, we also find Eq. (15) for $j = +$ as predicted by [14]. In analogy to Appendix A we arrive at

$$\Delta \phi_{\eta j}^2 = \Delta \phi_j^2 \left(1 + \frac{1 - \eta_j}{\eta_j} \frac{N_j}{\Delta N_j^2} \right) \quad (16)$$

TABLE I. Comparison of degenerate and nondegenerate NLI. The index d denotes the degenerate case, 1 and 2 the two output ports of the nondegenerate case, and $+$ their sum. The signal without detection loss has an amplitude \mathcal{A}_j and a contrast \mathcal{K}_j . The variance of the detected signal is $\Delta N_{\eta j}^2$. In the second part of the table, we show the variance ΔN_j^2 without detection loss and later the same quantity for vanishing internal loss. The factor in the second column shows the influence of detection loss in a balanced situation. The optimal phase uncertainty $\Delta \phi_j^2(\phi_{\min})$ was calculated for the lossless case.

j	\mathcal{A}_j	\mathcal{K}_j	$\Delta N_{\eta j}^2$	
d	$T_d V_A + V_B + 2T_d V_A V_B$	$2T_d \sqrt{U_A U_B V_A V_B}$	$\eta_d N_d (1 + \eta_d + 2\eta_d N_d) - \eta_d^2 R_d T_d V_A$	
1	$T_1 V_A + V_B + (T_1 + T_2) V_A V_B$	$2\sqrt{T_1 T_2 U_A U_B V_A V_B}$	$\eta_1 N_1 (1 + \eta_1 N_1)$	
2	$T_2 V_A + V_B + (T_1 + T_2) V_A V_B$	$2\sqrt{T_1 T_2 U_A U_B V_A V_B}$	$\eta_2 N_2 (1 + \eta_2 N_2)$	
$+$	$\mathcal{A}_1 + \mathcal{A}_2$	$4\sqrt{T_1 T_2 U_A U_B V_A V_B}$	$(\eta_1 N_1 + \eta_2 N_2)(1 + \eta_1 N_1 + \eta_1 N_2)$ $+ \eta_1 \eta_2 (N_1 + N_2) - \eta_1 \eta_2 (T_1 + T_2 - 2T_1 T_2) V_A$	
j	ΔN_j^2	$1 + \frac{1 - \eta_j}{\eta_j} \frac{N_j}{\Delta N_j^2} \Big _{\phi=0}$	ΔN_j^2 with $T_j = 1$	$\Delta \phi_j^2(\phi_{\min})$
d	$2N_d(1 + N_d) - R_d T_d V_A$	$(1 + \eta_d)/(2\eta_d)$	$2N_d(1 + N_d)$	$1/(2U_{\min} V_{\min})$
1	$N_1(1 + N_1)$	$1/\eta_1$	$N_d(1 + N_d)$	$1/(4U_{\min} V_{\min})$
2	$N_2(1 + N_2)$	$1/\eta_2$	$N_d(1 + N_d)$	$1/(4U_{\min} V_{\min})$
$+$	$N_+(2 + N_+) + [2T_1 T_2 - (T_1 + T_2)] V_A$	$(1 + \eta_+)/(2\eta_+)$	$4N_d(1 + N_d)$	$1/(4U_{\min} V_{\min})$

and thus that the inverse Fano factor $N_j/\Delta N_j^2$ determines the suppression of detection loss with $j = d, 1, 2, +$. In fact, for a gain-unbalanced scheme and vanishing internal loss we find for the expression in parentheses the factor shown in Table I in agreement with [14]. Note that if only one single exit port is detected in the nondegenerate setup, we find a significantly different dependence on detection loss. We also see that gain unbalancing suppresses detection loss in the nondegenerate setup, even though for the sum of the two signals and $\eta_1 \neq \eta_2$ the treatment is more subtle.

If the internal loss in each arm is equal, i.e., $T_1 = T_2 = T_d$, we find $N_1 = N_2 = N_d$ and $N_+ = 2N_d$. Moreover, if we assume the lossless case with $T_j = 1$, we can express all variances simply by the number of photons in one exit port N_d (see the third column in the lower part of Table I). Since all of these results differ only by a factor from the degenerate result, we can use the phase from Eq. (8) to obtain the minimal uncertainty. These results are shown in the table as well. We note that the phase uncertainty is smaller by a factor of 2 in the nondegenerate case, regardless of using only one detector or both. In particular, we obtain again that the sensitivity is limited by $V_{\min} = \min[V_A, V_B]$. Hence, we see that the discussion from above similarly applies to the different cases of a nondegenerate setup. This is also true if we include internal loss in analogy to Sec. IV, even though there are more parameters since there might be different loss in each arm of the NLI. We therefore refrain from presenting a lengthy discussion of all different cases.

Finally, to compare the sensitivity to the shot-noise level in a nondegenerate setup, one has to remember that V_A is the number of photons per mode produced by crystal A. Therefore, the number of photons inside the NLI is $n_+ = 2V_A$, whereas in the degenerate case it was $n_d = V_A$. Hence, the shot-noise level could be defined as $1/\sqrt{2V_A}$ in contrast to the degenerate NLI, where it is $1/\sqrt{V_A}$. In case of a stronger analyzer, we have $\Delta\phi_{d,\min} \cong 1/(\sqrt{2V_A}) = 1/(\sqrt{2}n_d)$ and $\Delta\phi_{+,\min} \cong 1/(2V_A) = 1/n_+$. In absolute values, $\Delta\phi_{+,\min} < \Delta\phi_{d,\min}$. However, if we assume the same number of photons inside the interferometer, that is, $n_d = n_+$, we find $\Delta\phi_{d,\min} = \Delta\phi_{+,\min}/\sqrt{2}$ in contrast to our previous statement.

VI. CONCLUSIONS

We have demonstrated that the sensitivity of a degenerate NLI is limited by the crystal with the smaller gain, whether it is the source or analyzer crystal. Hence, the second crystal has to be considered an essential part of the interferometer and its gain is equally important as the one of the source in a setup without internal loss. Moreover, the sensitivity might not scale at all with the number of photons produced by the source. We emphasize that a comparison to the shot-noise or Heisenberg limit is only suggestive if the gain of the source is the limiting factor. If the analyzer is limiting the sensitivity, a comparison to the shot-noise level and a discussion of a ‘‘Heisenberg scaling’’ seems rather artificial. Together with the discussion of [23], we therefore hope to raise awareness for the subtleties of claiming a Heisenberg scaling.

In order to suppress the effect of detection loss, it might be beneficial to unbalance the gains of the two crystals on

purpose. Indeed, we showed that detection loss is suppressed by the inverse Fano factor of the photon statistics. For a gain-balanced NLI, the optimal phase occurs for a vacuum output state and the sensitivity is susceptible to detection loss. In contrast, unbalancing the gains leads to a significant photon number in the output that suppresses it.

Whereas for this suppression it is irrelevant whether the source or the analyzer is stronger (the NLI is symmetric in this sense), it changes dramatically when internal loss is considered. Internal loss effectively changes the gain of the source and therefore may increase or decrease the suppression of detection loss. In addition, this broken symmetry between the two nonlinear crystals has the consequence that a higher gain in the source reduces the effect of internal loss on the phase sensitivity.

To suppress negative effects of internal loss, a stronger source should be used; to additionally suppress detection loss, a stronger analyzer seems beneficial. In fact, a stronger source with internal loss suppresses detection loss, but not as well as a stronger analyzer. Hence, the decision on whether to use a higher gain for the source or for the analyzer has to be based on the magnitude of internal and detection losses for each individual case. We emphasize that these results are valid for a degenerate NLI, but most of them carry over to the nondegenerate case, for which we provide analytical expressions as well.

ACKNOWLEDGMENTS

This research was performed as part of a collaboration within the Max Planck-uOttawa Centre for Extreme and Quantum Photonics, whose financial support we gratefully acknowledge. We thank M. V. Chekhova for valuable comments and discussions. E.G., S.L., R.F., and R.W.B. are thankful for the financial support by the Canada Excellence Research Chairs program (CERC) and the Natural Sciences and Engineering Research Council of Canada (NSERC). R.F. acknowledges the financial support of the Banting postdoctoral fellowship of the NSERC and S.L. the financial support from Le Fonds de Recherche du Québec Nature et Technologies (FRQNT). E.G. is grateful to the Friedrich-Alexander-Universität Erlangen-Nürnberg for an Eugen Lommel stipend.

APPENDIX A: DEGENERATE CONFIGURATION

In this Appendix, we use the notation according to Fig. 1, where the input mode of the degenerate NLI is denoted by the operator \hat{a} . It describes, as its subsequent counterparts, a photonic annihilation operator and fulfills the bosonic commutation relation $[\hat{a}, \hat{a}^\dagger] = 1$. The input enters at first crystal A, and its output \hat{a}' is described by the Bogoliubov transformation

$$\hat{a}' = u_A \hat{a} + v_A \hat{a}^\dagger. \quad (\text{A1})$$

Here, u_A and v_A are complex parameters. They describe the amplification process and fulfill the relation $1 = |u_A|^2 - |v_A|^2 = U_A - V_A$. Due to this identity, we can identify U_A and V_A with respective hyperbolic functions, that is $U_A = \cosh^2 r_A$ and $V_A = \sinh^2 r_A$, where we introduced the so-called squeezing parameter or gain r_A of crystal A.

The internal loss of the NLI is modeled by a beam splitter S_d , which is described by the transformation

$$\hat{a}'' = t_d \hat{a}' + r_d \hat{\ell} \quad \text{and} \quad \hat{\ell}' = t_d^* \hat{\ell} - r_d^* \hat{a}', \quad (\text{A2})$$

where $\hat{\ell}$ is the operator associated with the noise input of the beam splitter according to Fig. 1 and causes vacuum noise. We displayed also the transformation for the output $\hat{\ell}'$ to show that t_d and r_d may be chosen complex and there is in addition a phase shift. The asterisk (*) denotes the complex conjugate. Note that t_d and r_d describe the field transmittance and reflectivity, respectively. They fulfill $1 = |r_d|^2 + |t_d|^2 \equiv R_d + T_d$. Choosing complex t_d and r_d makes it possible to absorb phases of input modes into their definition. We therefore do not have to treat phases accumulated inside the NLI separately. With the relation (A1) for crystal A we find

$$\hat{a}'' = t_d u_A \hat{a} + t_d v_A \hat{a}^\dagger + r_d \hat{\ell}. \quad (\text{A3})$$

The action of crystal B is again described by a Bogoliubov transformation

$$\hat{b} = u_B \hat{a}'' + v_B \hat{a}''^\dagger \quad (\text{A4})$$

with the same assumptions and notations for the coefficients u_B and v_B as for crystal A. With the help of Eq. (A3) we find

$$\begin{aligned} \hat{b} = & (t_d u_A u_B + t_d^* v_A^* v_B) \hat{a} + (t_d v_A u_B + t_d^* u_A^* v_B) \hat{a}^\dagger \\ & + r_d u_B \hat{\ell} + r_d^* v_B \hat{\ell}^\dagger. \end{aligned} \quad (\text{A5})$$

Detection loss is modeled by the transformation

$$\hat{b}' = \sqrt{\eta_d} \hat{b} + \sqrt{1 - \eta_d} \hat{d}, \quad (\text{A6})$$

which corresponds to a beam splitter S_{η_d} in front of the detector. Here, η_d is the detection efficiency.

Let us assume that there is vacuum input in mode \hat{d} . We then find

$$\hat{b}'^\dagger \hat{b}' |0_d\rangle = \eta_d \hat{b}^\dagger \hat{b} |0_d\rangle + \sqrt{\eta_d(1 - \eta_d)} \hat{b} |1_d\rangle \quad (\text{A7})$$

and obtain, projecting with $\langle 0_d |$ onto Eq. (A7),

$$\langle 0_d | \hat{b}'^\dagger \hat{b}' |0_d\rangle = \eta_d \hat{b}^\dagger \hat{b} \quad (\text{A8a})$$

and

$$\langle 0_d | (\hat{b}'^\dagger \hat{b}')^2 |0_d\rangle = \eta_d^2 (\hat{b}^\dagger \hat{b})^2 + \eta_d(1 - \eta_d) \hat{b}^\dagger \hat{b} \quad (\text{A8b})$$

when we take the modulus square of Eq. (A7). The expectation value of Eq. (A8) for an arbitrary input state in the other modes directly leads to

$$N_{\eta_d} = \eta_d N_d \quad (\text{A9a})$$

and

$$\Delta N_{\eta_d}^2 = \eta_d^2 \Delta N_d^2 + \eta_d(1 - \eta_d) N_d, \quad (\text{A9b})$$

where N_{η_d} and $\Delta N_{\eta_d}^2$ are the photon number and variance detected by D_d , and N_d and ΔN_d^2 the photon number and variance without detection loss. With Eq. (A9) we find for the phase sensitivity $\Delta \phi_{\eta_d}^2 \equiv \Delta N_{\eta_d}^2 / \left| \frac{\partial N_{\eta_d}}{\partial \phi} \right|^2$ including detection

loss the expression

$$\Delta \phi_{\eta_d}^2 = \Delta N_d^2 / \left| \frac{\partial N_d}{\partial \phi} \right|^2 \times \left(1 + \frac{1 - \eta_d}{\eta_d} \frac{N_d}{\Delta N_d^2} \right). \quad (\text{A10})$$

The above expressions are so far general for generic input in modes \hat{a} and $\hat{\ell}$. But, now we make the assumption that we have a vacuum input in all modes. When we rewrite Eq. (A5) as $\hat{b} \equiv A_d \hat{a} + \alpha_d \hat{a}^\dagger + B_d \hat{\ell} + \beta_d \hat{\ell}^\dagger$ and introduce the complex coefficients

$$\begin{aligned} A_d &= t_d u_A u_B + t_d^* v_A^* v_B, & B_d &= r_d u_B, \\ \alpha_d &= t_d v_A u_B + t_d^* u_A^* v_B & \text{and} & \beta_d = r_d^* v_B, \end{aligned} \quad (\text{A11})$$

we see that $\hat{b}|0\rangle = \alpha_d |1_a\rangle + \beta_d |1_\ell\rangle$ and find for the state $|\psi_d\rangle \equiv \hat{b}^\dagger \hat{b} |0\rangle$ the expression

$$\begin{aligned} |\psi_d\rangle = & (|\alpha_d|^2 + |\beta_d|^2) |0\rangle + \sqrt{2} A_d^* \alpha_d |2_a\rangle \\ & + (B_d^* \alpha_d + A_d^* \beta_d) |1_a, 1_\ell\rangle + \sqrt{2} B_d^* \beta_d |2_\ell\rangle. \end{aligned} \quad (\text{A12})$$

Hence, the vacuum expectation value $N_d \equiv \langle 0 | \psi_d \rangle = |\alpha_d|^2 + |\beta_d|^2$ takes with Eq. (A11) the form

$$N_d = T_d V_A + V_B + 2 T_d V_A V_B - 2 T \sqrt{U_A V_A U_B V_B} \cos \phi, \quad (\text{A13})$$

where we used $R_d + T_d = 1$, $U_j = 1 + V_j$, and introduced the phase

$$\phi \equiv \arg(u_A v_A u_B v_B^* t_d^2) + \pi. \quad (\text{A14})$$

Note that the definition of the phase includes a shift by π so that $\phi = 0$ describes the dark fringe. The variance can be calculated through $\Delta N_d^2 = \langle \psi_d | \psi_d \rangle - N_d^2$ and we find after some algebra

$$\Delta N_d^2 = 2 N_d (1 + N_d) - R_d T_d V_A. \quad (\text{A15})$$

APPENDIX B: QUANTUM FISHER INFORMATION

In this Appendix, we calculate the quantum Fisher information for a degenerate NLI with vacuum input and equal gain in both crystals. For a more convenient description, we use the Bogoliubov transformation from Eq. (A1) with $u_A = u_B = u$ and $v_A = v_B = v$ to write the squeezed photon operator $\hat{a}' = \hat{S}^\dagger \hat{a} \hat{S}$, where we introduced the squeezing operator \hat{S} . If the gain is equal in both crystals and no loss is present, the final state at the output of the NLI is a pure state which can be written as a sequence of squeezing, phase evolution, and antisqueezing. Hence, it takes the form

$$|\psi_f\rangle = \hat{S}^\dagger \exp\left(i \frac{\phi}{2} \hat{a}^\dagger \hat{a}\right) \hat{S} |0\rangle = \exp\left(i \frac{\phi}{2} \hat{a}'^\dagger \hat{a}'\right) |0\rangle. \quad (\text{B1})$$

With the notation $\hat{n}' \equiv \hat{a}'^\dagger \hat{a}'$, the derivative of the final state with respect to ϕ can be written as $|\psi_f'\rangle = \hat{n}' |\psi_f\rangle / 2$.

For a pure state, the quantum Fisher information [25] of the NLI can be written as

$$F_\phi = 4(\langle \psi_f' | \psi_f' \rangle - \langle \psi_f' | \psi_f \rangle^2) = \langle \hat{n}'^2 \rangle - \langle \hat{n}' \rangle^2, \quad (\text{B2})$$

where the expectation values are taken with respect to the initial state, i.e., $|0\rangle$ in our case. With the help of Eq. (A1) we

find the relation

$$\hat{n}'|0\rangle = V|0\rangle + \sqrt{2}u^*v|2\rangle, \quad (\text{B3})$$

and, by projecting this state on itself and on $|0\rangle$ we find the variance of \hat{n}' and therefore show that the quantum Fisher information can be written as

$$F_\phi = 2UV. \quad (\text{B4})$$

APPENDIX C: NONDEGENERATE CONFIGURATION

In contrast to the degenerate case, we have for a nondegenerate setup two input modes, namely, modes 1 and 2, which are described by the bosonic annihilation operators \hat{a}_1 and \hat{a}_2 , according to Fig. 4. Crystal A is described by the Bogoliubov transformation

$$\hat{a}'_1 = u_A \hat{a}_1 + v_A \hat{a}_2^\dagger \quad \text{and} \quad \hat{a}'_2 = u_A \hat{a}_2 + v_A \hat{a}_1^\dagger. \quad (\text{C1})$$

We define the coefficients v_A and u_A in complete analogy to the degenerate case in Eq. (A1).

To model the loss that occurs inside the interferometer, we place two beam splitters in each branch, whose transmitted outputs is the input of crystal B. We describe the beam splitter S_j with $j = 1, 2$ that accounts for internal loss through the transformation

$$\hat{a}'_j = t_j \hat{a}'_j + r_j \hat{\ell}_j \quad \text{and} \quad \hat{\ell}'_j = t_j^* \hat{\ell}_j - r_j^* \hat{a}'_j. \quad (\text{C2})$$

Here, r_j and t_j denote the amplitude reflectivity and transmittance of the beam splitter. In addition, we use the conventional definitions $R_j = |r_j|^2$ and $T_j = |t_j|^2$ as well as the relation $R_j + T_j = 1$. The operators $\hat{\ell}_j$ describe the noise input of each beam splitter, the operators $\hat{\ell}'_j$ the output according to Fig. 4. The output of crystal B is then found through the relation

$$\hat{b}_1 = u_B \hat{a}'_1 + v_B \hat{a}'_2^\dagger \quad \text{and} \quad \hat{b}_2 = u_B \hat{a}'_2 + v_B \hat{a}'_1^\dagger. \quad (\text{C3})$$

We define the coefficients v_B and u_B as in Eq. (A5). Detection loss is modeled by the transformation

$$\hat{b}'_j = \sqrt{\eta_j} \hat{b}_j + \sqrt{1 - \eta_j} \hat{d}_j, \quad (\text{C4})$$

where η_j is the efficiency of the detector in output mode $j = 1, 2$ and \hat{d}_j the noise that is introduced. Since this transformation is completely analogous to Eq. (A6), we find exactly Eqs. (A9) and (A10), with the index d now replaced by $j = 1, 2$.

With all the transformations above, including the beam splitters S_{η_j} for detection loss, we find

$$\begin{aligned} \hat{b}'_{1,2} &= A_{1,2} \hat{a}_{1,2} + \alpha_{1,2} \hat{a}_{2,1}^\dagger + B_{1,2} \hat{\ell}_{1,2} \\ &+ \beta_{1,2} \hat{\ell}_{2,1}^\dagger + \sqrt{1 - \eta_{1,2}} \hat{d}_{1,2} \end{aligned} \quad (\text{C5})$$

for the field detected by detector $D_{1,2}$. Here, we defined the complex coefficients

$$\begin{aligned} A_{1,2} &= \sqrt{\eta_{1,2}}(t_{1,2} u_A u_B + t_{2,1}^* v_A^* v_B), \quad B_{1,2} = \sqrt{\eta_{1,2}} r_{1,2} u_B, \\ \alpha_{1,2} &= \sqrt{\eta_{1,2}}(t_{1,2} v_A u_B + t_{2,1}^* u_A^* v_B), \quad \beta_{1,2} = \sqrt{\eta_{1,2}} r_{2,1}^* v_B. \end{aligned} \quad (\text{C6})$$

It is straightforward to calculate $\hat{b}'_{1,2}|0\rangle = \alpha_{1,2}|1_{a_{2,1}}\rangle + \beta_{1,2}|1_{\ell_{2,1}}\rangle$. With that result we find, in analogy to the calculation

in the degenerate setup, for $|\psi_j\rangle \equiv \hat{b}_{1,2}^\dagger \hat{b}'_{1,2}|0\rangle$ the expression

$$\begin{aligned} |\psi_{1,2}\rangle &= (|\alpha_{1,2}|^2 + |\beta_{1,2}|^2)|0\rangle + \alpha_{1,2} A_{1,2}^* |1_{a_1}, 1_{a_2}\rangle \\ &+ \alpha_{1,2} B_{1,2}^* |1_{a_{2,1}}, 1_{\ell_{1,2}}\rangle + \beta_{1,2} A_{1,2}^* |1_{a_{1,2}}, 1_{\ell_{2,1}}\rangle \\ &+ \sqrt{1 - \eta_{1,2}} (\alpha_{1,2} |1_{a_{2,1}}\rangle + \beta_{1,2} |1_{\ell_{2,1}}\rangle) |1_{d_{1,2}}\rangle \\ &+ \beta_{1,2} B_{1,2}^* |1_{\ell_1}, 1_{\ell_2}\rangle. \end{aligned} \quad (\text{C7})$$

It is easy to see that the photon number $N_{\eta_j} = \langle 0|\psi_j\rangle = |\alpha_j|^2 + |\beta_j|^2$ detected by D_j takes the form

$$N_{\eta_j}(\phi) = \eta_j(\mathcal{A}_j - \mathcal{K}_j \cos \phi) \quad (\text{C8})$$

with the amplitude $\mathcal{A}_j \equiv T_j V_A + V_B + 2(T_1 + T_2) V_A V_B$ and the contrast $\mathcal{K}_j = 2\sqrt{T_1 T_2 U_A U_B V_A V_B}$. Note that the term in parentheses can be defined as the photon number N_j without detection loss. Moreover, the phase

$$\phi \equiv \arg(u_A u_B v_A v_B^* t_1 t_2) + \pi \quad (\text{C9})$$

is slightly differently defined from Eq. (A14) to include a phase that may be accumulated in the two arms in the interferometer and is included in the complex values of t_j .

When we calculate the variance $\Delta N_{\eta_j}^2 \equiv \langle \psi_j | \psi_j \rangle - N_{\eta_j}^2$, we find with the help of Eq. (C7)

$$\Delta N_{\eta_j}^2 = (|\alpha_j|^2 + |\beta_j|^2)(1 - \eta_j + |A_j|^2 + |B_j|^2). \quad (\text{C10})$$

With the use of $|A_j|^2 + |B_j|^2 = \eta_j + |\alpha_j|^2 + |\beta_j|^2$, as well as Eq. (C8), this expression reduces to

$$\Delta N_{\eta_j}^2 = N_{\eta_j}(1 + N_{\eta_j}). \quad (\text{C11})$$

It also implies directly that $\Delta N_j^2 = N_j(1 + N_j)$ in the case without detection loss. Moreover, the variance of the sum of both signals is

$$\Delta N_+^2 = \Delta N_{\eta_1}^2 + \Delta N_{\eta_2}^2 + \langle \psi_1 | \psi_2 \rangle + \langle \psi_2 | \psi_1 \rangle - 2N_{\eta_1} N_{\eta_2}. \quad (\text{C12})$$

The overlap

$$\langle \psi_1 | \psi_2 \rangle = N_{\eta_1} N_{\eta_2} + (\alpha_2 A_1 + \beta_2 B_1)(\alpha_1 A_2 + \beta_1 B_2)^* \quad (\text{C13})$$

takes a simple form. Calculating the product is cumbersome, but using trigonometric relations, the definition of the phase ϕ , the relations $U_j = 1 + V_j$ as well as $T_j + R_j = 1$, and Eq. (C8) we arrive at

$$\begin{aligned} \Delta N_+^2 &= (N_{\eta_1} + N_{\eta_2})(1 + N_{\eta_1} + N_{\eta_2}) + \eta_2 N_{\eta_1} + \eta_1 N_{\eta_2} \\ &+ \eta_1 \eta_2 [2T_1 T_2 - (T_1 + T_2)] V_A. \end{aligned} \quad (\text{C14})$$

- [1] B. Yurke, S. L. McCall, and J. R. Klauder, SU(2) and SU(1,1) interferometers, *Phys. Rev. A* **33**, 4033 (1986).
- [2] C. M. Caves, Quantum-mechanical noise in an interferometer, *Phys. Rev. D* **23**, 1693 (1981).
- [3] M. V. Chekhova and Z. Y. Ou, Nonlinear interferometers in quantum optics, *Adv. Opt. Photon.* **8**, 104 (2016).
- [4] D. Linnemann, H. Strobel, W. Muesel, J. Schulz, R. J. Lewis-Swan, K. V. Kheruntsyan, and M. K. Oberthaler, Quantum-Enhanced Sensing Based on Time Reversal of Nonlinear Dynamics, *Phys. Rev. Lett.* **117**, 013001 (2016).
- [5] C. Sparaciari, S. Olivares, and M. G. A. Paris, Gaussian-state interferometry with passive and active elements, *Phys. Rev. A* **93**, 023810 (2016).
- [6] M. Manceau, F. Khalili, and M. V. Chekhova, Improving the phase super-sensitivity of squeezing-assisted interferometers by squeeze factor unbalancing, *New J. Phys.* **19**, 013014 (2017).
- [7] M. Manceau, G. Leuchs, F. Khalili, and M. V. Chekhova, Detection Loss Tolerant Supersensitive Phase Measurement with an SU(1,1) Interferometer, *Phys. Rev. Lett.* **119**, 223604 (2017).
- [8] A. M. Pérez, T. Sh. Iskhakov, P. Sharapova, S. Lemieux, O. V. Tikhonova, M. V. Chekhova, and G. Leuchs, Bright squeezed-vacuum source with 1.1 spatial mode, *Opt. Lett.* **39**, 2403 (2014).
- [9] P. Sharapova, A. M. Pérez, O. V. Tikhonova, and M. V. Chekhova, Schmidt modes in the angular spectrum of bright squeezed vacuum, *Phys. Rev. A* **91**, 043816 (2015).
- [10] S. Lemieux, M. Manceau, P. R. Sharapova, O. V. Tikhonova, R. W. Boyd, G. Leuchs, and M. V. Chekhova, Engineering the Frequency Spectrum of Bright Squeezed Vacuum via Group Velocity Dispersion in an SU(1,1) Interferometer, *Phys. Rev. Lett.* **117**, 183601 (2016).
- [11] L. Beltran, G. Frascella, A. M. Pérez, R. Fickler, P. R. Sharapova, M. Manceau, O. V. Tikhonova, R. W. Boyd, G. Leuchs, and M. V. Chekhova, Orbital angular momentum modes of high-gain parametric down-conversion, *J. Opt.* **19**, 044005 (2017).
- [12] W. N. Plick, J. P. Dowling, and G. S. Agarwal, Coherent-light-booster, sub-shot noise, quantum interferometry, *New J. Phys.* **12**, 083014 (2010).
- [13] D. Li, C.-H. Yuan, Z. Y. Ou, and W. Zhang, The phase sensitivity of an SU(1,1) interferometer with coherent and squeezed-vacuum light, *New J. Phys.* **16**, 073020 (2014).
- [14] A. M. Marino, N. V. Corzo Trejo, and P. D. Lett, Effect of losses on the performance of an SU(1,1) interferometer, *Phys. Rev. A* **86**, 023844 (2012).
- [15] Z. Y. Ou, Enhancement of the phase-measurement sensitivity beyond the standard quantum limit by a nonlinear interferometer, *Phys. Rev. A* **85**, 023815 (2012).
- [16] L. J. Wang, X. Y. Zou, and L. Mandel, Induced coherence without induced emission, *Phys. Rev. A* **44**, 4614 (1991).
- [17] M. I. Kolobov, E. Giese, S. Lemieux, R. Fickler, and R. W. Boyd, Controlling induced coherence for quantum imaging, *J. Opt.* **19**, 054003 (2017).
- [18] B. E. Anderson, B. L. Schmittberger, P. Gupta, K. M. Jones, and P. D. Lett, Optimal phase measurements with bright- and vacuum-seeded SU(1,1) interferometers, *Phys. Rev. A* **95**, 063843 (2017).
- [19] B. E. Anderson, P. Gupta, B. L. Schmittberger, T. Horrom, C. Hermann-Avigliano, K. M. Jones, and P. D. Lett, Phase sensing beyond the standard quantum limit with a variation on the SU(1,1) interferometer, *Optica* **4**, 752 (2017).
- [20] J. Kong, J. Jing, H. Wang, F. Hudelist, C. Liu, and W. Zhang, Experimental investigation of the visibility dependence in a nonlinear interferometer using parametric amplifiers, *Appl. Phys. Lett.* **102**, 011130 (2013).
- [21] R. Demkowicz-Dobrzański, J. Kołodyński, and M. Guţă, The elusive Heisenberg limit in quantum-enhanced metrology, *Nat. Commun.* **3**, 1063 (2012).
- [22] J. Sahota and N. Quesada, Quantum correlations in optical metrology: Heisenberg-limited phase estimation without mode entanglement, *Phys. Rev. A* **91**, 013808 (2015).
- [23] S. S. Szegedi, R. J. Lewis-Swan, and S. A. Haine, Pumped-Up SU(1,1) Interferometry, *Phys. Rev. Lett.* **118**, 150401 (2017).
- [24] L. Pezzé and A. Smerzi, Mach-Zehnder Interferometry at the Heisenberg Limit with Coherent and Squeezed-Vacuum Light, *Phys. Rev. Lett.* **100**, 073601 (2008).
- [25] L. Pezzé and A. Smerzi, Quantum theory of phase estimation, in *Atom Interferometry*, in *Proceedings of the International School of Physics "Enrico Fermi,"* edited by G. M. Tino and M. A. Kasevich (IOS Press, The Netherlands, 2014), Vol. 188, p. 691.
- [26] F. Hudelist, J. Kong, C. Liu, J. Jing, Z. Y. Ou, and W. Zhang, Quantum metrology with parametric amplifier-based photon correlation interferometers, *Nat. Commun.* **5**, 3049 (2014).
- [27] C. Sparaciari, S. Olivares, and M. G. A. Paris, Bounds to precision for quantum interferometry with Gaussian states and operations, *J. Opt. Soc. Am. B* **32**, 1354 (2015).
- [28] J. Xin, H. Wang, and J. Jing, The effect of losses on the quantum-noise cancellation in the SU(1,1) interferometer, *Appl. Phys. Lett.* **109**, 051107 (2016).

Chapter 6

A primary radiation standard based on quantum nonlinear optics

The impetus to this work occurred in 2015 when I was working in Prof. Maria Chekhova's laboratory in Erlangen, analyzing the data for the letter in Chapter 2. Prof. Chekhova had noticed that the frequency spectrum of phase-matched SPDC was described by a parabola, and could therefore be used as a reference to retrieve the instrument response function of a spectrometer. We utilized and briefly described that technique in [48], using data acquired by Dr. Mathieu Manceau.

In the article, we describe a two-step method to use PDC as a primary standard for the intensity of light. The first step allows one to obtain the instrument response function of the spectrometer. The second step makes use of the instrument response function to deduce the number of photons in high-gain PDC.

Prof. Maria Chekhova had the idea for the first step. I designed the experiment with the help of Dr. Robert Fickler, and derived the theory with Dr. Enno Giese. While working on the theory for the first step, I had the idea for the second step, and fleshed it out with Dr. Robert Fickler and Dr. Enno Giese. I then performed both experiments, analyzed the data, and wrote most of the paper. Dr. Enno Giese wrote the theory portion of the supplementary material. All this work was supervised by Profs. Maria Chekhova, Robert W. Boyd and Gerd Leuchs.

I, along with coinventors Prof. Maria Chekhova, Dr. Mathieu Manceau, Prof. Gerd

Leuchs and Prof. Robert Boyd, have a patent for using SPDC to extract the instrument response function of a measuring apparatus [49].

A primary radiation standard based on quantum nonlinear optics

Samuel Lemieux^{1*}, Enno Giese^{1,6}, Robert Fickler^{1,7}, Maria V. Chekhova^{2,3,4} and Robert W. Boyd^{1,5}

The black body remains the most prominent source of light for absolute radiometry¹. Its main alternative, synchrotron radiation, requires costly and large facilities². Quantum optics offers a new radiometric source: parametric down-conversion (PDC), a nonlinear optical process, in which pairwise photon correlations enable absolute calibration of photodetectors^{3–6}. Since the emission rate crucially depends on the brightness of the electromagnetic field, quantum-mechanical fluctuations of the vacuum⁷ can be seen as a seed of spontaneous PDC, and their amplitude is a natural radiometric standard. Thus, they allow for the calibration of the spectral radiance of light sources^{8–11} by measuring the ratio between seeded and unseeded PDC. Here, we directly use the frequency spectrum of the electromagnetic vacuum to trigger spontaneous PDC and employ the generated light to infer the spectral response of a spectrometer over a broad spectral range. Then, we deduce the absolute quantum efficiency from the spectral shape of PDC in the high-gain regime, without relying on a seed or reference detector. Our results compare well with the ones obtained with a reference lamp, demonstrating a promising primary radiation standard.

In general, a source can serve as a primary radiation standard if, within a specified bandwidth centred on the wavelength λ , the exact number of emitted photons $N(\lambda)$ is known. However, the number of counts $M(\lambda)$ recorded by a detector does not usually coincide with $N(\lambda)$ due to an imperfect quantum efficiency $\eta(\lambda)$ of the detecting device. These quantities are simply connected through the relation

$$M(\lambda) = \eta(\lambda)N(\lambda) \quad (1)$$

Measuring $M(\lambda)$ while having a precise knowledge of $N(\lambda)$ allows the determination of $\eta(\lambda)$, which is at the heart of the absolute calibration of spectrometers. The spectral efficiency $\eta(\lambda)$ can be further separated into its relative spectral shape $R(\lambda)$ (that is, the response function of the measurement device) and a wavelength-independent proportionality constant α , through $\eta(\lambda) = \alpha R(\lambda)$. Whereas a relative calibration procedure gives $R(\lambda)$, obtaining the full $\eta(\lambda)$ requires an absolute calibration. In the following we demonstrate in a two-step procedure that both relative and absolute calibration can be performed using parametric down-conversion (PDC).

The total number of photons reaching the detector depends on the photon-number distribution \mathcal{N} per plane-wave mode characterizing the source, and on the modes that are detected. Using standard

radiometric formalism (see details in the Methods), this fact translates to the expression

$$N(\lambda) = \frac{1}{(2\pi)^3} \int_{\text{source}} d^3r \int_{\text{detector}} d^3k \mathcal{N} \approx [A_s c \tau_s] [\Delta\Omega \Delta\lambda] \mathcal{D}(\lambda) \mathcal{N} \quad (2)$$

where the first integral can be approximated by the transverse area A_s of the source and the duration of the emission τ_s multiplied by the speed of light c . The second integral describes the modes that are detected and can be approximated by the bandwidth $\Delta\lambda$ and solid angle $\Delta\Omega$ of the detector, if \mathcal{N} does not vary significantly over these quantities. To connect the plane waves to the solid angle and the wavelength, which are the relevant quantities for a spectrometer, we also introduced the quantity $\mathcal{D}(\lambda) = (2\pi)^3 \lambda^{-4}$, which is a measure of the mode density⁷. If \mathcal{N} is known, we have all the necessary quantities for the absolute calibration of a spectrometer.

During the three-wave mixing process of PDC, pump photons (of frequency ω_p) interact with the vacuum field within a crystal with a nonlinear susceptibility $\chi^{(2)}$. This process leads to the generation of pairs of photons known as the signal and idler, of frequencies ω and ω_i . In the spontaneous regime (low pump intensity), \mathcal{N} , a function of frequency and emission angle, depends on the amplitude of the vacuum fluctuations, the profile of the pump beam, the gain of the amplification process and a phase-matching function. For a monochromatic plane wave pump of amplitude E_p and a crystal of thickness L , the photon-number spectral distribution of spontaneous PDC is given by

$$\mathcal{N} = (c^{-1} L \chi^{(2)} E_p)^2 \sqrt{\omega \omega_i / (n n_i)}^2 \text{sinc}^2(\Delta\kappa L / 2) \quad (3)$$

where n and n_i are the signal and idler refractive indices and $\Delta\kappa = \kappa_p - \kappa - \kappa_i$ is the mismatch between the longitudinal wave-vectors of the pump, the signal and the idler, respectively^{7,12}. The frequency-dependent factors $\sqrt{\omega / n}$ and $\sqrt{\omega_i / n_i}$ arise from the quantization of the electric field for the signal and for the idler¹³. In the spontaneous regime of pair creation, those factors embody the amplitude of the vacuum fluctuations for the biphoton field given by the density of states. They explicitly appear in the expression for the electric field operators for the signal and for the idler, which are used in turn to write the Hamiltonian for the nonlinear interaction. To denote the coupling strength, we use the gain parameter $\mathcal{G} = c^{-1} L \chi^{(2)} E_p / \sqrt{n n_i}$, which we can assume to be constant over

¹Department of Physics, University of Ottawa, Ottawa, Ontario, Canada. ²Max Planck Institute for the Science of Light, Erlangen, Germany.

³Physics Department, Lomonosov Moscow State University, Moscow, Russia. ⁴University of Erlangen-Nuremberg, Erlangen, Germany.

⁵Institute of Optics, University of Rochester, Rochester, NY, USA. ⁶Present address: Institut für Quantenphysik and Center for Integrated Quantum Science and Technology, Universität Ulm, Ulm, Germany. ⁷Present address: Photonics Laboratory, Physics Unit, Tampere University, Tampere, Finland.

*e-mail: [REDACTED]

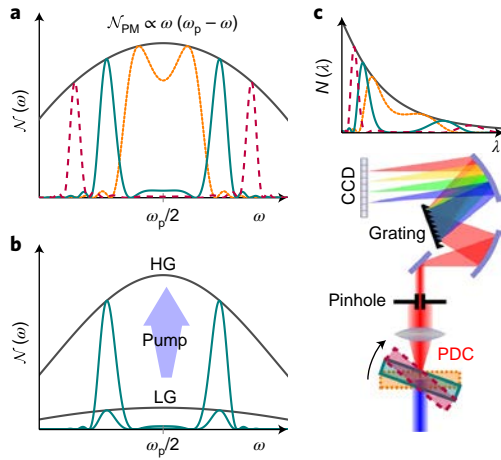


Fig. 1 | Physical principle and idealized set-up. **a**, Different tilt angles of the nonlinear crystal correspond to different phase-matching conditions, altering the spectrum $\mathcal{N}(\omega)$ accordingly, as exemplified by the orange, green and magenta curves. $\mathcal{N}_{\text{PM}}(\omega)$ (grey curve) is obtained by taking the maximum of \mathcal{N} for different phase-matching conditions. Since the shape of $\mathcal{N}_{\text{PM}}(\omega)$ is known, see equation (4), we can use it as a reference to retrieve the response function $R(\lambda)$. **b**, The relative calibration with PDC is performed in the low-gain regime (LG) and the absolute calibration with PDC in the high-gain regime (HG). We transition from low gain to high gain by increasing the intensity of the pump laser. In the high-gain limit, there is a one-to-one correspondence between the shape of \mathcal{N}_{PM} and the number of generated photons, leading to an absolute standard. **c**, For each tilt angle of the nonlinear crystal, the photon-number spectrum $N(\lambda)$ is measured with an angular filter (a pinhole in the far field selects a small solid angle) and a spectrometer. The shape of $N(\lambda)$ follows from the conversion of $\mathcal{N}(\omega)$ from the plane-wave representation to the wavelength and solid-angle representation associated with the spectrometer. CCD, charge-coupled device.

the frequency range of interest. This assumption is discussed in the Methods.

The last factor of equation (3) is the well-known phase-matching function of a bulk crystal. At exact phase-matching, $\Delta\kappa$ vanishes and the phase-matching function takes on the value unity. Thus, the phase-matched distribution (3) takes its maximal value and reads

$$\mathcal{N}_{\text{PM}} = \mathcal{G}^2 \omega (\omega_p - \omega) \quad (4)$$

where we assumed that photon energy is conserved in the parametric process, such that $\omega_i = \omega_p - \omega$. For absolute calibration, we need a complete knowledge of \mathcal{N}_{PM} , but it is difficult to determine \mathcal{G} experimentally in the spontaneous regime of PDC. However, the photon number for different \mathcal{N}_{PM} follows a parabola, as illustrated in Fig. 1a. Because $\omega(\omega_p - \omega)$ does not depend on laboratory parameters, we use the shape of \mathcal{N}_{PM} and perform a relative calibration¹².

By introducing a pinhole in the far-field of the crystal, we limit the emission solid angle and suppress the frequency content in the other angular modes (details in the Methods). A spectrometer then disperses the light and images it onto a charge-coupled device chip (see Fig. 1c). Since the position on the chip corresponds to a particular wavelength, we expect a specific functional behaviour that originates in the parabola but is modified by $\mathcal{D}(\lambda)$ ¹⁴. Thus, any deviation of the measured spectrum at the phase-matched wavelength from $\mathcal{D}(\lambda)\omega(\omega_p - \omega)$ can be assigned to detector inefficiencies, and therefore to $R(\lambda)$.

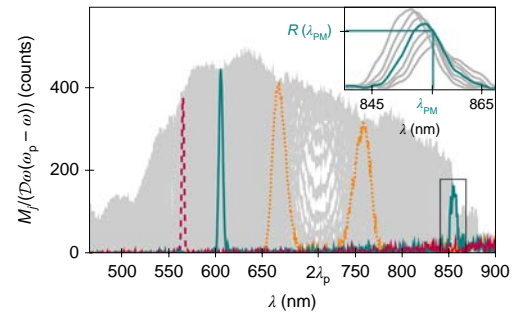


Fig. 2 | Measured spectra. We extract the response function $R(\lambda)$ from the overlap of 411 measured spectra (grey). The twin-peak structure in the orange and teal spectra is a feature of phase matching and energy conservation. For the magenta curve, the second peak does not lie within our measurement range. The maximum possible signal at a certain wavelength λ is proportional to $R(\lambda)$. To illustrate this method, the inset shows several spectra (Fourier-filtered to suppress the noise) from the box enclosing the right-hand peak of the teal curve.

Since $R(\lambda)$ is proportional to the ratio between the number of counts $M(\lambda)$ and the number of photons $N(\lambda)$, we can write

$$R(\lambda) \propto \frac{M(\lambda)}{\mathcal{D}(\lambda)\omega(\omega_p - \omega)} \bigg|_{\text{PM, LG}} \quad (5)$$

where $\omega = 2\pi c/\lambda$ and we used the proportionality symbol because \mathcal{G} is yet to be determined. The right-hand side is evaluated at the wavelength λ_{PM} that satisfies the phase-matching condition and the measured spectra $M(\lambda)$ are acquired in the low-gain limit, denoted by LG.

In our experiment, we pump a barium borate (BBO) crystal with a pulsed laser (355 nm wavelength) and acquire a large number of spectra M_j , with j corresponding to different tilt angles of the nonlinear crystal, spanning phase-matched frequencies over a broad spectral range, as shown at the bottom of Fig. 1c. We overlap all the measured spectra in Fig. 2 and highlight three of them to show their twin-peak structure. Crucially, the maximum number of counts at any particular wavelength as the crystal tilt angle is varied gives the phase-matched measurement $M_j(\lambda_{\text{PM}})$, because $\text{sinc}^2(\Delta\kappa L/2)$ is equal to unity only when the phase-matching condition is satisfied. We show in the inset of Fig. 2 and in the Methods that the peak number of counts in a single spectrum does not always occur at λ_{PM} .

We perform the experiment in the spontaneous regime of PDC to ensure the validity of equation (3). We retrieve $R(\lambda)$ directly from the spectra by virtue of equation (5), where $M(\lambda_{\text{PM}})$ is extracted by taking the maximum of many spectra. We assume the normalization condition that for degenerate down-conversion $R(2\lambda_p) = 1$, such that $\eta(2\lambda_p) = \alpha$. The response function obtained from the spontaneous PDC agrees very well with the response function measured with a reference lamp (Fig. 3). The experiment was repeated with an additional dichroic filter to demonstrate that the method resolves rich and rapidly varying spectral features. For a proper comparison, it is crucial that the light from spontaneous PDC and from the reference lamp undergo exactly the same transfer function. The skewness of the PDC response with respect to that of the lamp stems from chromatic aberration and non-perfect polarization filtering, as well as inaccuracies in the reference spectrum of the lamp.

To improve the precision of our method, one could include the frequency dependence of \mathcal{G} if the linear and nonlinear dispersion relations of the crystal are known. In this case, it is also straightforward to generalize equation (3) so that it incorporates the spatial

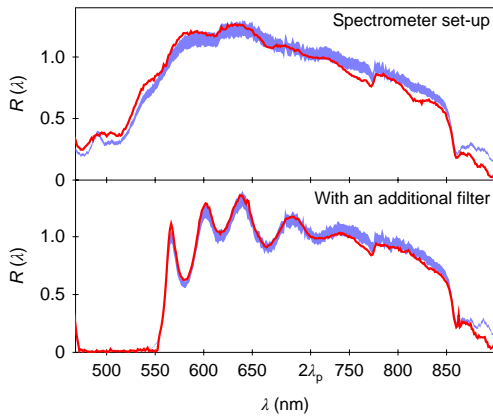


Fig. 3 | Spectral response function of the experimental set-up. Upper panel shows a comparison of $R(\lambda)$ obtained from spontaneous PDC (red, normalized to unity at the degenerate wavelength $2\lambda_p$) and the response function measured with a reference lamp (blue envelope enclosing the 5% error reported by the manufacturer; scaled onto the PDC curves using a linear fit). To obtain the curves in the lower panel, we added a dichroic filter to the spectrometer to induce rich spectral features into the response function.

and temporal profiles of the pump beam¹⁵. To stress the simplicity of our procedure, we refrain from applying these corrections, but nonetheless obtain excellent results. With a knowledge of $R(\lambda)$ we can accurately measure the shape of any spectrum. In the following, we perform the second step of our calibration procedure and establish an absolute calibration method. In particular, we extract the number of photons from the shape of high-gain PDC spectra, based on our previous measurement of $R(\lambda)$, as exemplified in Fig. 1b, where we see a distortion of the parabola when the gain is increased.

For an arbitrary value of the gain, the photon-number spectral distribution under phase matching and for a monochromatic, plane-wave undepleted pump, becomes

$$\mathcal{N}_{\text{PM}} = \sinh^2 \left(\mathcal{G} \sqrt{\omega(\omega_p - \omega)} \right) \quad (6)$$

which reduces to equation (4) in the spontaneous regime—that is, for $\mathcal{G} \sqrt{\omega(\omega_p - \omega)} \ll 1$. In the high-gain regime, the phase-matched photon-number spectrum is therefore a distorted parabola, whose spectral shape (curvature) and photon number are uniquely determined by the gain parameter \mathcal{G} . In complete analogy to equation (5) we obtain the relation

$$\alpha \sinh^2 \left(\mathcal{G} \sqrt{\omega(\omega_p - \omega)} \right) = \frac{M(\lambda)}{R(\lambda)\mathcal{D}(\lambda)\Gamma} \bigg|_{\text{PM}} \quad (7)$$

where we introduced, for a more convenient notation, the constant $\Gamma = \Delta\Omega\Delta\lambda A_s c \tau_s$ for the emission and detection parameters. Note that, in contrast to equation (5), we have an equality. Except for α , which we defined earlier through $\eta(\lambda) = \alpha R(\lambda)$, all the quantities are known: we obtained $R(\lambda)$ from spontaneous PDC and the shape of the phase-matched spectrum uniquely determines \mathcal{G} . We approximate A_s by the transverse area of the pump beam and τ_s by $m\tau_p$, with τ_p being the pump pulse duration and m the number of pulses during an acquisition time. Further, we calculate the solid angle $\Delta\Omega$ from the pinhole size in the far field of the crystal, and obtain $\Delta\lambda$ from the bandwidth associated with a pixel of the spectrometer's camera. The only remaining free parameter, α , is obtained via fitting.

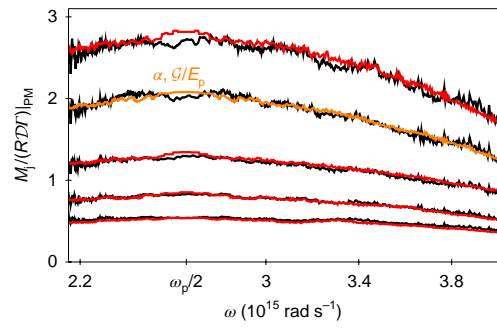


Fig. 4 | Absolute calibration from high-gain PDC. The maxima of densely packed high-gain spectra (right-hand side of equation (7); shown in black) and their fit (left-hand side of equation (7); shown in red and orange) are obtained for five different pump intensities. The curves are shown in the frequency domain to highlight the distortion of the parabola. The fit parameters for the orange curve were obtained with the second-to-top measurement. To demonstrate their accuracy, we used the same fit parameters to draw the red curves. The fitting curves are noisy because fluctuations in the pump energy are taken into account.

For that, we acquire a large number of densely packed spectra $M_j(\lambda)$ for different crystal tilt angles with a much higher pump energy per pulse to reach a large parametric gain. After taking the maxima of these dense spectra, we perform a bivariate curve fit using the free parameter α and the pump-normalized gain \mathcal{G}/E_p , a quantity that allows us to suppress the pulse energy drift of our pump laser over the acquisition time, and where a relative measurement of E_p is sufficient. We then obtain the spectral quantum efficiency by taking the product $\eta(\lambda) = \alpha R(\lambda)$, with R inferred from the spontaneous measurement and α from the high-gain regime.

In the absolute calibration measurement, we use a pump energy four times higher than in the spontaneous configuration. We show the maxima of the spectra and the fit (orange curve) in Fig. 4. The quantum efficiency at $\lambda = 2\lambda_p$, extracted from fitting, is $\alpha = 0.42 \pm 0.04$, where the uncertainty is dominated by the systematic error in the pulse duration and transverse profile of the pump. Note that α includes all the losses in the optical set-up, from the nonlinear crystal to the detector. The estimated quantum efficiency of the experimental set-up, based on the nominal efficiency of each optical component, is $\alpha = 0.38 \pm 0.07$. The largest source of loss is the diffraction grating of the spectrometer, with an efficiency of 60% at $2\lambda_p$, as reported by the manufacturer. In addition, we tested the consistency of the fit parameters by repeating the measurement with other pump energies. Using the previously obtained value of α , and estimating the gain from \mathcal{G}/E_p and a new measurement of E_p , we obtain the red curves (Fig. 4), which also show excellent agreement with experimental data. Undesired effects due to additional nonlinear processes arising with the higher pump intensity, such as self-focusing or fluorescence, are found to be negligible.

Equation (6) is obtained by solving the Heisenberg equation of motion for the creation and annihilation operators in the form of a Bogolyubov transformation relating the modes associated with the signal and the idler photons⁷. The validity of models for high-gain PDC in the context of a pulsed laser has been discussed¹⁶ and verified experimentally by looking at the exponential increase in the number of photons with the pump power^{14,17–20}. The results presented in Fig. 4 are experimental demonstrations of the distortion of the phase-matched spectral shape of light generated by a pulsed laser for increasing gain, and as such provide additional support for this description of PDC. Moreover, equation (7) underlines that high-gain PDC offers the possibility to perform the absolute calibration of a single-element detector by measuring the number of counts against the pump pulse energy.

In contrast to the relative calibration, the absolute calibration using high-gain PDC cannot be straightforwardly generalized to arbitrary pump beams. Corrections to the model could be implemented, for instance by taking into account the spatial profile and frequency spectrum of the pump as well as the frequency dependence of \mathcal{G} . However, our results demonstrate that even without a more sophisticated treatment, which would require the determination of many more laboratory parameters and solving Heisenberg's equations of motion numerically, we measure the quantum efficiency accurately. State-of-the-art spectroradiometric sources based on black-body radiation, which have benefited from a century of technical improvements, typically exhibit a relative uncertainty of the order of 1% around the wavelength 700 nm (ref. ²¹), whereas we report a relative uncertainty of the order of 10%. It is reasonable to expect that a PDC standard could reach the level of precision of methods based on black-body radiation. As a first step, one could carefully monitor the pump laser spatial profile and pulse duration. Less prominent sources of error, which include geometric factors and the quality of the fitting, could also be addressed. Furthermore, it would be interesting to explore different strategies to engineer the density of states, by using for instance metallic surfaces or nanoparticles, to increase the brightness of the source.

Online content

Any methods, additional references, Nature Research reporting summaries, source data, statements of data availability and associated accession codes are available at <https://doi.org/10.1038/s41567-019-0447-2>.

Received: 13 August 2018; Accepted: 24 January 2019;

Published online: 4 March 2019

References

- Hollandt, J. et al. in *Optical Radiometry: Volume 41 (Experimental Methods in the Physical Sciences)* (eds Parr, A. C. et al.) Ch. 5 (Elsevier, Amsterdam, 2005).
- Lemke, D. & Labs, D. The Synchrotron Radiation of the 6-GeV DESY Machine as a Fundamental Radiometric Standard. *Appl. Opt.* **6**, 1043–1048 (1967).
- Klyshko, D. N. Use of two-photon light for absolute calibration of photoelectric detectors. *Sov. J. Quantum Electron.* **10**, 1112–1117 (1980).
- Malygin, A. A., Penin, A. N. & Sergienko, A. V. Absolute calibration of the sensitivity of photodetectors using a biphotonic field. *JETP Lett.* **33**, 477–480 (1981).
- Polyakov, S. V. & Migdall, A. L. High accuracy verification of a correlated-photon-based method for determining photon-counting detection efficiency. *Opt. Express* **15**, 1390–1407 (2007).
- Rarity, J. G., Ridley, K. D. & Tapster, P. R. Absolute measurement of detector quantum efficiency using parametric downconversion. *Appl. Opt.* **26**, 4616–4619 (1987).
- Klyshko, D. N. *Photons and Nonlinear Optics* (Gordon and Breach, Boca Raton, 1989).
- Klyshko, D. N. Utilization of vacuum fluctuations as an optical brightness standard. *Sov. J. Quantum Electron.* **7**, 591–595 (1977).
- Kitaeva, G. Kh., Penin, A. N., Fadeev, V. V. & Yanait, Yu. A. Measurement of brightness of light fluxes using vacuum fluctuations as a reference. *Sov. Phys. Dokl.* **24**, 564–566 (1979).
- Migdall, A., Datla, R., Sergienko, A., Orszak, J. S. & Shih, Y. H. Measuring absolute infrared spectral radiance with correlated visible photons: technique verification and measurement uncertainty. *Appl. Opt.* **37**, 3455–3463 (1998).
- Kornienko, V. V., Kitaeva, G. Kh., Sedlmeir, F., Leuchs, G. & Schwefel, H. G. Towards terahertz detection and calibration through spontaneous parametric down-conversion in the terahertz idler-frequency range generated by a 795 nm diode laser system. *APL Photon.* **3**, 051704 (2018).
- Lemieux, S. et al. Engineering the frequency spectrum of bright squeezed vacuum via group velocity dispersion in an SU(1, 1) interferometer. *Phys. Rev. Lett.* **117**, 183601 (2016).
- Milonni, P. Field quantization and radiative processes in dispersive dielectric media. *J. Mod. Opt.* **42**, 1991–2004 (1995).
- Spasibko, K. Yu, Iskhakov, T., Sh. & Chekhova, M. V. Spectral properties of high-gain parametric down-conversion. *Opt. Express* **20**, 7507–7515 (2012).
- Hsu, F.-K. & Lai, C.-W. Absolute instrument spectral response measurements using angle-resolved parametric fluorescence. *Opt. Express* **21**, 18538–18552 (2013).
- Dayan, B. Theory of two-photon interactions with broadband down-converted light and entangled photons. *Phys. Rev. A* **76**, 043813 (2007).
- Agafonov, I. N., Chekhova, M. V. & Leuchs, G. Two-color bright squeezed vacuum. *Phys. Rev. A* **82**, 011801 (2010).
- Allevi, A. et al. Coherence properties of high-gain twin beams. *Phys. Rev. A* **90**, 063812 (2014).
- Brida, G., Meda, A., Genovese, M., Predazzi, E. & Ruo-Berchera, I. Systematic study of the PDC speckle structure for quantum imaging applications. *J. Mod. Opt.* **56**, 201–208 (2009).
- Pérez, A. M. et al. Bright squeezed-vacuum source with 1.1 spatial mode. *Opt. Lett.* **39**, 2403–2406 (2014).
- Yoon, H. W., Gibson, C. E. & Barnes, P. Y. Realization of the National Institute of Standards and Technology detector-based spectral irradiance scale. *Appl. Opt.* **41**, 5879–5890 (2002).

Acknowledgements

We thank O. Reshef for valuable discussions. This research was performed as part of a collaboration within the Max Planck-University of Ottawa Centre for Extreme and Quantum Photonics, whose support we gratefully acknowledge. This work was supported by the Canada First Research Excellence Fund award on Transformative Quantum Technologies and by the Natural Sciences and Engineering Council of Canada (NSERC). R.F. acknowledges the financial support of the Banting postdoctoral fellowship of the NSERC and S.L. the financial support from Le Fonds de Recherche du Québec Nature et Technologies.

Author contributions

M.V.C. conceived the idea for relative calibration. S.L., E.G. and R.F. extended that idea to the absolute calibration scheme. S.L. and R.F. designed the experiment. S.L. conducted the experiment and performed the data analysis. S.L., E.G. and R.F. wrote the manuscript. M.V.C. and R.W.B. supervised the project. All authors contributed to scientific discussions.

Competing interests

S.L., M.V.C. and R.W.B., along with coinventors M. Manceau and G. Leuchs, the University of Ottawa and the Max Planck Institute for the Science of Light, have an international patent application (PCT/IB2017/056450) currently pending, about the relative calibration using PDC. E.G. and R.F. declare that they have no competing interests.

Additional information

Supplementary information is available for this paper at <https://doi.org/10.1038/s41567-019-0447-2>.

Reprints and permissions information is available at www.nature.com/reprints.

Correspondence and requests for materials should be addressed to S.L.

Publisher's note: Springer Nature remains neutral with regard to jurisdictional claims in published maps and institutional affiliations.

© The Author(s), under exclusive licence to Springer Nature Limited 2019

Methods

Radiometry. Since the quantization of the electric field is usually performed in plane-wave modes denoted by a wavevector \mathbf{k} , we express general radiometric quantities through the photon number per mode $\mathcal{N}(\mathbf{k})$ of the field under consideration. A detector cannot detect all of these modes, and hence the detected photon number per source volume can be written as

$$\mathcal{Q} = \frac{1}{(2\pi)^3} \int_{\text{detector}} d^3k \mathcal{N}(\mathbf{k}) = \int_{\Delta\lambda} d\lambda \int_{\Delta\Omega} d\Omega \frac{1}{\lambda^4} \mathcal{N}(\mathbf{k}) \quad (8)$$

where we used $d^3k = k^2 dk d\Omega = (2\pi)^3 \lambda^{-4} d\lambda d\Omega$ in the last step. We neglect here the index of refraction of air and assume that the detector has a bandwidth of $\Delta\lambda$ and collects light from a solid angle $\Delta\Omega$. In the following we introduce for a more convenient notation the Jacobian $\mathcal{D}(\lambda) = (2\pi)^3 \lambda^{-4}$, relating d^3k and $d\lambda d\Omega$, which is proportional to the mode density. For a sufficiently small $\Delta\lambda$ around the wavelength λ and a small $\Delta\Omega$ around the direction set by \mathbf{k} , we can perform the integration and find

$$\mathcal{Q}(\lambda, \Omega) \cong \frac{1}{(2\pi)^3} [\Delta\lambda \Delta\Omega] \mathcal{D}(\lambda) \mathcal{N}(\mathbf{k}) \quad (9)$$

This quantity is closely related to the spectral radiance $\hbar\omega(2\pi)^{-3} c \mathcal{D}(\lambda) \mathcal{N}$, which is the energy per unit of time, area of the source, solid angle and bandwidth (in wavelength) of the detector²².

To calculate the total number of photons that fall onto the detector, equation (9) has to be integrated over the volume of the source, to obtain

$$\mathcal{N}(\lambda, \Omega) = \int_{\text{source}} d^3r \mathcal{Q}(\lambda, \Omega) \cong (2\pi)^{-3} [A_s c \tau_s] [\Delta\lambda \Delta\Omega] \mathcal{D}(\lambda) \mathcal{N} \quad (10)$$

where in the last step we assumed that the source has a surface area of A_s and emits light for a time duration τ_s .

We have not yet specified $\mathcal{N}(\mathbf{k})$. We do that in the next section and show that the assumption of a small solid angle as well as a small bandwidth of the detector is justified.

Angular distribution of spontaneous PDC. The photon number per mode \mathcal{N} for spontaneous PDC in a bulk crystal of length L with a nonlinearity $\chi^{(2)}$ and illuminated by a plane wave pump with a field amplitude E_p is given by equation (3). The longitudinal wavevectors appearing in the expression for $\Delta\kappa$ are given by $\kappa \equiv \sqrt{k^2 - q^2}$ for the signal and $\kappa_i \equiv \sqrt{k_i^2 - q_i^2}$ for the idler. Here, the signal and idler photons have the wavevectors \mathbf{k} and \mathbf{k}_i and the transverse wavevectors \mathbf{q} and \mathbf{q}_i . Note that $k_j = \omega_j n_j / c$, with c the speed of light and ω_j the frequency of the idler and pump fields with $j = i, p$, and no subscript for the signal.

With this notation, we find the expression

$$\Delta\kappa = k_p - \kappa - \sqrt{k_i^2 - q_i^2} \quad (11)$$

for the longitudinal wavevector mismatch. Since we assume in equation (3) a plane wave and monochromatic pump, we have due to energy conservation $\omega_i = \omega_p - \omega$ and due to momentum conservation $\mathbf{q} = -\mathbf{q}_i$. Hence, our expression depends only on ω and \mathbf{q} . Moreover, introducing spherical coordinates, we can define the polar angle θ of the detected field and have $\cos\theta = \kappa/k$ and $\sin\theta = |\mathbf{q}|/k$. Therefore, the longitudinal wavevector mismatch

$$\Delta\kappa = k_p - k \left(\cos\theta + \sqrt{(k_i/k)^2 - \sin^2\theta} \right) \quad (12)$$

as well as equation (3), depends only on λ (using $\omega = 2\pi c/\lambda$) and θ , which are the natural dimensions of the detector.

In equation (9) we approximated the integral of \mathcal{N} over $d\lambda$ and $d\Omega = \sin\theta d\theta d\phi$ by just multiplying the integration intervals. This is of course valid if \mathcal{N} depends only weakly on both λ and θ over the range of interest.

In the experiment we place a pinhole in the far field of the spontaneous PDC light to filter a small range of angles. We show in the density plot of Supplementary Fig. 1 the product $\mathcal{D}(\lambda)\mathcal{N}$ as a function of θ and λ , and mark the size of our pinhole by a semi-transparent white strip. This numerical result is based on the Sellmeier equations of the three fields for BBO²³. We further assume that \mathcal{G} is constant in the wavelength range of interest, and we justify this assumption in the next section. We work close to collinear propagation, with $\theta \approx 0$, where the function $\mathcal{D}(\lambda)\mathcal{N}$ does not vary significantly across the pinhole area so that we can perform the integration by just multiplying by the solid angle. Similarly, the size of a pixel corresponds roughly to a bandwidth of 0.063 nm. On this scale, \mathcal{N} does not change significantly. Hence, our approximation in equation (9) is valid for our set-up.

Of course, one can also integrate over the solid angle covered by the pinhole to obtain a more accurate result, but at some point the contribution of other crystal properties, such as its length, as well as the dispersion relations of all the light fields will dominate. In the spirit of an easy-to-implement calibration technique,

we refrain from this more complex analysis but emphasize that it is possible. In a similar manner, one could include both the frequency as well as the angular profile of the pump in equation (3). However, on axis this treatment would not lead to a different result and our plane wave and monochromatic assumption is well-justified for our laser system.

Wavelength dependence of gain. In the main text, we assumed that the wavelength dependence of the gain function

$$\mathcal{G} = c^{-1} L \chi^{(2)} E_p / \sqrt{n n_i} \quad (13)$$

can be neglected. In this section, we investigate different effects that could contribute to the wavelength dependence in our experiment and demonstrate that they do not vary much across the spectral region of interest. In addition to the linear dispersion ($n(\lambda)$ and $n_i(\lambda)$) as well as the nonlinear dispersion $\chi^{(2)}(\omega_p, \omega, \omega_i)$, obvious from equation (13), other contributions arise from tilting the angle of the crystal to scan different phase-matching conditions. By tilting the crystal, the Fresnel coefficients vary (for the pump or for the down-converted light) and the effective length L of the nonlinear crystal (defined as the length of propagation of the pump inside the crystal) changes. The different Fresnel coefficients change the intensity of the pump inside the crystal, as well as how much of the down-converted light couples out of the crystal. Using the Sellmeier equations for BBO²³ and Miller's rule²⁴ (relating the first-order and second-order susceptibilities), we estimate the impact of those contributions, and show our results in Supplementary Fig. 2. The largest deviations are attributed to the dispersion in the nonlinear susceptibility $\chi^{(2)}$ and to the change in the effective length of the nonlinear crystal upon tilting it. However, over a spectral range of 300 nm around degeneracy, the gain function \mathcal{G} does not vary by more than 1%.

Experimental set-up. A detailed set-up is shown in Supplementary Fig. 3. The third harmonic (355 nm wavelength, 29 ps pulse duration, 50 Hz repetition rate, pump beam area $A_p = 2\pi\sigma^2 = (0.17 \pm 0.01) \text{ mm}^2$, with the standard deviation σ of the Gaussian profile, 100 μJ pulse energy in the spontaneous regime, up to 500 μJ in the high-gain regime) of a pulsed Nd:YAG laser (EKSPLA, PL2231) is prepared as the pump for PDC from a nonlinear crystal (β -BBO, 3 mm thickness, type-I phase-matching, uncoated, cut for degenerate PDC) whose phase-matching frequencies are tuned using a motorized rotation mount. We estimate the systematic error on the pulse duration to be ± 2 ps. The standard error on the pump beam area is obtained from repeated measurements of the attenuated pump on the Gentec Beamage-3.0 beam profiler. The wavelengths that satisfy the phase-matching condition are tuned by varying the angle between the optic axis of the crystal and the wavevector of the pump. We test the uniformity of the crystal by measuring the PDC spectra produced by pumping different portions of the crystal. A set of dichroic mirrors removes the pump after the crystal. The pump energy drift over time is monitored using a photodiode. A concave mirror of focal length 200 mm is used to bring the down-converted light to the far field, where a pinhole (0.5 mm diameter) selects a small solid angle. To ensure a fixed polarization, a broadband polarizing beam splitter is placed before the pinhole. A pair of lenses is used to image the pinhole onto the entrance slit (1 mm in width) of the spectrometer with a magnification of 4/3. The spectrometer is an imaging spectrograph (Acton SP-2558) with a charge-coupled device camera (PIXIS:100BR_eXcelon, pixels of size $20 \mu\text{m} \times 20 \mu\text{m}$). Transverse binning is enabled, so that the signal at a certain wavelength is the sum of the photoelectron counts over all the pixels that correspond to that wavelength. The integration time for each of the 411 spectra is 500 ms. Each spectrum spans the range from 450 nm to 900 nm. To cover this range, we need to repeat the acquisition for different angular positions of the grating (600 grooves per mm, 500 nm blaze). The experiment is automated: after each acquisition by the spectrometer, the motorized holder rotates the crystal through an angle of about 0.01° , up to a total change of approximately 8° . To reduce errors, we filter out the noise (rapidly fluctuating signal) in each spectrum with an algorithm based on the fast Fourier transform. For the nonlinear curve fitting of PDC in the high-gain regime, we used a weight function to reduce the influence of the data points associated with high residuals. The spectrometer is calibrated in wavelength using a neon–argon lamp along with a Princeton Instruments Intellistack system. The reference lamp (an LED-stack with a diffuser, Princeton Instruments) is introduced at the crystal plane. Its spectrum is acquired using the same experimental settings.

Details of the data analysis. Our calibration method relies on the comparison of the measured phase-matched number of counts $M(\lambda_{pm})$ to the expected phase-matched number of photons $N(\lambda_{pm})$. We therefore acquire a large number of spectra M_i corresponding to different phase-matching conditions over a broad spectral range. However, the peak number of counts in a measured spectrum does not correspond, in general, to $M(\lambda_{pm})$. Instead, we can extract the response function from the properties of \mathcal{N} . From the main text, we know that

$$\mathcal{N} \propto \omega(\omega_p - \omega) \text{sinc}^2(\Delta\kappa L / 2) \leq \omega(\omega_p - \omega) \quad (14)$$

where the inequality becomes an equality only for phase matching $\Delta\kappa=0$. We denote the wavelength of phase matching with λ_{PM} . With equation (5) we find the inequality

$$R(\lambda) \geq R(\lambda) \text{sinc}^2 \frac{\Delta\kappa L}{2} \propto \frac{M_j(\lambda)}{\mathcal{D}(\lambda)\omega(\omega_p - \omega)} \quad (15)$$

with an equality sign for $\lambda = \lambda_{\text{PM}}$. If we approximate the phase matching function by a Gaussian, that is,

$$\text{sinc}^2(\Delta\kappa L / 2) \propto \exp[-(\lambda - \lambda_{\text{PM}})^2 / (2\sigma_\lambda^2)] \quad (16)$$

it is easy to show that the peak of the product $R(\lambda)\text{sinc}^2(\Delta\kappa L/2)$ shifts to the wavelength

$$\tilde{\lambda} = \lambda_{\text{PM}} + \frac{1}{R} \frac{dR}{d\lambda} \bigg|_{\tilde{\lambda}} \sigma_\lambda^2 \quad (17)$$

Hence, the steeper the slope of the response function, the greater the shift between the phase-matched wavelength and the peak. We show this effect in the inset of Fig. 2. Since the response function is not known but is the result of the calibration procedure, equation (17) cannot be used to determine the phase-matching wavelength. However, equation (15) directly gives a method to determine the response function despite the shift: when we acquire a large number of spectra M_j , each with a slightly varying λ_{PM} , the amplitude of $M_j / [\mathcal{D}\omega(\omega_p - \omega)]$ at one particular wavelength is the largest if the wavelength corresponds to λ_{PM} . Hence, we obtain the response function from

$$R(\lambda) = \max_j \left[\frac{M_j(\lambda)}{\mathcal{D}(\lambda)\omega(\omega_p - \omega)} \right] / \max_j \left[\frac{4M_j(2\lambda_p)}{\mathcal{D}(2\lambda_p)\omega_p^2} \right] \quad (18)$$

where we normalize the response function to unity at the degenerate wavelength $\lambda = 2\lambda_p$. To reduce errors in the analysis according to equation (18), we suppress for each spectrum $M_j(\lambda)$ the high-frequency content, filtered out via a fast Fourier transform procedure.

A similar idea can be used for absolute calibration. For an arbitrary \mathcal{G} , the photon distribution per plane-wave mode assuming a monochromatic plane wave pump can be written as⁷

$$\mathcal{N}^{(\text{HG})} = \frac{\mathcal{G}^2 \mathcal{Q}^2}{\mathcal{G}^2 \mathcal{Q}^2 - (\Delta\kappa L / 2)^2} \sinh^2 \sqrt{\mathcal{G}^2 \mathcal{Q}^2 - (\Delta\kappa L / 2)^2} \quad (19)$$

where $\mathcal{Q}^2 \equiv \omega(\omega_p - \omega)$ and the superscript (HG) highlights that we are using this equation to describe the high-gain regime of PDC. Since the maximum of this function occurs for phase matching ($\Delta\kappa=0$), we find

$$\mathcal{N}^{(\text{HG})} \leq \sinh^2(\mathcal{G}\mathcal{Q}) \equiv \mathcal{N}_{\text{PM}}^{(\text{HG})} \quad (20)$$

where we defined the phase-matched photon distribution $\mathcal{N}_{\text{PM}}^{(\text{HG})}$, which has the well-known hyperbolic form of parametric amplification and is used in the main body of our article. Note further that for $\mathcal{G}\mathcal{Q} \ll 1$ we recover the low-gain result.

The quantum efficiency at the degenerate wavelength $\alpha = \eta(2\lambda_p)$ is

$$\alpha = M_j(\lambda) / [R(\lambda)N(\lambda)] \quad (21)$$

with the definitions from the main text. With that, we find from equation (20) and with the help of equation (10) the inequality

$$\alpha \sinh^2 \mathcal{G}\mathcal{Q} \geq M_j(\lambda) / [R(\lambda)\mathcal{D}(\lambda)\Delta\Omega\Delta\lambda_s c\tau_s] \quad (22)$$

where again the equal sign is valid for $\lambda = \lambda_{\text{PM}}$. Hence, we find, similarly to the low-gain method

$$\alpha \sinh^2 \mathcal{G}\mathcal{Q} = \max_j \left[\frac{M_j(\lambda)}{R(\lambda)\mathcal{D}(\lambda)\Delta\Omega\Delta\lambda_s c\tau_s} \right] \quad (23)$$

as an exact equality if the spectra are sufficiently dense. Taking the maximum of all recorded spectra, each one of them divided by $R(\lambda)\mathcal{D}(\lambda)$ and a numerical factor that depends on laboratory parameters (spatial dimensions and bandwidths), we can fit the data to the function $\alpha \sinh^2 \mathcal{G}\mathcal{Q}$ with two fitting parameters α and \mathcal{G} . Note that we do not need to measure the exponential increase of the number of generated photons with increasing pump intensity, but determine both parameters from the distortion of the spectral shape of the maximum of all spectra. With this fitting procedure, one can determine not only the quantum efficiency $\eta(\lambda) = \alpha R(\lambda)$, but also the gain \mathcal{G} .

Even though we do not use the exponential increase with the pump power for our calibration method, we still record the intensity while scanning different phase matching functions. We do this to correct for drifts and fluctuations during the course of one measurement. We are then able to perform the fitting procedure using \mathcal{G} / E_p , where E_p is the pump field amplitude during measurement corresponding to the j th phase-matching condition.

The α obtained using our method for absolute calibration is compared to an estimated quantum efficiency based on the properties of each optical component in the experimental set-up, listed in Supplementary Table 1. The losses of uncoated components are estimated from the Fresnel coefficients, whereas the losses of coated components are taken from the manufacturers.

Spontaneous regime of PDC. As shown in equation (19), the photon-number distribution grows exponentially with the intensity of the pump. In the low-gain regime, where the photon pairs are generated spontaneously, the number of photons grows linearly with the intensity, which can be seen from the expansion

$$\mathcal{N}_{\text{PM}}^{(\text{HG})} = \sinh^2 \mathcal{G}\mathcal{Q} \cong \mathcal{G}^2 \mathcal{Q}^2 = \mathcal{G}^2 \omega(\omega_p - \omega) = \mathcal{N}_{\text{PM}} \quad (24)$$

where \mathcal{N}_{PM} is the low-gain photon distribution for phase matching. To obtain the response function $R(\lambda)$, we do not need to know the exact value of \mathcal{G} , but rely on the fact that the first-order expansion above is valid. Note that \mathcal{G}^2 is proportional to the intensity of the pump⁷. To verify that we work in the spontaneous regime of PDC, we measure the number of counts for a single wavelength and increase the pump intensity. The results, given in Supplementary Fig. 4, show that we are well within the linear regime up to roughly 150 μJ pump energy. We performed the relative calibration experiment at a pump intensity of 100 μJ , whereas the high-gain part of the experiment used a more intense pump, around 200 μJ and higher.

Data availability

The data that support the plots within this paper and other findings of this study are available from the corresponding author on reasonable request.

References

22. Datla, R. U. & Parr, A. C. in *Optical Radiometry: Volume 41 (Experimental Methods in the Physical Sciences)* (eds Parr, A. C. et al.) Ch. 1 (Elsevier, Amsterdam, 2005).
23. Eimerl, D., Davis, L., Velsko, S., Graham, E. K. & Zalkin, A. Optical, mechanical, and thermal properties of barium borate. *J. Appl. Phys.* **62**, 1968–1983 (1987).
24. Boyd, R. W. *Nonlinear Optics* (Academic, Burlington, 2003).

In the format provided by the authors and unedited.

A primary radiation standard based on quantum nonlinear optics

Samuel Lemieux ^{1*}, Enno Giese ^{1,6}, Robert Fickler^{1,7}, Maria V. Chekhova^{2,3,4} and Robert W. Boyd^{1,5}

¹Department of Physics, University of Ottawa, Ottawa, Ontario, Canada. ²Max Planck Institute for the Science of Light, Erlangen, Germany.

³Physics Department, Lomonosov Moscow State University, Moscow, Russia. ⁴University of Erlangen-Nuremberg, Erlangen, Germany.

⁵Institute of Optics, University of Rochester, Rochester, NY, USA. ⁶Present address: Institut für Quantenphysik and Center for Integrated Quantum Science and Technology, Universität Ulm, Ulm, Germany. ⁷Present address: Photonics Laboratory, Physics Unit, Tampere University, Tampere, Finland.

*e-mail: 

Supplementary Material : A Primary Radiation Standard Based on Quantum Nonlinear Optics

Samuel Lemieux,^{1,*} Enno Giese,^{1,2} Robert Fickler,^{1,3}

Maria V. Chekhova,^{4,5,6} and Robert W. Boyd^{1,7}

¹*Department of Physics and Max Planck Centre for Extreme and Quantum Photonics,
University of Ottawa, 25 Templeton Street, Ottawa, Ontario K1N 6N5, Canada*

²*Current address: Institut für Quantenphysik and Center
for Integrated Quantum Science and Technology (IQST),*

Universität Ulm, Albert-Einstein-Allee 11, D-89069 Ulm, Germany

³*Current address: Institute for Quantum Optics and Quantum Information (IQOQI),
Austrian Academy of Sciences, Boltzmanngasse 3, 1090 Vienna, Austria*

⁴*Max Planck Institute for the Science of Light,*

G.-Scharowsky Str.1/Bau 24, 91058 Erlangen, Germany

⁵*Physics Department, Lomonosov Moscow State University, Moscow 119991, Russia*

⁶*University of Erlangen-Nuremberg, Staudtstrasse 7/B2, 91058 Erlangen, Germany*

⁷*Institute of Optics, University of Rochester, Rochester, New York 14627, USA*

TABLE S1. Contribution of each optical component to the total quantum efficiency of the experimental setup. The parentheses denote the number of components. The total efficiency is obtained by multiplying all the contributions and propagating the uncertainties accordingly.

Optical component	Efficiency
Crystal output facet (1)	0.94 ± 0.01
Dichroic mirror (2)	0.95 ± 0.01
Dielectric mirrors (6)	0.99 ± 0.01
Polarizing beam splitter (1)	0.98 ± 0.01
Uncoated lens (2)	0.92 ± 0.01
Diffraction grating (1)	0.60 ± 0.02
Spectrometer camera (1)	0.95 ± 0.02
Total	0.38 ± 0.07

* XXXXXXXXXX

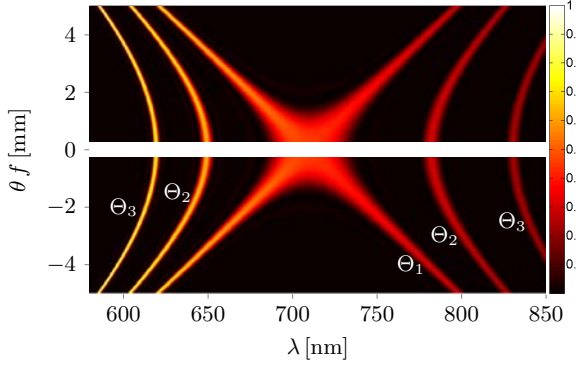


FIG. S1. Numerically generated spectrum of spontaneous PDC, plotting $\mathcal{D}(\lambda)\mathcal{N}$, for three different crystal tilt angles Θ , with Θ_1 corresponding to degenerate phase-matching in the emission angle $\theta = 0$. While \mathcal{N} is the spectral density in the k -space, $\mathcal{D}(\lambda)\mathcal{N}$ corresponds to the spectral density in the angular-wavelength representation, which is the measurement basis of our spectrometer. The vertical axis is represented in terms of the position in the far-field, using a concave mirror of focal length $f = 200$ mm. The semi-transparent white strip is the angular filtering of a pinhole of size 0.5 mm positioned around $\theta = 0$.

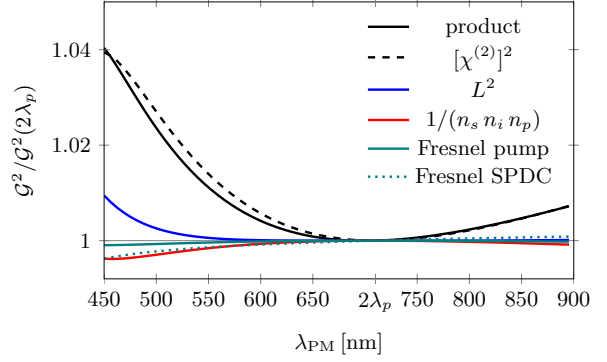


FIG. S2. Wavelength dependence of \mathcal{G}^2 , normalized to its value at the degenerate frequency. Each phase-matched wavelength λ_{PM} corresponds to a set of refractive indices n_s , n_i and n_p (subscripts s , i and p denote the signal, idler and pump fields) that satisfy the phase-matching condition, occurring at a certain tilt of the nonlinear crystal. The refractive indices also influence the nonlinearity $\chi^{(2)}$, appearing as well in equation (14) of the main text, through Miller's rule. At a given energy per pulse, the electric field amplitude of the pump scales with n_p^{-1} . We combined this contribution with $1/(n_s n_i)$, which is explicit in the expression for \mathcal{G}^2 . The varying angle between the pump propagation direction and the crystal leads to a different effective length L of the crystal. The Fresnel coefficients depend on the incidence angle and on the refractive indices: at the entrance facet the coefficients change how much of the pump E_p is transmitted into the nonlinear medium; the exit facet changes the amount down-converted light that couples out. The solid black line is the product all these effects.

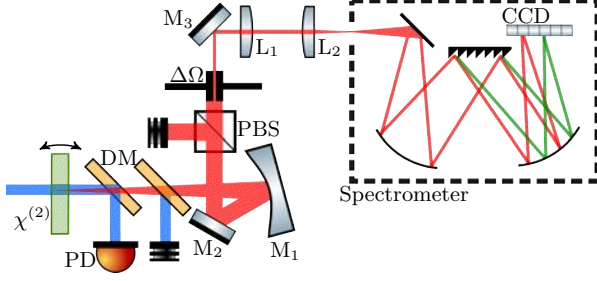


FIG. S3. Experimental setup. The pulsed pump laser (blue) is filtered before entering the setup by dispersive prisms. A half-wave plate and α -BBO Glan-Laser polarizer set the polarization, a pair of lenses bring the diameter of the laser beam down to approximately 0.6 mm, a pinhole of size 100 μm is introduced between the lenses at the beam focus to spatially filter the beam, and another α -BBO Glan-Laser polarizer confirms the polarization of the beam. Two dichroic mirrors (DM) suppress the pump after the $\chi^{(2)}$ crystal and reflect the pump light onto a photodiode (PD) to monitor its intensity. A concave mirror (M_1) of focal length 200 mm is used to bring the down-converted light to the far field reflecting off a planar mirror (M_2), where a pinhole $\Delta\Omega$ (0.5 mm diameter) selects a small solid angle. A broadband polarizing beam splitter (PBS) placed before the iris is set to transmit the polarization of the down-converted light. A pair of lenses of (L_1 and L_2) are used to image the iris onto the entrance slit of the spectrometer (Acton SP-2558) with a magnification of 4/3, which brings the grating-diffracted light onto the CCD camera (PIXIS:100BR_eXcelon).

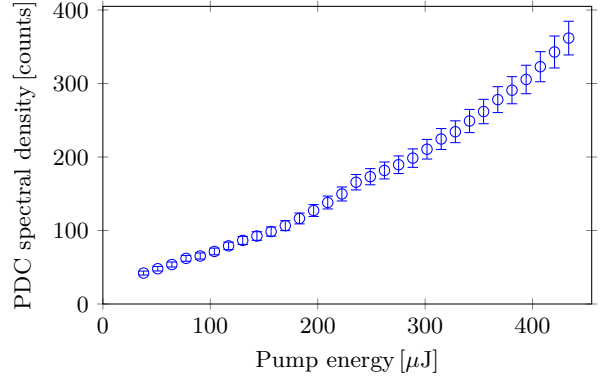


FIG. S4. PDC spectral density as a function of the pump energy per pulse. The number of counts was extracted at the phase-matched wavelength $\lambda = 690\text{ nm}$. The error bars are obtained from the amplitude of the noise in the spectrum. The acquisition time is 5 seconds, for a total of 250 pulses. Uncertainties for the pump energy include the standard error to the mean, as well as the longer-term fluctuations of the laser, which could lead to a systematic error of up to 5%.

Chapter 7

Conclusion

The goal of this thesis has been to investigate, both conceptually and experimentally, how our understanding of PDC needs to be expanded upon or more rigourously described when transitioning from the spontaneous to the high-gain regime. This included an experimental technique to reduce squeezed light to a single frequency mode for improved efficiency, theoretical and experimental insights into the evolving structure of PDC in the high-gain regime, a proposal for mitigating the effect of losses in $SU(1,1)$ interferometers and an experimental demonstration that high-gain PDC can serve as a primary standard for radiometry.

I utilize the various properties of high-gain PDC in order to devise or facilitate the usage of new tools in optical metrology. All applications presented in this thesis rely on key properties of high-gain PDC: quantum correlations between the signal and the idler, and the exponential increase in the number of photons with the parametric gain. Those properties are different sides of the same coin, stemming from the same theoretical framework of quantum and nonlinear optics. I separate these applications in three main branches: modes of bright squeezed vacuum, nonlinear interferometry and radiometry.

Bright squeezed vacuum generated via high-gain PDC in free space is naturally multimode. PDC radiation can be decomposed into modes that are squeezed pairwise, corresponding to an array of two-mode squeezed vacua. According to our theoretical model, the mode structure depends on the spectrum of the pump, the properties of nonlinear medium and on the parametric gain driving the OPA. In addition, we demonstrated that the field amplitude of the angular Schmidt modes can be retrieved from a measurement

of the covariance intensity. Those modes cannot be straightforwardly split or filtered. We experimentally showed that the number of frequency modes is greatly reduced in a two-crystal configuration, by amplifying in the second crystal a narrow frequency band of the PDC from the first crystal. Those developments, both experimental and theoretical, constitute important steps towards bright squeezed vacuum applied in quantum imaging and interferometry.

The study of the effect of internal loss in $SU(1,1)$ interferometers, which breaks the symmetry between the crystals, led us to a few interesting observations. Increasing the gain of the source crystal leads to a partial recovery of the phase sensitivity, despite internal loss. In the absence of internal loss, the phase sensitivity is limited by the crystal with the lower gain. This brings about a crucial discussion about the meaning of n , the number of photons, in the definition of the scaling of the phase sensitivity. Customarily, n is defined as the number of photons inside the interferometer. However, we concluded that it is not the number of photons produced by the source crystal that matters, but rather the number of photons associated with the smaller gains between the source and the analyzer.

The frequency spectrum of high-gain PDC is tied to the properties of vacuum fluctuations, allowing to predict the number of photons from first principles. This makes high-gain PDC a source-based primary standard for radiometry, akin to blackbody radiation. In this work, I successfully retrieve the spectral quantum efficiency of a spectroradiometer, without the need of a calibrated reference. This adds another tool for the field of primary standard metrology, for which validation depends on the comparative study of other standards. The results I present in this thesis are a proof of principle. I therefore identify the main sources of error to be addressed in order to bring the error margin down and potentially make high-gain PDC a usable standard in metrology laboratories.

We can consider bright squeezed light to be classical-scale optical fields that exhibit clear, quantum-like properties and statistics. This behaviour invites conceptualization of a multitude of practical applications where classical limits on metrology or even whole new standards for radiometry become available. Provided we have sufficient, careful understanding into the quantum nature of how squeezed light is generated and the resulting consequences, we will be able to shine this bright light into otherwise dark corners of yet unknown physics.

References

- [1] R. W. Boyd, *Nonlinear optics*. Academic press, 2020.
- [2] M. O. Scully and M. S. Zubairy, *Quantum optics*. American Association of Physics Teachers, 1999.
- [3] A. Aspect, J. Dalibard, and G. Roger, “Experimental test of bell’s inequalities using time-varying analyzers,” *Physical Review Letters*, vol. 49, no. 25, p. 1804, 1982.
- [4] A. Furusawa, J. L. Sørensen, S. L. Braunstein, C. A. Fuchs, H. J. Kimble, and E. S. Polzik, “Unconditional quantum teleportation,” *Science*, vol. 282, no. 5389, pp. 706–709, 1998.
- [5] C.-K. Hong, Z.-Y. Ou, and L. Mandel, “Measurement of subpicosecond time intervals between two photons by interference,” *Physical review letters*, vol. 59, no. 18, p. 2044, 1987.
- [6] A. Heidmann, R. Horowicz, S. Reynaud, E. Giacobino, C. Fabre, and G. Camy, “Observation of quantum noise reduction on twin laser beams,” *Physical Review letters*, vol. 59, no. 22, p. 2555, 1987.
- [7] T. Sh. Iskhakov, I. N. Agafonov, M. V. Chekhova, and G. Leuchs, “Polarization-entangled light pulses of 10^5 photons,” *Physical Review Letters*, vol. 109, no. 15, p. 150502, 2012.
- [8] R. Slusher, L. Hollberg, B. Yurke, J. Mertz, and J. Valley, “Observation of squeezed states generated by four-wave mixing in an optical cavity,” *Physical Review Letters*, vol. 55, no. 22, p. 2409, 1985.
- [9] L.-A. Wu, H. Kimble, J. Hall, and H. Wu, “Generation of squeezed states by parametric down conversion,” *Physical Review Letters*, vol. 57, no. 20, p. 2520, 1986.

- [10] A. I. Lvovsky, “Squeezed light,” *Photonics: Scientific Foundations, Technology and Applications*, vol. 1, pp. 121–163, 2015.
- [11] M. e. Tse, H. Yu, N. Kijbunchoo, A. Fernandez-Galiana, P. Dupej, L. Barsotti, C. Blair, D. Brown, S. Dwyer, A. Effler, *et al.*, “Quantum-enhanced advanced ligo detectors in the era of gravitational-wave astronomy,” *Physical Review Letters*, vol. 123, no. 23, p. 231107, 2019.
- [12] D. N. Klyshko, *Photons and nonlinear optics*. Routledge, 1988.
- [13] B. Yurke, S. L. McCall, and J. R. Klauder, “SU(2) and SU(1,1) interferometers,” *Physical Review A*, vol. 33, no. 6, p. 4033, 1986.
- [14] M. Chekhova and Z. Ou, “Nonlinear interferometers in quantum optics,” *Advances in Optics and Photonics*, vol. 8, no. 1, pp. 104–155, 2016.
- [15] D. Klyshko, “Use of two-photon light for absolute calibration of photoelectric detectors,” *Soviet Journal of Quantum Electronics*, vol. 10, no. 9, p. 1112, 1980.
- [16] A. Malygin, A. Penin, and A. Sergienko, “Absolute calibration of the sensitivity of photodetectors using a biphotonic field,” *JETP Lett*, vol. 33, no. 10, 1981.
- [17] S. V. Polyakov and A. L. Migdall, “High accuracy verification of a correlated-photon-based method for determining photon-counting detection efficiency,” *Optics Express*, vol. 15, no. 4, pp. 1390–1407, 2007.
- [18] I. D. Leroux, M. H. Schleier-Smith, and V. Vuletić, “Orientation-dependent entanglement lifetime in a squeezed atomic clock,” *Physical Review Letters*, vol. 104, no. 25, p. 250801, 2010.
- [19] M. Kitagawa and M. Ueda, “Squeezed spin states,” *Physical Review A*, vol. 47, no. 6, p. 5138, 1993.
- [20] R. Loudon, *The quantum theory of light*. OUP Oxford, 2000.
- [21] B. Stiller, U. Seyfarth, G. Leuchs, C. Fabre, V. Sandoghdar, N. Treps, and L. Cugliandolo, *Temporal and spectral properties of quantum light*. 2014.
- [22] A. Einstein, B. Podolsky, and N. Rosen, “Can quantum-mechanical description of physical reality be considered complete?,” *Phys. Rev.*, vol. 47, pp. 777–780, May 1935.

- [23] R. J. Glauber, “The quantum theory of optical coherence,” *Physical Review*, vol. 130, no. 6, p. 2529, 1963.
- [24] L. Mandel and E. Wolf, *Optical coherence and quantum optics*. Cambridge university press, 1995.
- [25] R. Brown and R. Q. Twiss, “Correlation between photons in two coherent beams of light,” *Nature*, vol. 177, no. 4497, pp. 27–29, 1956.
- [26] M. Reid and D. Walls, “Violations of classical inequalities in quantum optics,” *Physical Review A*, vol. 34, no. 2, p. 1260, 1986.
- [27] C. Gerry, P. Knight, and P. L. Knight, *Introductory quantum optics*. Cambridge university press, 2005.
- [28] T. Pittman, D. Strekalov, D. Klyshko, M. Rubin, A. Sergienko, and Y. Shih, “Two-photon geometric optics,” *Physical Review A*, vol. 53, no. 4, p. 2804, 1996.
- [29] M. I. Kolobov and P. Kumar, “Sub-shot-noise microscopy: imaging of faint phase objects with squeezed light,” *Optics Letters*, vol. 18, no. 11, pp. 849–851, 1993.
- [30] G. Brida, M. Genovese, and I. Ruo Berchera, “Experimental realization of sub-shot-noise quantum imaging,” *Nature Photonics*, vol. 4, no. 4, pp. 227–230, 2010.
- [31] S. Lemieux, J. Rioux, B. Braverman, and R. W. Boyd, “Spatial correlation functions for arbitrary pump profiles in bright twin beams,” in *Conference on Coherence and Quantum Optics*, pp. W6A–26, Optical Society of America, 2019.
- [32] W. Wasilewski, A. I. Lvovsky, K. Banaszek, and C. Radzewicz, “Pulsed squeezed light: Simultaneous squeezing of multiple modes,” *Physical Review A*, vol. 73, no. 6, p. 063819, 2006.
- [33] M. A. Finger, T. S. Iskhakov, N. Y. Joly, M. V. Chekhova, and P. S. J. Russell, “Raman-free, noble-gas-filled photonic-crystal fiber source for ultrafast, very bright twin-beam squeezed vacuum,” *Physical Review Letters*, vol. 115, no. 14, p. 143602, 2015.
- [34] A. Christ, B. Brecht, W. Mauerer, and C. Silberhorn, “Theory of quantum frequency conversion and type-ii parametric down-conversion in the high-gain regime,” *New Journal of Physics*, vol. 15, no. 5, p. 053038, 2013.

- [35] E. Schmidt, “Zur theorie der linearen und nichtlinearen integralgleichungen,” in *Integralgleichungen und Gleichungen mit unendlich vielen Unbekannten*, pp. 190–233, Springer, 1989.
- [36] D. Horoshko, L. La Volpe, F. Arzani, N. Treps, C. Fabre, and M. Kolobov, “Bloch-messiah reduction for twin beams of light,” *Physical Review A*, vol. 100, no. 1, p. 013837, 2019.
- [37] M. Fedorov and N. Miklin, “Schmidt modes and entanglement,” *Contemporary Physics*, vol. 55, no. 2, pp. 94–109, 2014.
- [38] A. Pérez, T. S. Iskhakov, P. Sharapova, S. Lemieux, O. Tikhonova, M. Chekhova, and G. Leuchs, “Bright squeezed-vacuum source with 1.1 spatial mode,” *Optics Letters*, vol. 39, no. 8, pp. 2403–2406, 2014.
- [39] Z. Ou and X. Li, “Quantum SU(1,1) interferometers: Basic principles and applications,” *APL Photonics*, vol. 5, no. 8, p. 080902, 2020.
- [40] E. Polino, M. Valeri, N. Spagnolo, and F. Sciarrino, “Photonic quantum metrology,” *AVS Quantum Science*, vol. 2, no. 2, p. 024703, 2020.
- [41] S. L. Braunstein and C. M. Caves, “Statistical distance and the geometry of quantum states,” *Physical Review Letters*, vol. 72, no. 22, p. 3439, 1994.
- [42] J. P. Dowling, “Quantum optical metrology—the lowdown on high-n00n states,” *Contemporary physics*, vol. 49, no. 2, pp. 125–143, 2008.
- [43] B. Dayan, “Theory of two-photon interactions with broadband down-converted light and entangled photons,” *Physical Review A*, vol. 76, no. 4, p. 043813, 2007.
- [44] L. Landau, “Electrodynamics of continuous media, landau and lifshitz course of theoretical physics, vol. 8,” 1984.
- [45] T. Sh. Iskhakov, S. Lemieux, A. Pérez, R. Boyd, G. Leuchs, and M. Chekhova, “Non-linear interferometer for tailoring the frequency spectrum of bright squeezed vacuum,” *Journal of Modern Optics*, vol. 63, no. 1, pp. 64–70, 2016.
- [46] N. Quesada and J. Sipe, “Effects of time ordering in quantum nonlinear optics,” *Physical Review A*, vol. 90, no. 6, p. 063840, 2014.

- [47] M. Manceau, F. Khalili, and M. Chekhova, “Improving the phase super-sensitivity of squeezing-assisted interferometers by squeeze factor unbalancing,” *New Journal of Physics*, vol. 19, no. 1, p. 013014, 2017.
- [48] S. Lemieux, M. Manceau, P. R. Sharapova, O. V. Tikhonova, R. W. Boyd, G. Leuchs, and M. V. Chekhova, “Engineering the frequency spectrum of bright squeezed vacuum via group velocity dispersion in an SU(1,1) interferometer,” *Physical Review Letters*, vol. 117, no. 18, p. 183601, 2016.
- [49] S. Lemieux, M. Manceau, R. Boyd, G. Leuchs, and M. V. Chekhova, “Apparatus and method for calibrating measuring instruments,” Patent CA 3039461, 2017.